University of Alberta

Glancing Angle Deposition

by

Kevin Robbie

A thesis submitted to the Faculty of Graduate Studies and Research in partial fulfillment of the requirements for the degree of Doctor of Philosophy

Department of Electrical and Computer Engineering

Edmonton, Alberta, Canada

Fall 1998

National Library of Canada
Acquisitions and Bibliographic Services
395 Wellington Street
Ottawa ON K1A 0N4
Canada

Bibliothèque nationale du Canada
Acquisitions et services bibliographiques
395, rue Wellington
Ottawa ON K1A 0N4
Canada

Your file Votre référence

Our file Notre référence

The author has granted a non-exclusive licence allowing the National Library of Canada to reproduce, loan, distribute or sell copies of this thesis in microform, paper or electronic formats.

L'auteur a accordé une licence non exclusive permettant à la Bibliothèque nationale du Canada de reproduire, prêter, distribuer ou vendre des copies de cette thèse sous la forme de microfiche/film, de reproduction sur papier ou sur format électronique.

The author retains ownership of the copyright in this thesis. Neither the thesis nor substantial extracts from it may be printed or otherwise reproduced without the author's permission.

L'auteur conserve la propriété du droit d'auteur qui protège cette thèse. Ni la thèse ni des extraits substantiels de celle-ci ne doivent être imprimés ou autrement reproduits sans son autorisation.

0-612-39771-8

Canada

University of Alberta

Library Release Form

Name of Author: Kevin Robbie

Title of Thesis: Glancing Angle Deposition

Degree: Doctor of Philosophy

Year this Degree Granted: 1998

Permission is hereby granted to the University of Alberta Library to reproduce single copies of this thesis and to lend or sell such copies for private, scholarly, or scientific research purposes only.

The author reserves all other publication and other rights in association with the copyright in the thesis, and except as hereinbefore provided, neither the thesis nor any substantial portion thereof may be printed or otherwise reproduced in any material form whatever without the author's prior written permission.

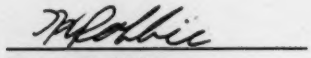

Kevin Robbie
264 Westridge Drive
Williams Lake
British Columbia
V2G 4R9
Canada

August 20, 1998

University of Alberta

Faculty of Graduate Studies and Research

The undersigned certify that they have read, and recommend to the Faculty of Graduate Studies and Research for acceptance, a thesis entitled 'Glancing Angle Deposition' submitted by Kevin Robbie in partial fulfillment of the requirements for the degree of Doctor of Philosophy.

Dr. M. J. Brett

Dr. R. P. W. Lawson

Dr. J. N. McMullin

Dr. M. R. Freeman

Dr. T. Hrudey

Dr. A. Elezzabi

Dr. L. Whitehead

To my wife, Chelsea, my parents, Joanne and Byron,
and my sister and brother, Gillian and Adam

Abstract

Glancing angle deposition (GLAD) is a new technique for fabricating semi-porous, structurally controlled materials. The technique combines obliquely-incident physical vapour deposition with computer-controlled substrate motion to produce thin films with engineered, nanometre-scale, columnar microstructure. A shadowing mechanism, which occurs at the atomic scale, is exploited to obtain structural control on a scale of tens of nanometres. Thin films with microstructures consisting of complex three-dimensional shapes have been created with this technique from a variety of materials, including metals, metal oxides and fluorides, and semiconductors. Examples of microstructure elements include helices, zigzags, staircases, and posts. Characterizations of a number of novel GLAD materials are presented. Helical, or chiral, films, of dielectric materials, with structure sizes matching visible light wavelengths, were investigated for polarization optical effects, and were found to behave similarly to chiral liquid crystals. Ellipsometry, polarimetry, and circular polarized spectroscopy analyses were used to characterize optical properties. Chiral films were also impregnated with fluids, including liquid crystals, and were found to enable control of the molecular orientation of the liquid crystal embedded in the voids of the porous film structure. Display and optical switching applications show particular promise for these GLAD materials. Another optical device, an optical interference filter, was fabricated by varying the density and hence the refractive index, of a film during deposition. An advanced GLAD technique was developed to circumvent the interdependence of film density and column growth angle. This technique increases the versatility of GLAD, and enables the fabrication of a wider range of structures. Numerous optical, chemical, biological, mechanical, magnetic, and electrical applications that might utilize GLAD are proposed.

Acknowledgement

I would like to thank the many people who helped me along the way: Chelsea Elliott, my wife, for unflagging love, support, and patience; George Braybrook for the many hours of electron microscope analysis in a darkened room, and the brief, but bright, moments of discovery; Herb, Herbert, and Bernie for the quality machining of the endless, odd, bits and pieces I dreamt up for them; Albert Huizinga for assistance with the design and construction of electrical equipment; Sandy Campbell for literature and patent searching guidance and assistance; Niall Tait, Glen Fitzpatrick, Graham McKinnon, Ken Westra, Doug Bowles, and all the Alberta Microelectronic Centre staff for technical guidance and words of advice; Mark Freeman for access to his laboratory, and for assistance with optical measurements; the Natural Sciences and Engineering Research Council of Canada and the Alberta Microelectronic Centre for financial support; and Michael Brett, my thesis supervisor, for teaching me what I needed to learn and letting me wander where I needed to wander, and for always having an open door. I would also like to thank my cat, Harley, for keeping me company while I wrote my thesis, and reminding me that you have to take time to sleep in the sun.

Table of Contents

Chapter 1 - Introduction ____ 1

1.1 Intention 2

1.2 Scope 3

Chapter 2 - Thin Film Structure and Oblique Deposition ____ 5

2.1 Physical Vapour Deposition 6

2.2 Thin Film Structure 8

a) nucleation 9
b) adatom diffusion and shadowing 11
c) columnar structure 14

2.3 Oblique Deposition 15

a) column inclination 16
b) density 19
c) structural anisotropy 19
d) extreme oblique deposition 20

2.4 Substrate Motion 21

Chapter 3 - Glancing Angle Deposition ____ 24

3.1 Growth Mechanics 25

a) stationary, zigzag, helical, post 25
b) variation of vapour incidence angle 27
c) variation of material 35
d) size scaling 38
e) adatom diffusion from heating 40
f) transmission electron microscopy 46

3.2 Equipment Development 49

a) fixed polar angle 50
b) variation of polar angle 51
c) techniques for stepper control 53
d) techniques for structure description 54

3.3 Capping 54

a) capping with GLAD 55
b) failure mechanisms 56
c) alternate techniques 58

Table of Contents (continued)

3.4 Applications 58

a) thermal barriers 58
b) dental adhesives 61
c) organic materials 61
d) chemical sensors 63
e) magnetic materials 64
f) biomaterials 64
g) chiral catalysis 65

Chapter 4 - Advanced Techniques for Structural Control ____ 67

4.1 Microstructure Restrictions 67

4.2 Substrate Motion Techniques 70

4.3 Advanced Structural Control Examples 73

Chapter 5 - Chiral Optics ____ 81

5.1 Chiral GLAD Films 82

a) chirality 83
b) optical activity 85
c) ellipsometry and effects of orientation 91
d) circular polarization effects 95

5.2 Liquid Crystals 101

a) chiral nematic liquid crystals 102
b) chiral optical devices 104
c) chiral GLAD/LC hybrid materials 106
d) chiral nematic impregnates 111

Chapter 6 - Interference Optics ____ 113

6.1 GLAD interference filters 113

6.2 Rugate Filters 116

Chapter 7 - Squeezing ____ 120

7.1 Springs 121

7.2 Interferometry 123

Table of Contents (continued)

Chapter 8 - Summary and Recommendations ____ **126**

8.1 Summary 126

8.2 Recommendations 127

Chapter 9 - References ____ **129**

List of Figures

Figure 1 : Thin film deposition by evaporation. 7
Figure 2 : Surface potential energy. 9
Figure 3 : Film nucleation and coalescence. 11
Figure 4 : Shadowing and adatom diffusion. 12
Figure 5 : Structure zone models. 13
Figure 6 : Columnar film microstructure. 15
Figure 7 : Column inclination schematic. 17
Figure 8 : Column inclination theory and experiment. 18
Figure 9 : Column spacing. 20
Figure 10 : Chevron film structure fabricated by Motohiro and Taga. 22
Figure 11 : Glancing Angle Deposition (GLAD) geometry. 23
Figure 12 : MgF_2 films demonstrating the GLAD technique. 26
Figure 13 : SiO films with varying vapour incidence angle. 29
Figure 14 : CaF_2 films with varying vapour incidence angle. 30
Figure 15 : Graph of theoretical and experimental film density. 31
Figure 16 : SiO film with sinusoidal variation of vapour incidence angle. 32
Figure 17 : SiO film with quasi-sinusoidal variation of vapour incidence. 33
Figure 18 : Cr film with porous 'post' structure atop a dense Cr layer. 34
Figure 19 : SiO with dense 'cap' atop a porous GLAD film. 35
Figure 20 : Structural variation with material. 36
Figure 21 : Cu films investigating rapid substrate rotation. 37
Figure 22 : MgF_2 size scaling in helical structures. 39
Figure 23 : SiO size scaling in helical structures to about 13 mm. 40
Figure 24 : GROFILMS investigation of film heating. 44
Figure 25 : Films investigating the effect of heating induced mobility. 45
Figure 26 : TEM image and electron diffraction pattern of a Si GLAD film. 47
Figure 27 : CaF_2 TEM images and electron diffraction patterns. 49
Figure 28 : Front panel of Labview control system for GLAD. 52

List of Figures (continued)

Figure 29 : MgF_2 capping with linear and exponential decrease in α. 56
Figure 30 : Failure mechanisms in capped GLAD films. 57
Figure 31 : Alternate techniques for capping GLAD films. 59
Figure 32 : Thermal barrier coating demonstration films. 60
Figure 33 : Organic dichroic dye deposited with GLAD. 61
Figure 34 : Cr film coated onto the cylindrical shaft of a dental implant. 62
Figure 35 : Porous GLAD platinum film. 63
Figure 36 : Co GLAD film investigating magnetic properties. 65
Figure 37 : Porous Ti demonstration for biomedical applications. 65
Figure 38 : Small scale structure at initial stages of film growth. 66
Figure 39 : Interdependence of column inclination and porosity. 68
Figure 40 : Cr films deposited obliquely onto stationary substrates. 69
Figure 41 : SiO films demonstrating advanced GLAD. 72
Figure 42 : SiO films deposited in 3 steps, varying the column angle. 75
Figure 43 : SiO films with dynamically varied column angle. 76
Figure 44 : Two helices with equal pitch but different column angles. 78
Figure 45 : Two helical SiO films with varied helical geometries. 79
Figure 46 : Chiral shapes which can be fabricated with GLAD. 83
Figure 47 : A right handed helix and its left handed mirror image. 84
Figure 48 : Chirality in medicine. 85
Figure 49 : Examples of handedness in organic chemistry. 86
Figure 50 : Optical activity in solutions of chiral molecules. 87
Figure 51 : Polarimetry technique used to measure optical rotation. 89
Figure 52 : Optical rotation of a MgF_2 helical (chiral) thin film. 90
Figure 53 : Optical rotation as a function of orientation of chiral film. 92
Figure 54 : Schematic of the Penn. State transmission ellipsometer. 94
Figure 55 : Transmission ellipsometry analysis of a MgF_2 helical film. 95
Figure 56 : Spectroscopic left and right circular polarized transmission. 97

List of Figures (continued)

Figure 57 : Difference spectra for film filled with index matching fluids. 99
Figure 58 : Graded pitch and right-left handed films. 100
Figure 59 : Rodlike and disklike molecules form liquid crystalline phases. 101
Figure 60 : Liquid crystalline phases in themotropic LCs. 102
Figure 61 : Chiral nematic or cholesteric LC phase. 103
Figure 62 : Difference spectra for a film impregnated with LCs. 109
Figure 63 : Transmission spectra for a film impregnated with E7 LC. 110
Figure 64 : Transmission spectra for a film impregnated with a chiral LC 111
Figure 65 : Reflection spectra of the first two GLAD interference filters. 114
Figure 66 : High quality GLAD interference (rugate) filter. 117
Figure 67 : One turn helical film for squeezing. 122
Figure 68 : Theoretical deflection of helical springs. 123
Figure 69 : GLAD film destroyed by electrical breakdown. 124
Figure 70 : Fibre interferometer with AC detection. 125

1. Introduction

Thin films are the workhorses of much of today's technology. Thin films are to modern industry what steel was to the industrial revolution. Entire technologies, from integrated circuits to spacecraft to candy wrappers are completely dependent on thin films. In many cases, a scientifically observed property of thin films led to the creation of an entirely new field of technology. In this century, thin films have been transformed from a laboratory curiosity to become a multi-billion dollar industry worldwide. Thin films are also a wonder of the purely scientific and artistic world. They can be beautiful, with iridescent colours and elegant patterns. When looking at a thin film with a scanning electron microscope (SEM), the top surface can look incredibly similar to a layer of clouds as viewed from an airplane (or the surface of a cauliflower). Because of similarities in growth processes, thin film growth resembles many physical phenomena, with fractal shapes and self-similarity over large size scales. While writing this thesis, I observed blowing snow deposited at an oblique angle onto a metal post, and many of the physical effects discussed in this thesis were observable.

The growth of thin films can be complex, making them difficult to study theoretically. For the most part they are not understood predictively to the degree necessary for technological use, making thin films very much an experimental study. Each new application of thin films requires extensive exploration before use. Advances in recent years, including thin film growth simulators, have helped to alleviate this lack of predictive theoretical understanding. The complexity of thin film growth can also be an advantage as it creates a large range of possible uses. Magnetic, optical, electrical, mechanical, and other properties can be controlled with the many techniques of thin film fabrication. Techniques are introduced every year to add a new tool to the thin film toolbox. This thesis describes one of those tools.

Glancing Angle Deposition (GLAD) is a technique for controlling the physical structure, or morphology, of thin films. Based on physical vapour deposition, it employs oblique angle deposition and controlled substrate motion to form a structure composed of nanometre scale columns of designed shape. Optical response of the engineered material can be designed, leading to a range of possibilities for scientific exploration and

technological application. GLAD is not limited to optics, however. As a fabrication technique it has great promise in fields including optical, chemical, electrical, biological, magnetic, and mechanical. Areas of possible study include sensors, filters (optical, chemical, biological etc.), barriers, catalysts, and many more.

1.1 Intention

The intention of this thesis is to give the reader a cohesive account of the technique called Glancing Angle Deposition (GLAD). By describing the GLAD process from the very basic to the most advanced, I hope to offer a manual of sorts for investigation of controlled materials with this fabrication technology. Discussions of methods and equipment should help to allow others to reproduce the work described here, and demonstrations of the relevant physical effects to the thin film growth process with GLAD will facilitate understanding. Analysis with techniques such as SEM, transmission electron microcopy (TEM), ellipsometry etc. serve to illustrate the physical effects and methods described and show the current state of the art. Suggestions of possible future avenues of exploration are discussed throughout the thesis.

While investigating and developing the GLAD technique, it was possible to take a number of approaches. For example, one could have chosen any of the possible application ideas and pursued it directly to attempt to produce a prototype device. This would have given a clear and direct demonstration of the power of GLAD, but would not have addressed much of the fundamental science. Alternatively, one could have investigated an important aspect of the deposition process, and set a firm framework for future researchers in the field. It was felt that the best approach, however, was to try to cover a number of avenues. Investigations of both basic science and potential applications were conducted and discussed in this thesis. This allowed many of the difficulties in various areas to be identified, while demonstrating the potential of GLAD in numerous fields in a short time. In-depth studies of important issues were performed along the way where warranted, including capping, and advanced control techniques. More direct, proof-of-principle prototype devices were constructed in a few instances, such as with interference filters. A variety of analysis techniques were used to assemble as much information as possible on

these new materials, and scanning electron microscopy (SEM), transmission electron microcopy (TEM), atomic force microscopy (AFM), electron and x-ray diffraction, ellipsometry, and interferometry were all used. Materials including low melting temperature metals (Cu), refractory metals (Pt, Cr), metal fluorides (MgF_2, CaF_2), semiconductors (Si), and organics were deposited with GLAD and analyzed with SEM. The intention of the research project described in this thesis was to produce a wide-ranging investigation of the GLAD process with concentrated effort in a few key areas.

1.2 Scope

The thesis begins with a chapter describing the background of thin film deposition leading to a discussion of deposition with oblique incidence and substrate motion. A detailed discussion of the prior art is given, with references to aid the reader. The GLAD technique is then described in a separate chapter, with discussions ranging from substrate heating effects to crystallinity. GLAD is described as a complete technique, with examples of possibilities, and with an emphasis on difficulties and failure mechanisms. In this chapter, the development of the GLAD deposition equipment is also given, as well as critiques of the various system configurations and approaches used for motion control. Finally, a number of broad application areas are presented with brief descriptions and, where possible, a proof-of-principle device fabricated with GLAD. An advanced GLAD technique is described in the next chapter, Chapter 4. The technique greatly expands the range of obtainable structures with GLAD and was the subject of a large amount of the work for this thesis. Using a duty-cycle approach to motion, growth of previously unobtainable structures is possible. Explanations of the technique, and demonstrations of realized structures, are given. Chapters 5 and 6 discuss optical properties of thin film materials fabricated with GLAD. First, the chiral optical properties of helical GLAD films are investigated experimentally, with comparison to the theory of the optically similar chiral nematic liquid crystals. Chiral hybrid materials are described, where the porous regions of the GLAD film are filled with various fluids, including liquid crystals. The structured GLAD material was found to control the molecular architecture of the liquid crystalline phase. Properties of this new hybrid material are discussed, as well as

possibilities for optical filtering and switching. In the second chapter discussing optical properties of GLAD films, interference filters are described, where refractive index variation is created by varying the porosity of the GLAD material. Filters with designed spectral response are demonstrated. Finally, an attempt at electrostatic actuation of the 'spring' structure of a helical columnar film is given. While no actuation was observed experimentally, the theory of springs is discussed. Also described is the development of a sensitive interferometer, capable of measuring deflections of tens of picometres. Finally, a short conclusion is given with recommendations for future investigations.

2. Thin Film Structure and Oblique Deposition

A thin film is a thin coating of one material which has been applied onto an object (or substrate) with a vacuum coating technique [75,90,121]. Typically, thin films have thicknesses of less than 1 micrometre (μm), although films of hundreds of micrometres in thickness are used in some applications, such as thermal barrier coatings. There are many non-vacuum thin film coating techniques, such as chemical plating and solution-gelation (sol-gel), but as they lack a fundamental mechanism of vacuum coating processes (shadowing), they are probably not compatible with the techniques described in this thesis. Generally, vacuum thin film deposition methods are divided into physical vapour deposition (PVD) techniques, where the film is produced by physical condensation of the film material from vapour phase onto the substrate, and chemical vapour deposition (CVD) techniques, where the film is produced as a result of a chemical reaction at the substrate from a set of chemical constituents transported to the substrate in vapour phase. The research described in this thesis is restricted to physical vapour deposition (PVD) techniques, specifically evaporation and sputtering. While glancing angle deposition (GLAD) techniques are not necessarily incompatible with all CVD processes, the differences between PVD and CVD suggest that the effects of GLAD would be significantly modified if not eliminated, with CVD (CVD can be used in film capping however - See "Capping" on page 54.). The gas phase transport and low sticking probability of most CVD processes largely eliminates the atomic shadowing effect that is a fundamental mechanism of GLAD.

Thin films deposited with PVD grow on the substrate through a condensation process with mechanics that have a significant effect on the structure and properties of the resulting film material [75,90,121]. Because of the condensation process, physical properties of thin films can be significantly different from the properties of a bulk quantity of the film material. Crystal structure (texture), packing density, electrical, magnetic, optical, and most other measurable properties can be different from what is observed for the bulk material, and can vary strongly with deposition process conditions such as vapour energy and arrival distributions, substrate temperature, background gas composition and pressure, substrate material, and surface state.

In this chapter I give a general overview of the thin film growth process from PVD, and relate relevant physical effects to GLAD. The GLAD process employs extremely oblique deposition angles and substrate motion which each have significant effects on film structure. I describe the literature involving oblique deposition and substrate motion and present a background for understanding the discussions of GLAD presented in subsequent chapters.

2.1 Physical Vapour Deposition

In physical vapour deposition (PVD) of thin films, a solid quantity of the desired film material (small pieces or a powder usually) is placed within a vacuum environment and vapourized [75]. The vapour travels atomistically through the vacuum (or molecularly for compounds such as magnesium fluoride - MgF_2), with little or no interaction in the vapour phase with other vapour or with the background gas (gas pressures are typically below 10^{-6} Torr (10^{-4} Pa or 10^{-9} atmosphere)), and condenses into a solid on the substrate and vacuum chamber walls. The simplest technique for forming the vapour, and the one used exclusively in this thesis, is evaporation. In evaporation deposition, the solid source material is simply heated until vapour is liberated (Figure 1). For many materials, the source material becomes a liquid before liberating significant vapour, while other materials sublimate, and liberate vapour directly from the solid phase. To obtain reasonable growth rates at the substrate (~1 nm/s), the material must be heated until its vapour pressure exceeds approximately 10^{-3} torr (10^{-1} Pa). The two most common heating techniques for evaporation deposition, both of which were used in the research in this thesis, are resistive heating and electron beam heating. With resistive heating, the source material is placed within a pocket in a refractory metal foil (typically W, Ta, or Mo, and called an evaporation boat), and a large current (hundreds of amperes) is passed through the foil. Resistive heating of the evaporation boat heats the boat and source material until the source material evaporates. Care must be taken to choose a source/boat material combination which will prevent the boat from melting, or from reacting (alloying etc.) with the source material. Resistively heated evaporation was used for the majority of thin film depositions described in this thesis, and is the technique shown schematically in Figure 1. In electron beam

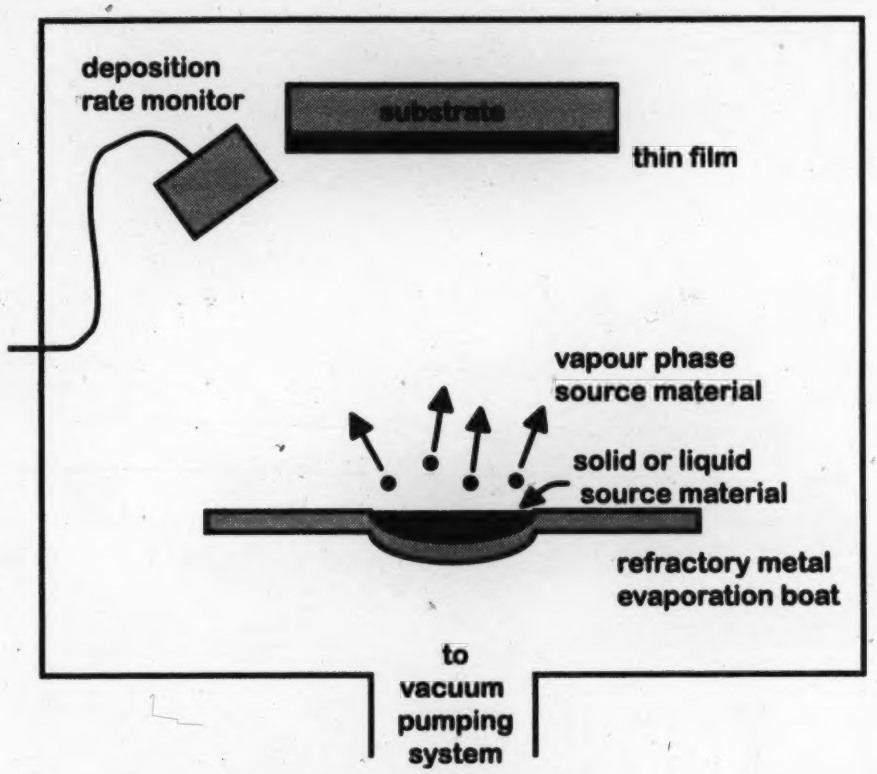

Figure 1: Thin film deposition by evaporation. The deposition rate monitor is a quartz-oscillator microbalance connected to an external controller. Background gas pressures are typically below 10^{-5} Torr (10^{-3} Pa).

heating, a high energy electron beam, typically 5-10 kV, is directed at the solid source material placed within a cooled hearth. Upon impact, the energy of the electrons heats the source material (the melt) and causes it to evaporate. Cooling of the hearth limits heating of the crucible, which holds the melt. Electron beam deposition eliminates the interaction between the source material and evaporation boat that can be problematic with resistively heated evaporation. Much higher temperatures can be obtained, allowing evaporation of materials which cannot be deposited by resistively heated evaporation. Electron beam evaporation is the evaporation technique of choice for producing high quality films. For the purposes of GLAD, either technique can be used, but care must be taken to keep the vapour source small in cross-section to reduce the angular spread of vapour flux arriving at the

substrate (See "variation of vapour incidence angle" on page 27.).

A very common PVD technique called 'sputtering' was not used in this thesis but will be briefly discussed [121]. Sputtering employs a glow discharge, or plasma, of a low pressure (~10^{-2} torr) inert gas, typically argon, to produce heavy ions (Ar+). A large negative voltage is applied to the source material, on the order of -100 to -500 volts, causing the argon ions (Ar+) to be accelerated toward the source material. Upon impact, they atomistically eject source material through a momentum transfer process. Ejected atoms travel through the vacuum to the substrate, and condense to form the thin film. The mechanics of film formation with sputtering are quite similar to those of evaporation, with differences arising from plasma effects, more energetic vapour flux, and higher background pressure from the working gas (the argon). The primary advantage of sputtering is that it allows the deposition of film materials not possible with evaporation techniques. Initial results indicate that the directionality of the vapour flux from a sputter source, and the narrow angular distribution obtainable through techniques such as long-throw low-pressure sputtering, should allow GLAD effects to be exploited with sputtered film materials [110].

2.2 Thin Film Structure

As the first vapour atoms (or molecules) arrive and condense on a bare substrate, growth of the thin film begins, and many physical processes influence the growth. There are significant differences between the physics at the beginning of growth, broadly called nucleation, where the vapour is arriving onto a mostly bare substrate; and later stages of growth, where the vapour is arriving onto previously deposited film material, called bulk growth. Nucleation effects are the result of the interface physics, between the accumulating film and the substrate - typically different materials. Once film growth has progressed past initial nucleation, and the majority of the substrate surface is coated, film-on-film bulk growth processes dominate. For the large majority of the films discussed in this thesis, atomic shadowing and surface diffusion of adatoms are the dominant bulk growth mechanisms, although other effects such as facetting and bulk diffusion have minor contributions.

There are many aspects of thin film structure, including physical morphology

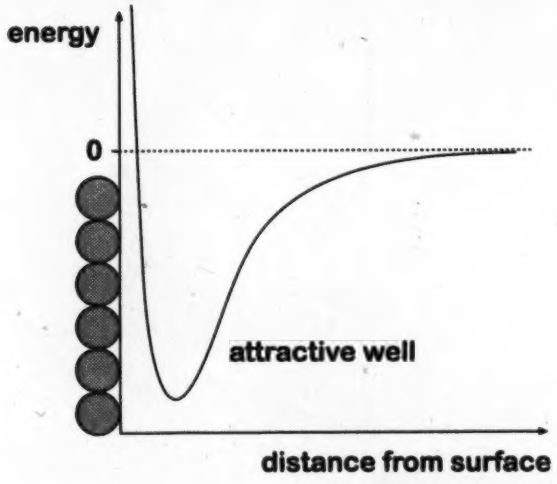

Figure 2: Surface potential energy well arising from surface excess energy. Atoms trapped in the well are physisorbed and have some freedom to move across the surface to find preferred bonding sites.
This figure is from Ball [7].

(shape/geometry), crystal structure, and compositional structure. The majority of the following discussion of GLAD films and materials relates to the physical morphology of the deposited film material. GLAD techniques will have some effect on crystallinity and compositional structure; however, this thesis concentrates on the effects of GLAD on film morphology, and techniques which can be used to control film morphological architecture. A few comments on the effects of GLAD on film crystallinity are given in "transmission electron microscopy" on page 46.

2.2a) nucleation

As a vapour atom (or molecule) from the deposition vapour approaches the substrate surface, it encounters a energy potential function (Figure 2) arising from the excess energy of the free bonds of the atoms on the surface. There is a small potential well (attractive), with little or no potential barrier, a small distance from the surface. An atom on the surface (an adatom) sitting in this potential well is said to be in a physisorbed state, and has relative freedom to move across the surface [1,7,75]. For the atom to move closer to the surface it must surpass a potential barrier. It then enters a chemically bound state and becomes essentially fixed in location on the surface. The form of the potential function

(Figure 2) varies greatly with substrate and film materials, and with position on the surface. Discontinuities, such as defects and step edges, have smaller energy barriers and, therefore, induce preferential growth.

When adatoms arrive on a bare substrate, they initially occupy physisorbed states and diffuse along the surface. If they have enough energy to surpass the potential barrier at their current position, they bind with the substrate and become fixed in place. The probability of surpassing the barrier depends on the energy of the adatom and surface and on the size of the barrier (which in turn depends on the substrate and film materials, and the local geometry). For any surface/film/temperature combination there is also a finite (possibly very small) probability that the adatom will re-evaporate from the surface. For each vapour atom approaching a surface, there are essentially three results that can occur: 1) it can reflect immediately; 2) it can enter a physisorbed state, move across the substrate for a finite time, and then enter a bound state and become permanently fixed on the surface; 3) it can enter a physisorbed state, move across the substrate for a finite time, and then re-evaporate from the surface.

While adatoms are diffusing across a substrate surface in physisorbed states, they are attracted to one another and come together to form nuclei of small numbers of atoms. Small nuclei have a large ratio of surface area to volume, and consequently a large (relative) probability that the nuclei will reevaporate. As nuclei size increases, the probability of reevaporation decreases, until at the 'critical nuclei' size, the nuclei are more likely to remain on the surface than reevaporate. The first stages of film growth are dominated by the movement of adatoms on the surface, and the formation of nuclei growing to be larger than the critical size (Figure 3). Once the surface is covered with many super critical nuclei, most adatoms will remain on the surface, and condense to form the thin film. Growth progresses as the nuclei expand to cover remaining bare substrate. Eventually nuclei begin to touch (coalescence) and film on film growth begins. An interesting aspect of the GLAD process described in this thesis is that coalescence and the formation of a continuous film can be suppressed by extreme shadowing. Even during the nucleation stages of film growth, the extreme oblique deposition used with GLAD leads to strong shadowing effects which in turn create significant perturbations from the typical thin film growth mechanics.

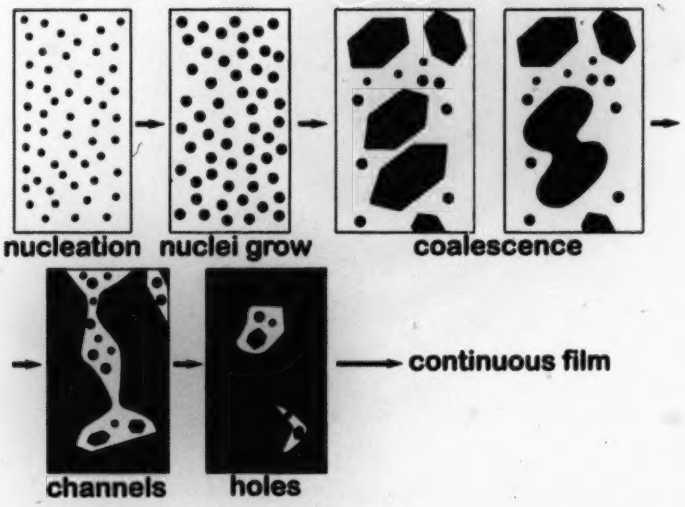

Figure 3: Film nucleation and coalescence. Critical nucleation occurs when the average nuclei size exceeds the size where a nuclei is equally likely to remain on the surface or reevaporate. Coalescence and the formation of a continuous film is suppressed by the extreme shadowing created by the GLAD deposition process.
This figure is from Maissel and Glang [75].

2.2b) adatom diffusion and shadowing

Once the nucleation stage of film growth has produced a fairly complete covering of the substrate, film/substrate interfacial physics no longer directly affect film growth. Indirectly however, through the resulting size, density, and crystallinity of nuclei, nucleation physics do have residual effects on the resulting bulk film structure and growth mechanics. Three physical processes typically dominate the majority of bulk film growth by physical vapour deposition: 1) atomic (or geometrical) shadowing; 2) adatom (or surface) diffusion; and 3) bulk diffusion (Figure 4). For the large majority of films discussed in this thesis, atomic shadowing and adatom diffusion dominate, while bulk diffusion is minimal or non-existent. Bulk diffusion is the bulk annealing of film material deposited onto significantly heated substrates. High temperatures provide enough energy to enable diffusion of atoms and defects within the bulk of the film, and across grain boundaries. As all films discussed in this thesis were deposited onto unheated substrates,

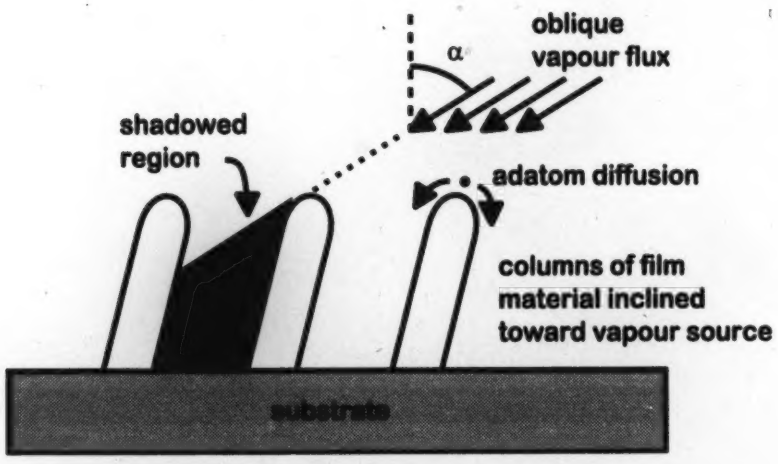

Figure 4: Shadowing and adatom diffusion. Atomic (geometrical) shadowing prevents vapour flux from arriving in areas 'behind' previously deposited film material (shadowed region). Deposition under conditions of limited adatom diffusion prevents any film material from reaching the shadowed regions. The shadows become voids in the final film structure.

well below the melting temperatures of the film material, temperatures were typically too low to activate bulk diffusion.

Adatom (or surface) diffusion is the motion of adatoms, across the surface of the film, while in a physisorbed state. Because of the excess energy of a rough or textured surface, adatoms preferentially 'fill in' voids [8]. Or, equivalently, the energy barrier to surface bonding for an adatom is less at defect sites and step edges. There are effects that lead to surface roughening [8], but adatom diffusion substantially tends to smooth film structure. The average distance that an adatom will diffuse on the film surface (adatom diffusion length) is controlled by the energy of the adatom, the binding energetics of the film material, and the deposition (burial) rate by the vapour flux. A rough measure of the effective diffusion length can be taken from the ratio of the film temperature during deposition (T), which gives a measure of the energy of the adatom, and the bulk melting temperature of the film material (T_m), which gives a measure of the binding energetics of the film material. Structure zone models [121,90,79] used in description of thin film structure are based on this 'reduced temperature' ratio (T/T_m) (Figure 5). The ratio gives an

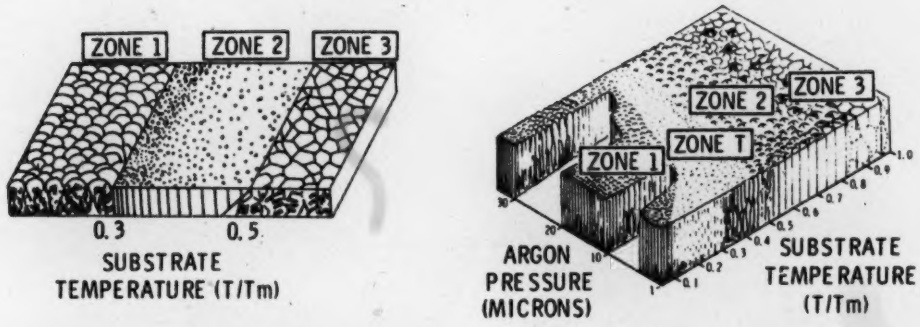

Movchan and Demchishin model **Thornton model**

Figure 5: Structure zone models proposed by Movchan and Demchishin [86], and Thornton [121] for predicting film structure for varying reduced temperature (T/T_m - both in Kelvin) and background pressure (for sputtered films). Structure is classified by zones of dominant growth mechanism. *This figure is from Movchan and Demchishin [86] and Thornton [121].*

estimate of the adatom diffusion length and gives a good qualitative prediction of film structure. However, there are differences that arise for varying material types. The structure zone models are based on observations of thick metal films, and direct comparisons of the model to metal oxide, metal fluoride, and semiconductor films can be inaccurate. This will be discussed in more detail later.

A more recently developed structure zone model [79,81] incorporates the effects of evolution of structure, and attempts provide a framework for quantitative description of the fractal nature of low temperature thin film growth. While not as extensively studied as the earlier structure zone models, the evolutionary model does provide improvements in the description of film structure. Many levelled bundling of columnar structure from atomic to macroscopic scales is described, and attributed to evolutionary growth effects and adatom mobility induced by various effects, including temperature, bombardment, and chemistry. The complexity and fractal nature of film structure is discussed, and Messier summarizes, "Since thin film morphology is apparently a random fractal that is expected to be modified by both temperature and bombardment, a generally concise description should not be expected." [81]. Because of the lack of a comprehensive model of thin film structure, I will

use the simplified structure zone model descriptions to illustrate film structure and the relevant physical processes of growth. When warranted, however, I will go beyond the simplifications of the early structure zone models (for example, See "transmission electron microscopy" on page 46.).

The 'atomic shadowing' effect occurs when areas of previous film growth prevent vapour flux from impinging on areas which are in their shadows (Figure 4). As the vapour flux arrives atomistically in linear trajectories, shadowing can prevent any area which is 'behind' previously deposited material from receiving material flux. Surface and bulk diffusion are able to fill the shadowed regions with film material if the adatoms can diffuse far enough to reach the shadowed regions. The structure zone models of Figure 5 separate film structure into zones where the dominant growth mechanisms are atomic shadowing, adatom diffusion, and bulk diffusion, in zones 1, 2, and 3 respectively. The zones are defined as ranges of the reduced temperature, T/T_m, with shadowing dominating at low temperature ($T/T_m < 0.3$) and bulk diffusion dominating at high temperatures ($T/T_m > 0.5$). All films described in this thesis were deposited onto unheated substrates placing their predicted structure in zone 1, with atomic shadowing dominating (T/T_m for Cu at room temperature = 300/1400 = 0.21). While the substrate was always at room temperature at the beginning of the deposition, heating from the evaporation source, and from condensing film material, typically heats the substrate and film to hundreds of degrees above room temperature [73]. This results in significantly increased adatom diffusion in some instances, and resulting changes in film growth.

2.2c) columnar structure

When a film is deposited onto a low temperature substrate (zone 1 : $T/T_m < 0.3$), atomic shadowing dominates adatom diffusion in determining the resulting structure. Adatom diffusion is minimal, and atoms are incorporated into the film very close to their point of impact. Shadowing effects can not be mitigated by diffusion into shadowed areas. This leads to a columnar film structure where the boundaries or voids between columns cannot receive flux (Figure 6). The resulting film is normally composed of approximately cylindrical shaped columns of material, separated by voids. Note that crystalline texture is not necessarily the same as columnar structure and that individual columns can be

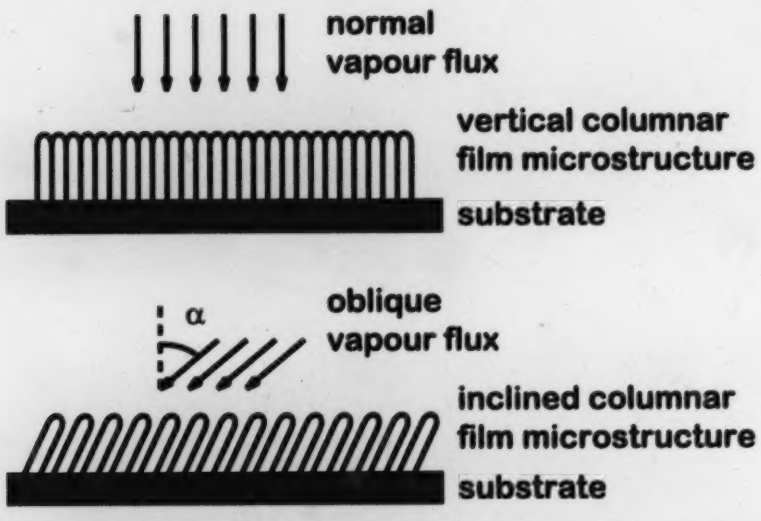

Figure 6: Most films deposited onto low temperature substrates (zone 1 : T/Tm < 0.3) exhibit columnar film structure. When the vapour flux arrival angle is made oblique ($\alpha > 45°$), the columnar structure becomes porous and inclined toward the vapour source.

amorphous, polycrystalline, or monocrystalline. Columnar structure is observed in most zone 1 films.

2.3 Oblique Deposition

That oblique deposition affects film properties was first observed by Knorr and Hoffmann [61] and Smith [112]. Smith observed variation in the magnitude and direction of magnetic anisotropy in permalloy films with variation in flux arrival angle. Smith then proposed that the origin was shadowing: "the area behind a crystallite is left vacant because it is in the crystallite's shadow" [113]. Later work showed that oblique deposition affects most observable properties of deposited films including stress [101,62], optical birefringence and dichroism [113,55,115,46,24,85,64,77], electrical anisotropy [119,40,95,2,63,92], magnetic anisotropy [113,112,24,63] density [119,95], composition [60], electrochromic behavior [37,131], and fluid transport [45].

Generally, thin film deposition is performed with the majority of the vapour flux arriving along a trajectory normal (perpendicular) or near normal to the surface of the

substrate. Structure zone models (Figure 5) of thin film growth do not account for variations in flux arrival angular distributions, yet they exhibit their effect to some degree. The extension of Zone 1 structure to higher T/T_m ratios for high argon pressure, in the sputtering zone model proposed by Thornton (Figure 5) [121], is a direct consequence of the broadening of the angular distribution of the vapour flux due to randomizing collisions with the background gas. More vapour flux arrives at an oblique angle, creating more shadowing, and resulting in a more porous film structure. Atomic shadowing caused by surface roughness is also strongly enhanced with oblique incident flux, resulting in structures that are more voided and porous. This effect has been considered as undesirable in most thin film applications, where uniform coatings of complex structures or filling of topography is desired.

Many interesting and potentially useful results occur when flux distribution is intentionally tailored to include a large oblique component. To begin the analysis of the effect on film structure of varying the oblique component in the vapour flux, I will describe the effects of varying the polar angle α from which the vapour flux arrives, from a point source evaporation source, onto a stationary substrate. The flux distribution can be considered as a point source in vacuum for the majority of the work discussed in this thesis due to the small size of the vapour source, the large source-substrate spacing, and the low background gas pressure. Typical angular spreads of arrival angles were less than 5°. As shadowing is enhanced for oblique arriving flux, the consequences of the shadowing effect become more pronounced for larger α. Enhanced shadowing results in formation of isolated columns of film material, inclined toward the vapour source, with diameters comparable to the adatom diffusion length. The film becomes more voided (less dense) as α is increased. One-sided oblique deposition also creates different shadowing characteristics parallel and perpendicular to the deposition plane (the deposition plane contains the vapour incidence vector and the substrate normal) (Figure 7) resulting in structural anisotropy in the deposited film [1,60,118].

2.3a) column inclination

As α is increased and the deposition flux becomes more oblique, growth occurs on the faces of the domed column tops facing the vapour source, and the zone 1 columnar

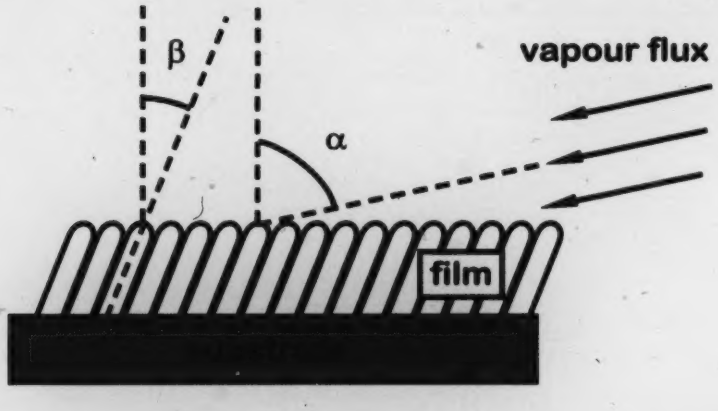

Figure 7: Column inclination angle β lies between the substrate normal and the vapour incidence angle α.

structure begins to become inclined toward the source of the vapour (Figure 7). Numerous works discuss the relationship between the angle α, between the vapour flux direction and the substrate normal, and the angle β, between the column growth angle and the substrate normal [28,117,88] (Figure 8). The tangent rule,

$$2\tan\beta = \tan\alpha, \tag{1}$$

is an expression determined experimentally for evaporated aluminum for near normal deposition ($\alpha < 30°$) [88]. The expression states that the column growth direction lies between the vapour flux direction α and the substrate normal. Fair agreement with observed column growth angles is seen for $\alpha < 60°$. Above $\alpha > 60°$, the tangent rule predicts column angles larger than is observed in real films. Other relationships have been proposed, but the most accurate and most useful to date is the relationship based on a geometrical analysis proposed by Tait [117]. The analysis assumes: 1) a film structure comprised of inclined columns with hemispherical tops, 2) a distance in which the incoming flux is captured by the growing column, and 3) minimal surface diffusion, and yields the expression:

$$\beta = \alpha - \text{asin}\left[\frac{1-\cos\alpha}{2}\right]. \tag{2}$$

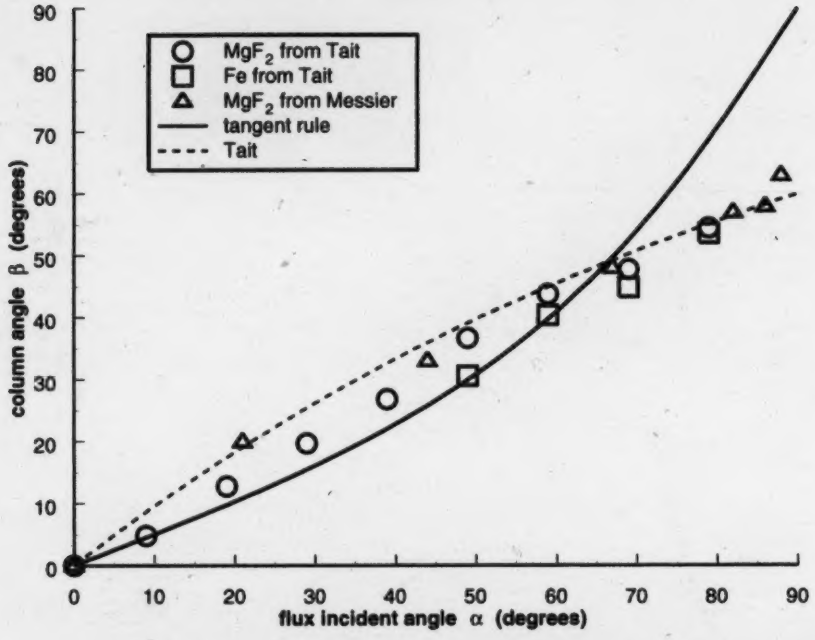

Figure 8: Column inclination β varies with vapour incidence α, and material. The 'tangent rule' [88] is shown, as well as a rule proposed by Tait [117]. Experimental data from Tait [117] and from Messier [80] agrees with Tait's rule, particularly at large vapour incidence angles α.

There is some discussion, in the literature, of the accuracy of this expression in predicting actual film structure, with Tait showing only fair agreement with MgF_2 and Fe films for $\alpha < 60°$. A more recent comparison [80] shows very strong agreement for MgF_2 films for α ranging from 0° to 89°. A recent review by Abelmann [1] discusses the many second-order factors that affect column growth angle, such as surface contamination, deposition rate, parallel momentum and biased diffusion, and temperature. Abelmann gives a comprehensive review of experimental and theoretical work investigating oblique deposition, particularly relating to surface (adatom) diffusion and column inclination. He discusses a model proposed by Hara et al. [40,41] in a series of papers where adatoms preferentially diffuse along their impingement direction. Predicting column inclination accurately appears to be a complex problem affected by many factors; Abelmann summarizes: "It is concluded that the Hara model does seem to be approximately correct

and that at least qualitative predictions are possible". Tait's expression (2), however, gives good approximate results for at least some film materials.

2.3b) density

Because shadowing is strongly affected by vapour incidence angle, variation of α also affects the density of the resulting film. As α is increased to very oblique, the columnar structure becomes more and more voided as shadowing from one column forces columns behind it to be farther away. This results in undesirable, highly porous, films when attempting to cover topographical features in integrated circuit manufacturing. Tait [119], for example, shows how W films sputtered over topographical features have a low density porous structure on highly sloped regions such as via sidewalls. Tait also [117] developed an expression (based on geometrical analysis) relating the spacing of columns to the vapour incidence angle. A more detailed description of the effects of oblique deposition on density is given in "extreme oblique deposition" on page 20, and in "variation of vapour incidence angle" on page 27.

2.3c) structural anisotropy

When vapour flux arrives perpendicular to the substrate ($\alpha = 0°$), the film material arrives symmetrically, and shadowing produces no anisotropic effects. As the flux angle α is made oblique, the asymmetry in the vapour distribution produces asymmetric (or anisotropic) shadowing, leading to anisotropic film growth. The anisotropy in film growth produces anisotropies in all observable film properties including stress, optical birefringence and dichroism [45], magnetic susceptibility [59], and fluid transport [45]. Two types of structural anisotropy are observed in obliquely deposited films. Strong shadowing in the deposition plane, and comparably less shadowing perpendicular, produces a structure with a larger columnar separation in the deposition plane and produces a 'bundling' of columns perpendicular to the deposition plane [1]. The second type of anisotropy is observed in cross-sectional shape of the columns. Columns in general have elliptical cross-sections with the long axis of the ellipse either parallel or perpendicular to the vapour incidence plane. This effect is reviewed in Abelmann [1] and is attributed to effects related to conservation of momentum of the vapour atoms.

The degree of observed anisotropy is strongly dependent on vapour incidence

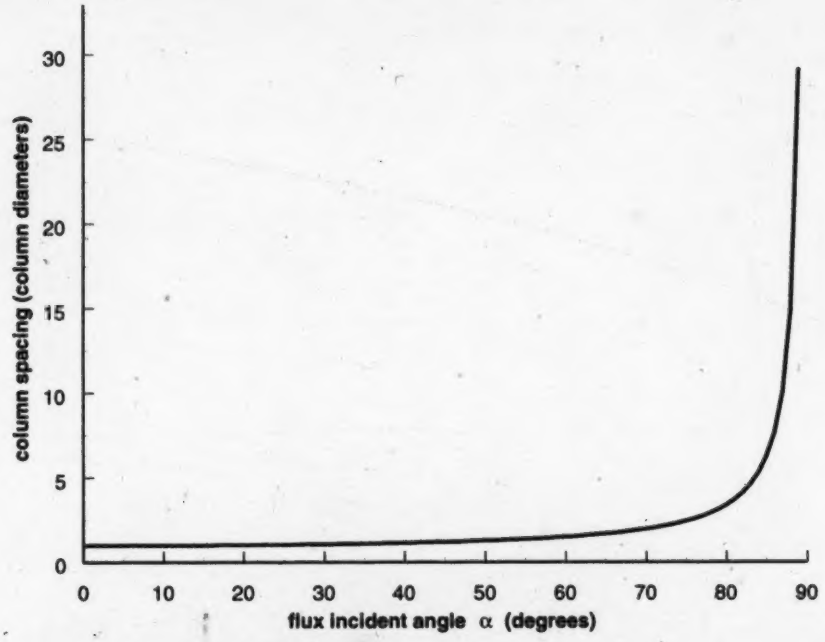

Figure 9: Column spacing as derived by Tait [117] graphed to a vapour incidence angle $\alpha = 89°$.

angle, material, and deposition conditions. Hodgkinson [45] has demonstrated a variety of novel optical filters based on birefringence induced by oblique deposition, and tailored by variation of vapour incidence angle. Polarization selective mirrors and interference filters were recently demonstrated [78].

2.3d) extreme oblique deposition

When the vapour arrival angle is made very large ($\alpha > 80°$), significant changes result in film structure. Tait [117] developed an expression:

$$a = \frac{1}{2} \cdot \left[1 + \frac{1}{\cos\alpha} \right], \tag{3}$$

relating column spacing a, in column diameters, to incidence angle α that displays this effect. In [117], Tait plotted expression (3) to $\alpha = 80°$ and didn't display the extreme oblique regime. When the expression is plotted to $\alpha = 89°$ (Figure 9) it is apparent that there is a significantly different region of film growth when the flux arrival angle is restricted to

extremely oblique. For the most part, the columns forming the inclined film structure remain in contact until the flux angle is increased beyond about 75°. Beyond this, the column spacing quickly approaches infinity at $\alpha = 90°$. This growth is very different than the growth that occurs at smaller angles, of α, and this regime forms the basis for Glancing Angle Deposition. It is interesting to note that while the column spacing *a* approaches infinity as α approaches 90°, the column growth angle β asymptotically approaches a finite value of approximately 60°. This allows column spacing to be controlled in porous films largely independent of variation in β, if the arrival angle α is maintained at an extreme value.

Another effect seen in extreme oblique deposition is that columnar structure is observed in film materials that would form uniform dense coatings at nearer normal incidence. SiO, for example, produces a dense, and almost structureless film, when deposited at any vapour incidence angle less than about 70°. Above 70°, however, SiO exhibits a columnar structure very similar to that observed in MgF_2 and other column forming materials. Extreme shadowing created by highly oblique incidence creates a new film growth regime where shadowing suppresses coalescence of the film. This will be discussed in more detail in the next chapter during the discussion of the effects of varying the vapour incidence angle with GLAD (See "variation of vapour incidence angle" on page 27.).

2.4 Substrate Motion

All the physical effects resulting from oblique deposition are strongly dependent on the arrival direction of the vapour flux. Both the polar angle α and the azimuthal orientation ϕ affect film growth direction and structural anisotropy. By varying the orientation of the substrate relative to the vapour source (α and ϕ), the arrival direction can be easily controlled . If the substrate orientation is varied during deposition, film structure can be controlled. Equivalently, the orientation of the vapour flux could be controlled by moving the vapour source, but moving the substrate is much simpler.

Structural control with substrate motion was first demonstrated in 1966 by Nieuwenhuizen and Haanstra [88] when they deposited an Al film with a chevron structure.

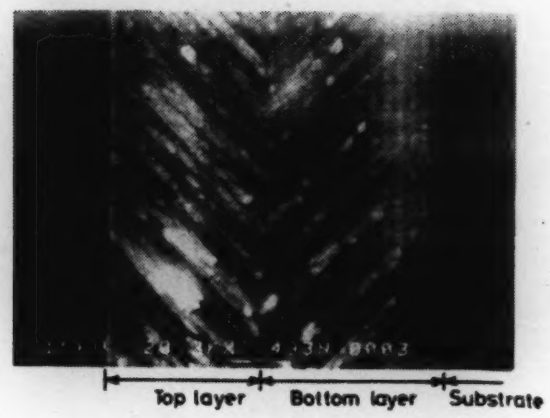

Figure 10: Chevron film structure fabricated by Motohiro and Taga [85].
This figure is from Motohiro and Taga [85].

They deposited a film at an oblique angle α for the first half of the deposition and $-\alpha$ for the last half; the substrate was rotated through an angle 2α about an axis parallel to the substrate and perpendicular to the deposition plane. Because film growth from oblique incident flux is inclined toward the vapour source, when the vapour source direction was changed by 180° (in ϕ), film growth followed. The resulting structure had a chevron or zigzag shape in cross section (Figure 10). Motohiro and Taga [116,84,85] investigated the chevron structure and interface in detail for various metal oxides and measured optical birefringence of multilayer chevron films. The substrate motion required for depositing chevron films is simple and can be described in two ways: 1) the substrate is rotated about an axis parallel to the surface and perpendicular to the deposition plane (α rotation in Figure 11), this varies α to $-\alpha$ in a 2α rotation; 2) the substrate is rotated 180° in ϕ, about an axis perpendicular to the substrate surface. Hodgkinson and Wilson [45], exploiting the α dependent optical anisotropy, deposited many layers varying α from layer to layer.

GLAD exploits the effects discussed in this chapter, namely atomic shadowing with limited adatom diffusion, and inclined growth toward the vapour source, to engineer desired structures in porous thin films for technological application.

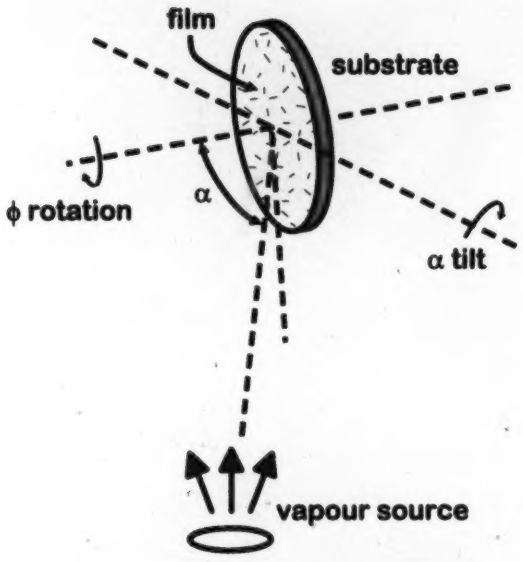

Figure 11: Glancing Angle Deposition (GLAD) geometry defining vapour incidence angle α and substrate azimuthal rotation ϕ.

3. Glancing Angle Deposition

While investigating the fabrication of very porous film structures by oblique deposition from multiple sources, or with substrate motion, I produced an interesting zigzag microstructure [Figure 12c][95]. Unlike the chevron structures investigated by Nieuwenhuizen and Haanstra [88], and Motohiro and Taga [85], the zigzag structure was produced within the extreme oblique deposition regime (See "extreme oblique deposition" on page 20.) with the vapour arrival angle α set at +/- 85°. The resulting film had a porous structure composed of *isolated* zigzag shaped columns instead of the dense structure with a zigzag or chevron microstructure which had been created previously. The observed film structure suggested that the structure of individual columns of film material with nanometre dimensions could be controlled with substrate motion if the flux angle was kept extremely oblique.

With publication of the single column controlled structure [95], there was much interest in the research community. The ability to create materials with controlled structure on a nanometre scale with substrate motion was recognized as a powerful technique, and many materials researchers expressed interest, and proposed structure and application ideas. Azzam [5] and Lakhtakia and Weiglhofer [65] had previously discussed using substrate motion and oblique deposition to produce materials with helical structures resulting in optical properties similar to chiral liquid crystals. Both works were theoretical in nature and neither recognized the importance of extreme oblique incidence. Azzam envisaged a dense structure with a uniaxial in-plane anisotropy perpendicular to the deposition plane. With rotation of the substrate, this anisotropy would rotate to produce a helical inhomogeneity very similar to that observed in chiral liquid crystals. Lakhtakia and Weiglhofer expanded the idea proposed by Azzam and investigated the optical properties of the theoretical 'helicoidal bianisotropic mediums' - a general description for helical complex mediums. Upon reading the work containing the isolated column zigzag results, Lakhtakia suggested that helical structures would be significant, and soon after I fabricated a film with helical shaped columns [Figure 12d][97].

The nanometre scale structural control that is possible with the combination of extreme oblique deposition and substrate motion suggests the possibility of numerous

applications of this technique in optical, chemical, biological, electrical, and other fields. We discuss a number of these possible applications in Lakhtakia et al. [70] and I will describe progress toward the experimental realization of some in the later chapters of this thesis.

In this chapter, I will discuss the mechanics of GLAD growth. Much of the discussion of oblique deposition is relevant to GLAD growth, but the combination of extremely oblique deposition and substrate motion creates some unique effects. GLAD also provides new insight into film growth mechanics, allowing a more direct observation of adatom diffusion than is possible with less oblique deposition. I will discuss the development of deposition equipment needed to produce and investigate GLAD films. A number of different techniques for substrate motion control were used and the characteristics of each are presented. Capping of the porous structure produced with GLAD with a dense slab or lid is desired for many applications. For some film structure, this can be difficult, and I will describe various techniques to accomplish capping. Finally, I will present various application possibilities for GLAD and initial feasibility studies.

3.1 Growth Mechanics

3.1a) stationary, zigzag, helical, post

Figure 12 illustrates the progression, of film structure, from stationary substrate normal deposition, to oblique deposition, and then to GLAD, and shows some of the basic structures obtainable with the GLAD technique. All films are MgF_2 (magnesium fluoride) deposited onto Si (silicon) or glass substrates. Figure 12a was deposited with the vapour flux arriving normal to the substrate ($\alpha = 0°$). The film structure is dense with columns oriented normal to the substrate ($\beta = 0°$). Figure 12b was deposited with the vapour incidence angle $\alpha = 85°$ onto a stationary substrate. The resulting structure is porous and composed of isolated columns, with diameters on the order of 100 nm, inclined toward the vapour source (to the right). Note that the column inclination angle β is not equal to the vapour incidence angle α; it is substantially less (for $\alpha = 85°$, $\beta \sim 60°$). This is in agreement with the analysis developed by Tait [117], discussed in "column inclination" on page 16. Figure 12c is the zigzag film of isolated columns discussed in the introduction to this

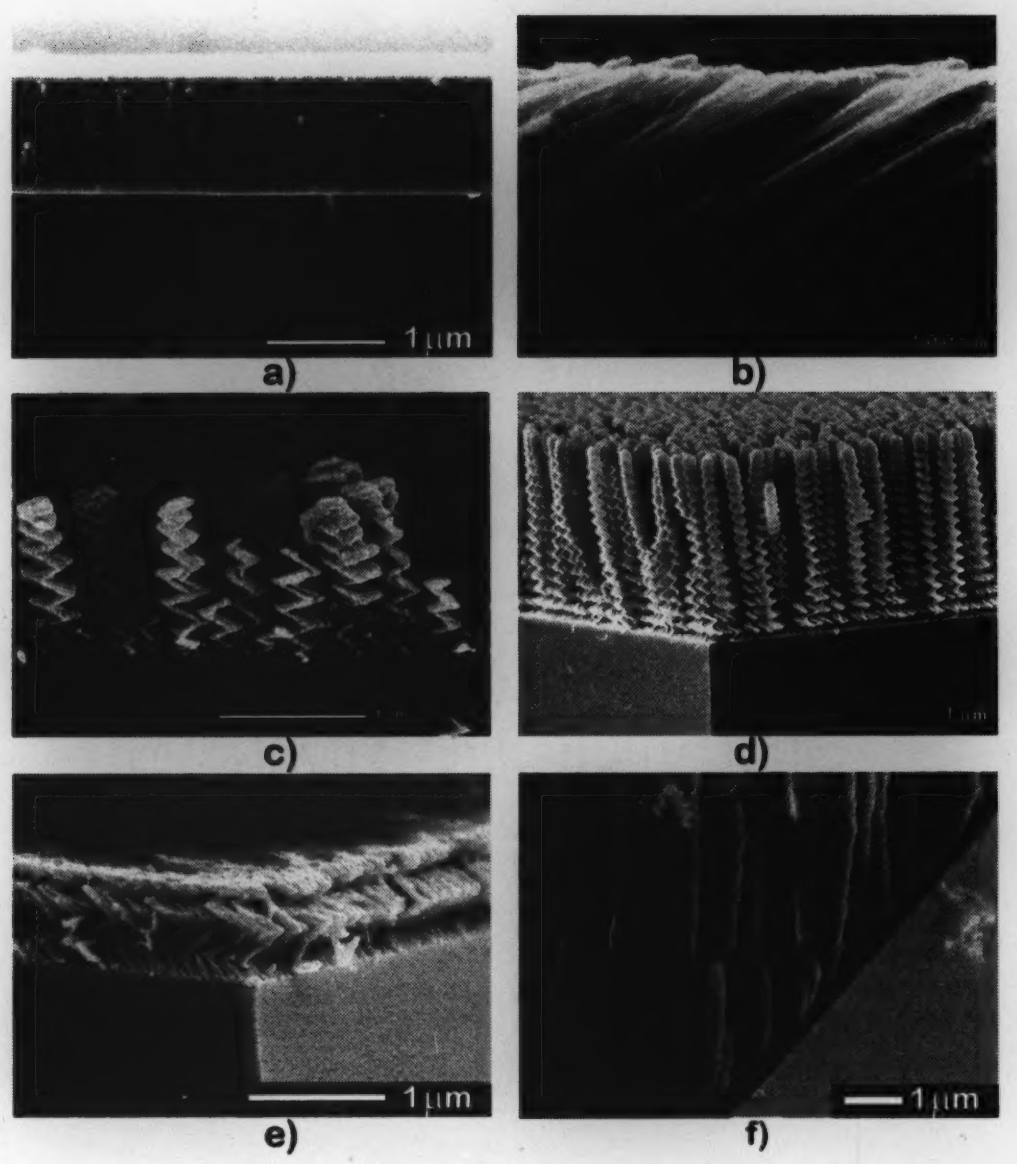

Figure 12: MgF_2 films deposited with techniques demonstrating the progression from normal deposition to oblique deposition to GLAD. The films were deposited with: a) normal deposition, b) oblique, one-sided deposition, c) alternating oblique deposition, d) continuous substrate rotation ϕ, e) 90° per step stepwise substrate rotation in ϕ, and f) rapid substrate rotation ϕ. Films b) through f) were deposited with a vapour incidence angle $\alpha = 85°$.

chapter. Deposition was alternately from the left and right at a vapour incidence angle of α = 85°. The film growth is seen to follow the changing direction of deposition, and individual columns are formed into zigzags. Figure 12d shows a film composed of helical shaped columns resulting from a continuous rotation of the substrate (ϕ rotation) during deposition while the vapour incidence angle was kept fixed at α = 85°. Films of this type have interesting optical properties. They interact strongly with circularly polarized light, leading to optical rotation and Bragg reflection effects (See "Chiral Optics" on page 81.). Figure 12e shows a film which demonstrates the effect of stepwise motion; it was deposited with a technique that is a combination of the techniques used in the zigzag and helical films. The substrate was rotated (ϕ) in 90° steps followed by pauses for deposition. The vapour incidence angle was kept fixed at α = 85° at all times. This produced a 'stepped helix' structure where the overall helical structure is composed of four straight edges per rotation. Decreasing evaporation rate during deposition resulted in smaller edges toward the top of the film. Finally, Figure 12f demonstrates the 'post' structure which will be discussed later in this thesis. Rapid rotation of the substrate during deposition, with the vapour incidence angle α fixed, produced a columnar structure with porosity specified by the choice of α. The rotation rate was high enough that the helical structure was largely eliminated. As a guideline, for the formation of a 'post' structure, the rotation rate must be high enough that one complete substrate revolution occurs in the time that a film is deposited with thickness equal to the average adatom diffusion distance. For rotation rates equal to or greater than this rate, 'post' structure will be produced.

3.1b) variation of vapour incidence angle

In the MgF_2 films of Figure 12, the vapour incidence angle α was kept constant for the entire duration of the thin film deposition. Here I describe the effect of varying α. It is important to note in this discussion that there is a finite width in the angular distribution of the vapour arriving at the substrate, arising from the finite size of the evaporation source. SiO films were deposited from a sublimation source (R. D. Mathis Co. "Baffled Box SiO Sources" - SM16), with a 13 mm diameter circular opening. Most other film materials were deposited from a resistively heated W, Mo, or Ta foil evaporation boat with a 25 mm diameter or smaller circular pocket (R. D. Mathis Co. - S29). The separation between the

evaporation source and the centre of the substrate was 31 cm. The finite size of the evaporation source results in a width of arrival angles α of the vapour of about 6° across a three inch wafer for $\alpha \sim 80°$, for the large boat sources, and about 4° for the sublimation source. All vapour incidence angles, α, discussed here are measured from the centre of the evaporation source to the centre of the substrate.

As α determines the amount of shadowing, when α is kept constant, effects dependent on shadowing remain constant throughout the deposition. Column spacing, film density, and column growth angle remain substantially the same through the entire thickness of the film. To qualify the effect of variation of α, I began with a study of film structure for α maintained constant during each single deposition, but varying from one deposition run to the next. Figure 13 and Figure 14 show the effect of varying α for three films each of two materials, deposited at varying α. Figure 13 shows two micrographs each of three films of SiO deposited at 75°, 85°, and 88°. Figure 14 shows two micrographs each of three films of CaF_2 deposited at 75°, 85°, and 88°. The images a) and b), c) and d), and e) and f) are different views of the same film for each of the two figures. The two micrographs for each of the six films are taken at equal viewing angles and magnifications to facilitate comparison (a), c), and e) and b), d), and f) are the same view respectively). It is apparent from the figures that column spacing and film density are strongly dependent on vapour incidence angle α. When α is more normal (75°), the film structure is more dense, with less space between columns. As α is increased to more oblique (88°), the film becomes very porous with large column spacing and corresponding large voids. As α approaches 90°, small changes in α result in large changes in film structure as evidenced by the substantial difference in film structure between the films deposited at $\alpha = 85°$, and at $\alpha = 88°$. This is in agreement with the relationship for column spacing developed by Tait [117] and discussed in "extreme oblique deposition" on page 20.

The densities of these films, and others deposited at various angles and composed of various materials, were measured with a microbalance mass measurement technique. A small portion of the film and substrate (approximately 2 cm x 2 cm) was weighed on a 1µg accuracy balance. The film was then etched from the substrate and the substrate was reweighed. The difference in measured mass was taken as the mass of the film material, and

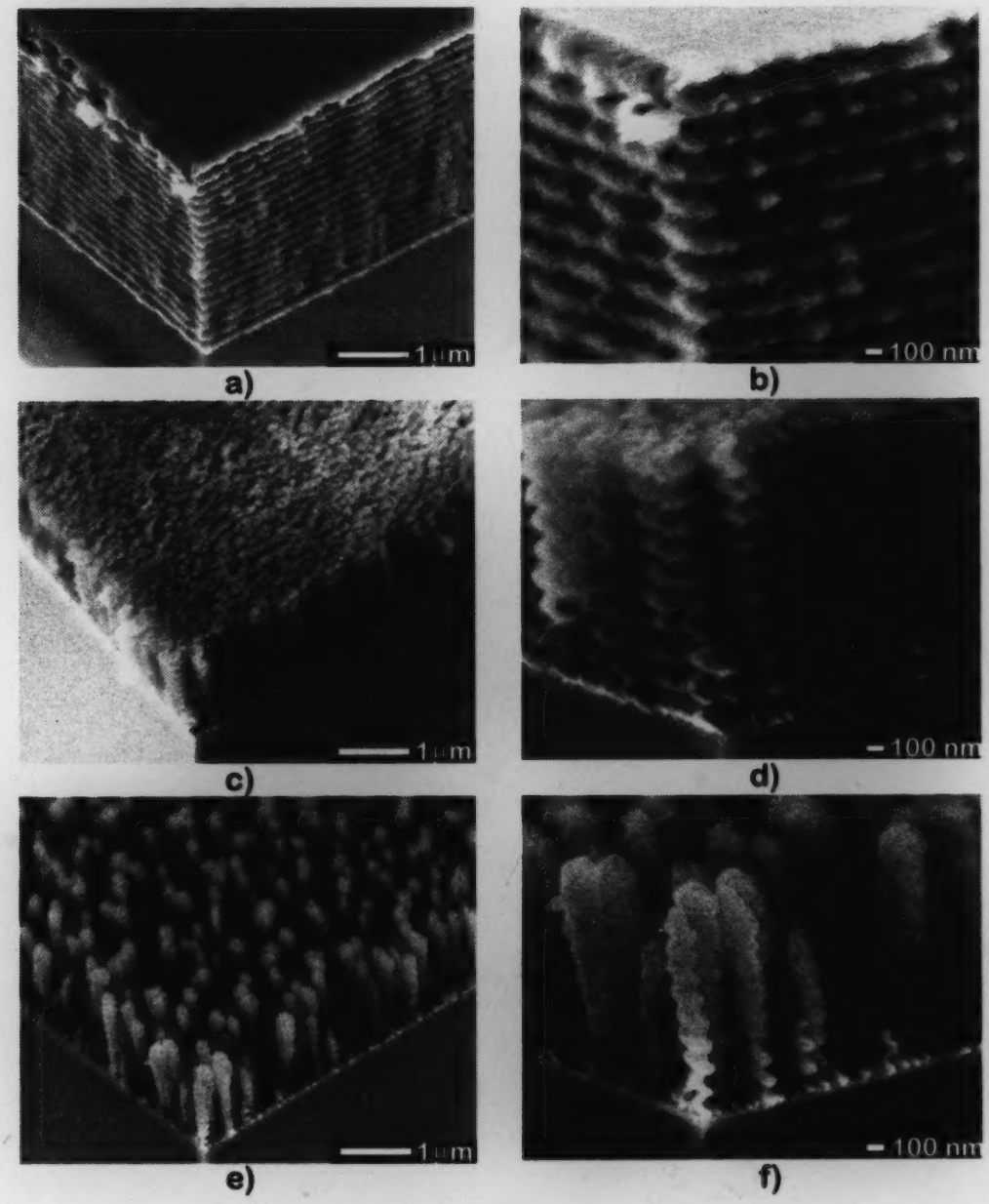

Figure 13: Three SiO films deposited at $\alpha = 75°$, 85°, and 88°. The film shown in a) and b) was deposited with $\alpha = 75°$. The film shown in c) and d) was deposited with $\alpha = 85°$. The film shown in e) and f) was deposited with $\alpha = 88°$. Micrographs a), c), and e) are equal viewing orientations and magnifications as are b), d), and f).

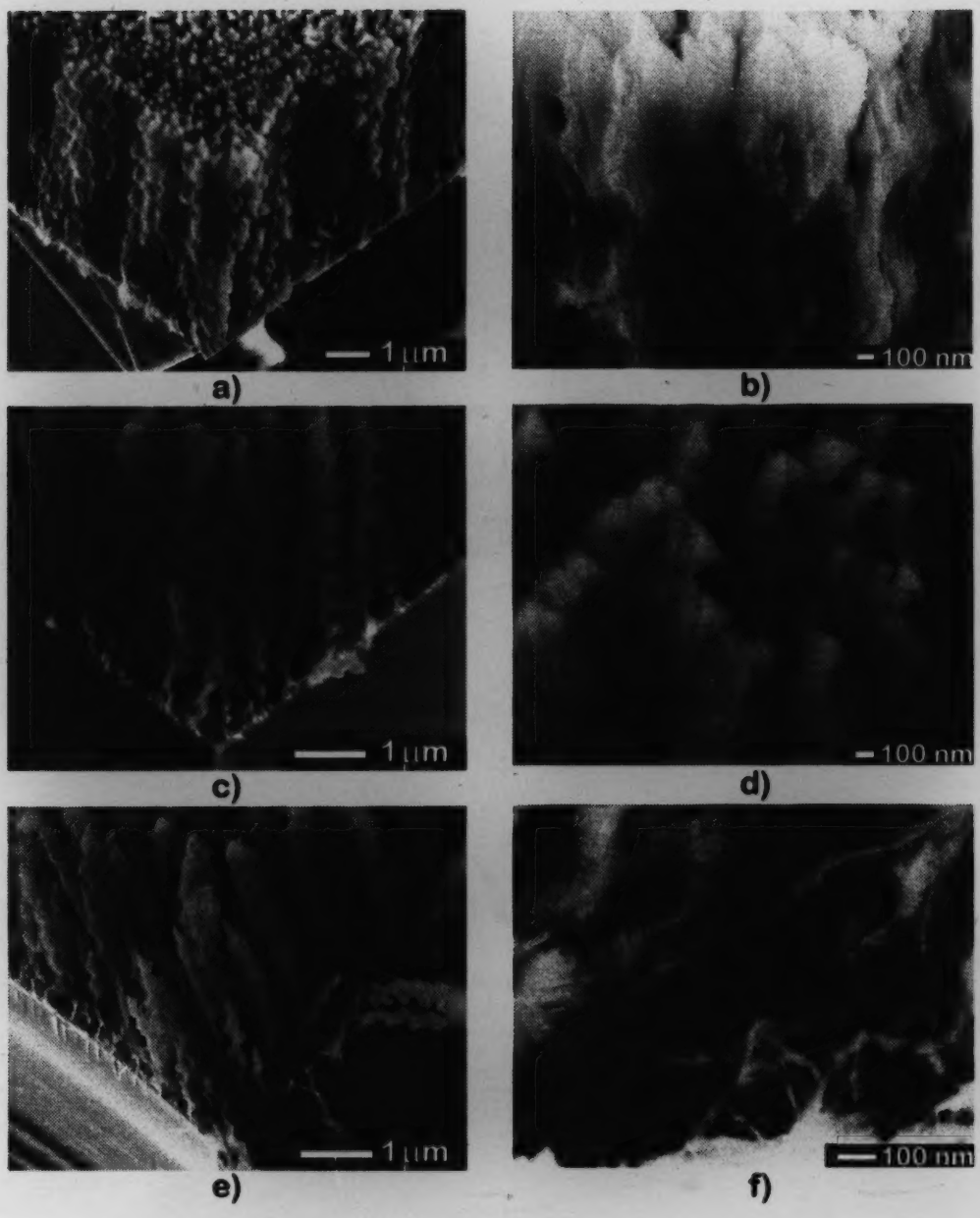

Figure 14: Three CaF_2 films deposited at $\alpha = 75°$, 85°, and 88°. The film shown in a) and b) was deposited with $\alpha = 75°$. The film shown in c) and d) was deposited with $\alpha = 85°$. The film shown in e) and f) was deposited with $\alpha = 88°$. Micrographs a), c), and e) are equal viewing orientations and magnifications as are b), d), and f).

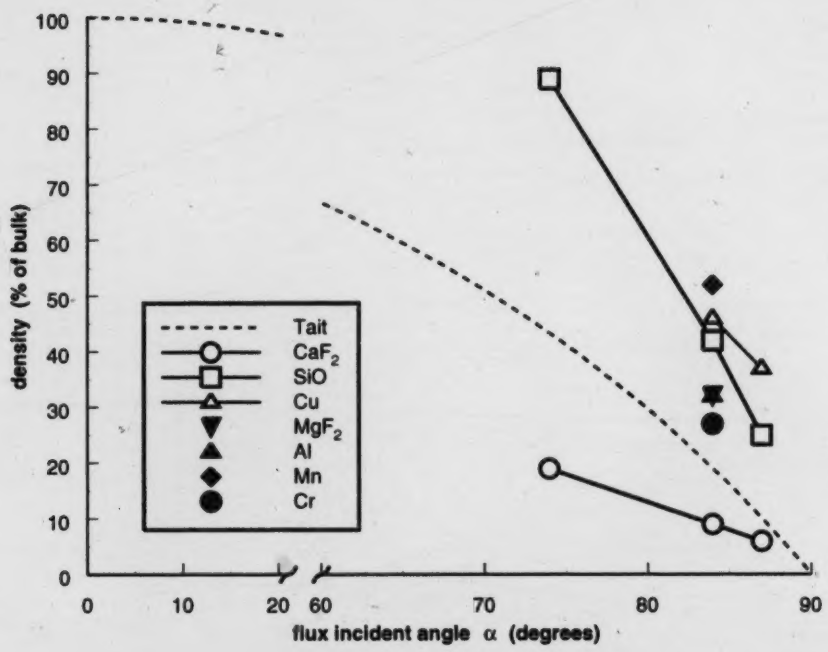

Figure 15: Graph of film density versus vapour incidence angle (α) for varied material. The rule from Tait [117] is shown as a dashed line. Note that the range $\alpha = 20°$ to $\alpha = 60°$ is omitted to allow more detail for large values of α.

combined with thickness measurements taken from SEM analysis, the density as a fraction of the bulk density was calculated. Figure 15 shows the results of these density measurements. Strong variation of density with α and with material is evident.

Together Figure 13, Figure 14, and Figure 15 demonstrate the strong dependence of film structure and properties on vapour incidence angle α when films are fabricated with oblique deposition. These figures also demonstrate the importance of the extreme oblique deposition regime where small variations in α (85° to 88°) can lead to dramatic changes in film structure. Finally, the importance of material on film structure is shown.

To increase the amount of control over film structure, α can also be varied during the deposition. This produces an inhomogeneity in the film structure perpendicular to the substrate plane. By varying α in a controlled manner, this structural variation can be exploited to produce useful effects. As will be discussed in "Interference Optics" on

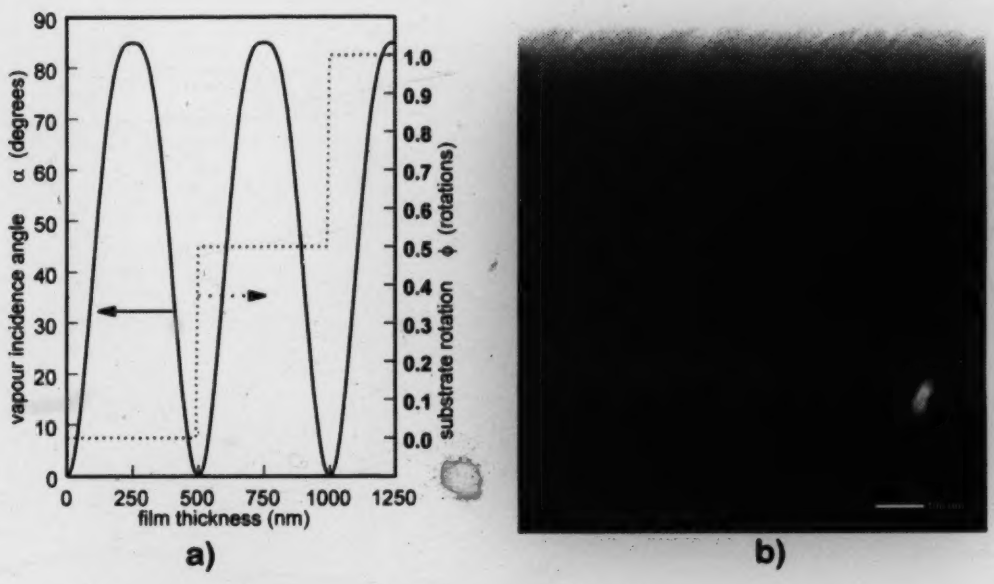

Figure 16: SiO film fabricated with sinusoidal variation of vapour incidence angle α. To mimic variation of α from +85° to -85°, the substrate was rotated (φ) 180° each time α reached 0°. This produces a structure similar to that obtained when α is varied from +85 to -85 with no rotation.

---

page 113, thin film interference filters can be fabricated by varying the film density, and hence the effective refractive index, in a controlled manner. This is accomplished by varying α between more and less oblique, repeatedly during the deposition. Figure 16 shows a SiO film deposited with this teehnique. The substrate azimuthal orientation φ was kept constant during deposition, and the polar orientation (or vapour incidence α) was varied sinusoidally between +85° and -85°. The porous columnar film regions were deposited with α large (+/- 85°), and the dense, uniform regions were deposited with α small (more normal vapour incidence). Because the substrate motion apparatus is restricted to α varying between 0° and 90°, a φ rotation of 180° was used each time α reached 0° (normal) to accomplish the desired motion. This is equivalent to varying α between +85° and -85°. This film again demonstrates the uniqueness of the extreme oblique deposition regime. For angles of α less than about 70°, the resulting film is dense, and uniform, while at extreme oblique angles, columnar structure results.

To further investigate variation with vapour incidence angle α, the film of

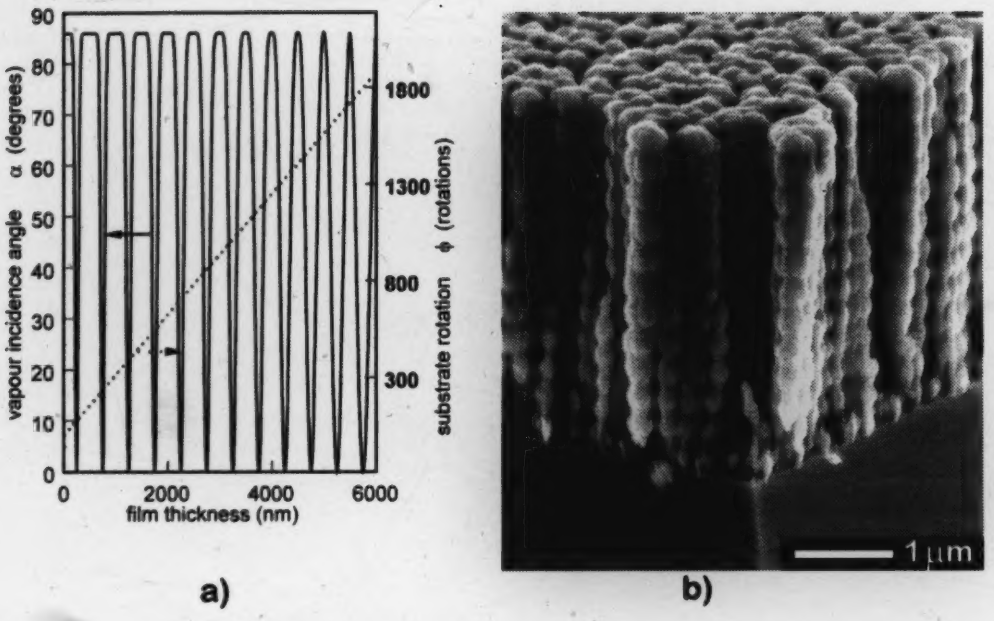

Figure 17: SiO film with quasi-sinusoidal variation of α during deposition, and rapid substrate rotation ϕ.

Figure 17b was deposited. Here, the following formula was used to control α:

$$\alpha = 86 - 86 \cdot \left| \sin\left(\left(t - \Omega \cdot floor\left(\frac{t}{\Omega}\right) \right) \cdot \frac{\Omega}{\pi} \right) \right|^{30 \cdot \exp\left(-\frac{t}{2000}\right)}, \qquad (4)$$

where t is the film thickness (nm), Ω is the pitch or period (nm), and the *floor()* function rounds down to the nearest integer. This varied α between normal (0°) and extremely oblique (86°) with a period of $\Omega = 500$ nm. The oscillation was quasi-sinusoidal, with the exponential term to which the sinusoid is raised creating a variation from one period to the next. At the beginning of the deposition (t small), most of the deposition time was spent with α oblique at 86°, with brief excursions to $\alpha = 0°$ and back. Toward the end of the deposition (t large), the exponential term becomes insignificant, and the α variation becomes a true sinusoid. This expression is graphed in Figure 17a for the film which is shown in Figure 17b. The substrate was rapidly rotated (ϕ rotation) during the entire deposition. The densification of the film is visibly dependent on the manner that α is varied.

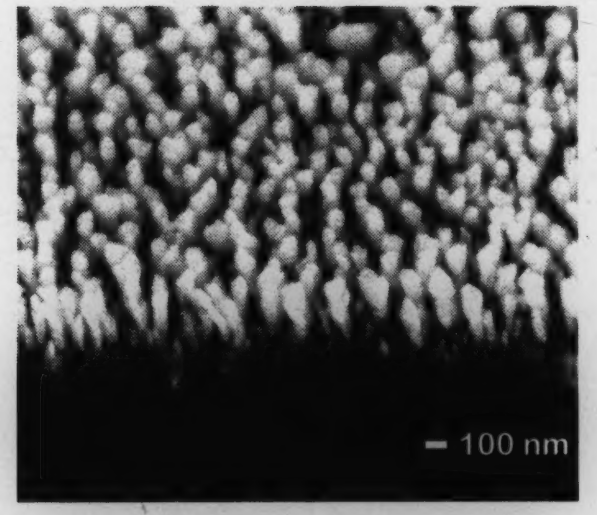

Figure 18: Cr film with porous 'post' structure atop a dense Cr layer [98].

In the lower portions of the film, the densified layers (where α was small) are minor bumps in the columnar structure whereas in the upper portions of the film, the densified layers (where α was small) dominate the structure. Unfortunately, substrate heating will also tend to increase column diameter, and may have played a role in this film structure. Substrate heating will be discussed in "adatom diffusion from heating" on page 40.

Variation of α during deposition can also be used to produce a dense film beneath a porous film. In Figure 18, a Cr film was deposited at normal incidence for the first portion of deposition. The vapour incidence angle was then changed to very oblique (86°) to produce a porous film. The substrate was rapidly rotated (ϕ rotation) during the entire deposition, resulting in a 'post' structure. Again, variation of α has allowed the porosity of the film to be tailored dynamically during deposition.

Finally, variation of α during deposition can be used to produce a dense region or 'cap' on top of the porous structured GLAD film. Figure 19b shows a SiO film, deposited in one deposition, where a dense cap of SiO was formed on top of a porous helical film. The variation of α and ϕ during the deposition is shown in the graph of Figure 19a. Capping was accomplished by an exponential decrease of α from 85° to normal while the substrate was rapidly rotated in ϕ. Capping of porous films with GLAD is a complex problem and is

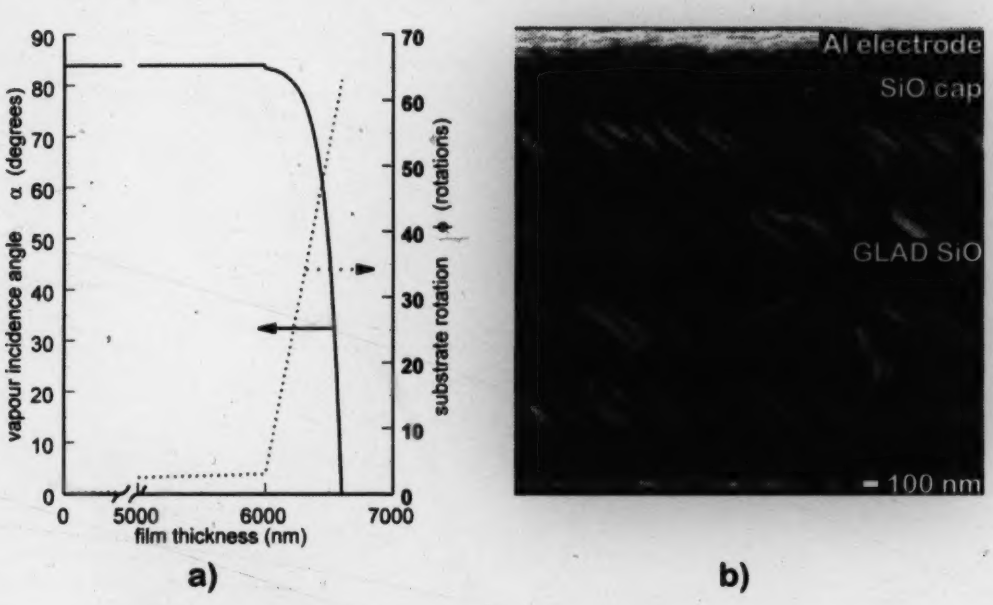

Figure 19: SiO with dense 'cap' atop a porous GLAD film. Al electrodes were deposited before and after the SiO film.

discussed in detail in "capping with GLAD" on page 55.

3.1c) variation of material

All observable thin film properties (density, stress, structure etc.) are dependent on film material. Because the dynamics of the physical processes that govern film growth depend on film material, variation of material will strongly affect the resulting film. As the intention of GLAD is to produce structure in thin films, the effect of material variation on structure was primarily studied in this thesis. As structured porous materials are desired with GLAD, adatom mobility is intentionally minimized by depositing films onto unheated substrates. There is a strong variation in adatom mobility with material, however, and this can significantly affect film structure. Figure 20 illustrates the effect of material on GLAD film structure. Roughly, adatom mobility scales with the ratio of the temperature of the film during deposition to the melting temperature of the bulk material (T/T_m - both in Kelvin). This ratio is the parameter used to specify the zones in the structure zone models (Figure 5). The adatom mobility determines the diameter of the columns of material that grow when the film is deposited at an oblique angle. Therefore, we expect that the diameter of the

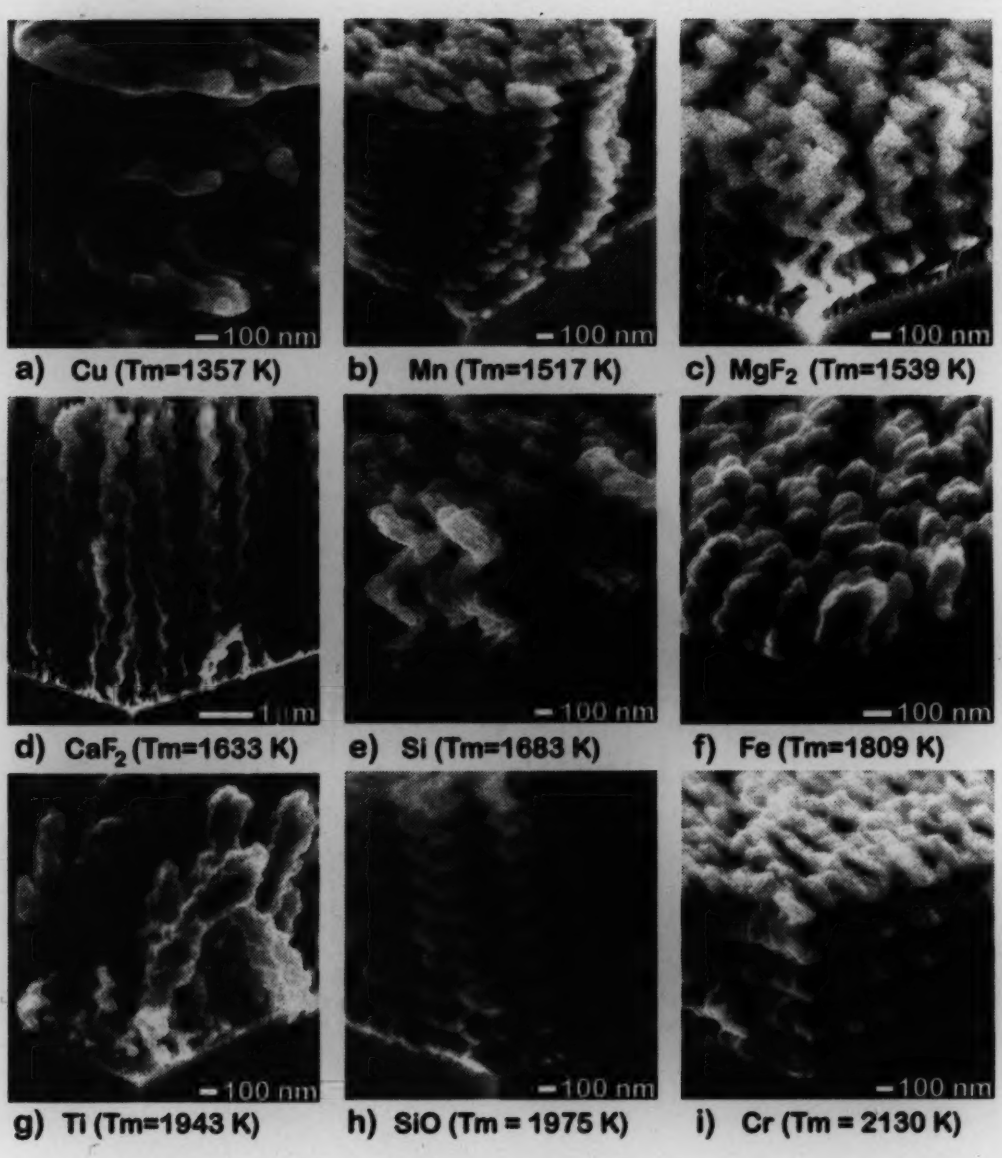

Figure 20: Variation with materials - a) Cu (T_m = 1357 K), b) Mn (T_m = 1517 K), c) MgF_2 (T_m = 1539 K), d) CaF_2 (T_m = 1633 K), e) Si (T_m = 1683 K), f) Fe (T_m = 1809 K), g) Ti (T_m = 1943 K), h) SiO (T_m = 1975 K), i) Cr (T_m = 2130 K).

---

columns of material observed in obliquely deposited films should scale with the bulk melting temperature of the deposited material, if the substrate temperature is kept relatively

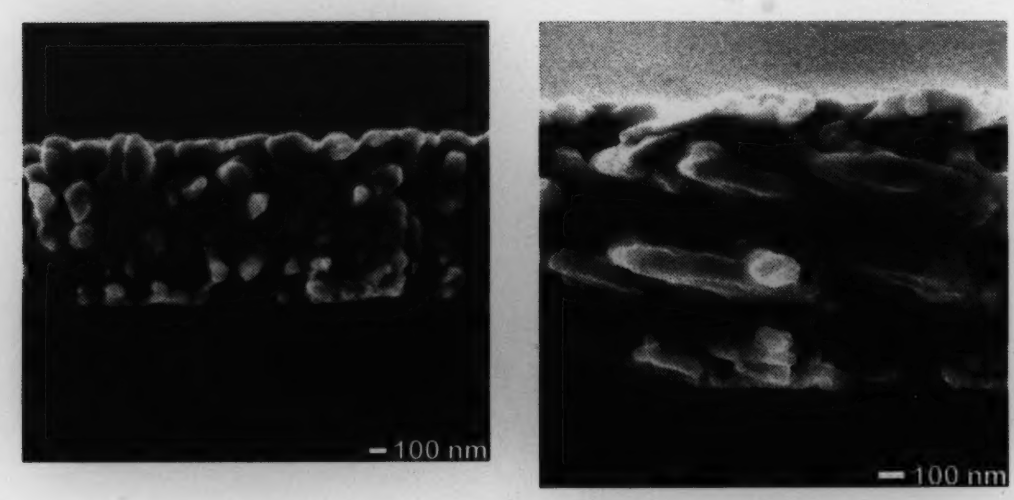

Figure 21: Cu films demonstrating the effect of fast substrate rotation on film structure. In a), the substrate was rapidly rotated, whereas in b), the substrate was slowly rotated.

constant. This is seen clearly in Figure 20 where the column diameter of the Cu film (T_m = 1357 K) is about 100 nm while the column diameter of the Cr film (T_m = 2130 K) is about 50 nm. The materials in the films of Figure 20a-i have monotonically increasing bulk melting temperature from Cu to Cr.

The intrinsic column diameter limits the scale of structural control in GLAD. It is impossible to fabricate structures with scale sizes smaller than the column diameter as adatom diffusion will 'erase' these structures. The two films shown in Figure 21 illustrate this effect. Both films are Cu deposited onto spinning substrates, with the intention of producing helical microstructures. In Figure 21a, the substrate was rapidly rotated to produce small pitch helices, but because the attempted pitch was less than the adatom diffusion length, the helical microstructure has been erased. Figure 21b was deposited onto a slowly rotating substrate, resulting in a helical structure that is larger than the adatom diffusion length. The helical microstructure in Figure 21b is obvious, with column diameters similar to the columns in Figure 21a (~100 nm). The effect of 'erasing' structure with adatom diffusion through rapid rotation of the substrate can be a useful effect. The

'post' structures of Figure 12f and Figure 18 were intentionally produced in this manner.

While adatom mobility variation with material has the most significant effect on film structure in GLAD films, other effects of varying material such as nucleation mechanics, crystallinity and facetted growth, renucleation, and surface roughening, contribute minor influences on film structure and properties.

3.1d) size scaling

It is important to know the upper and lower size limits on structures that can be fabricated with GLAD. The lower size limit is determined by the average adatom diffusion length as discussed above. Structures with dimensions smaller than the adatom diffusion length cannot be fabricated as the adatom diffusion will eliminate the shadowing effect which is central to the GLAD technique. A useful technique for examining size scaling in helical films is to compare the desired pitch of the helix to the observed column diameter. If the desired pitch is larger than the column diameter, a helical film will result. If, however, the desired pitch is smaller than the column diameter, a post structure results. This occurs because the observed column diameter results from the diffusion of adatoms on the surface of the growing film. As the desired pitch approaches the observed column diameter, adatom diffusion overcomes shadowing, and erases the helical structure, resulting in a vertical 'post' (Figure 12f).

Fortunately, adatom diffusion lengths on unheated substrates can be quite small for materials with high bulk melting temperatures (including refractory metals and most oxides and fluorides). MgF_2, CaF_2, ZrO_2, and Cr films, for example, exhibit column diameters of a few tens of nanometres. Figure 22a shows a MgF_2 helical film with a pitch of about 80 nm. It is difficult to discern if the column structure is a true helix, or somewhat of a helical ribbed shaft, however the film does demonstrate that some structural control below 100 nm is possible with GLAD. Figure 22b shows a MgF_2 film with a pitch of about 110 nm and a clearly shows the 'ribbed helical shaft' structure. Finally, Figure 22c and d) show MgF_2 films with a pitch of about 700 nm and a clear helical structure. Figure 23 displays size scaling in SiO films, and demonstrates that GLAD scales well to very large sized structures. Figure 23b is a film with a pitch of about 11 μm. With thick physical vapour deposition techniques, GLAD engineered films hundreds of μm thick could be produced, suggesting

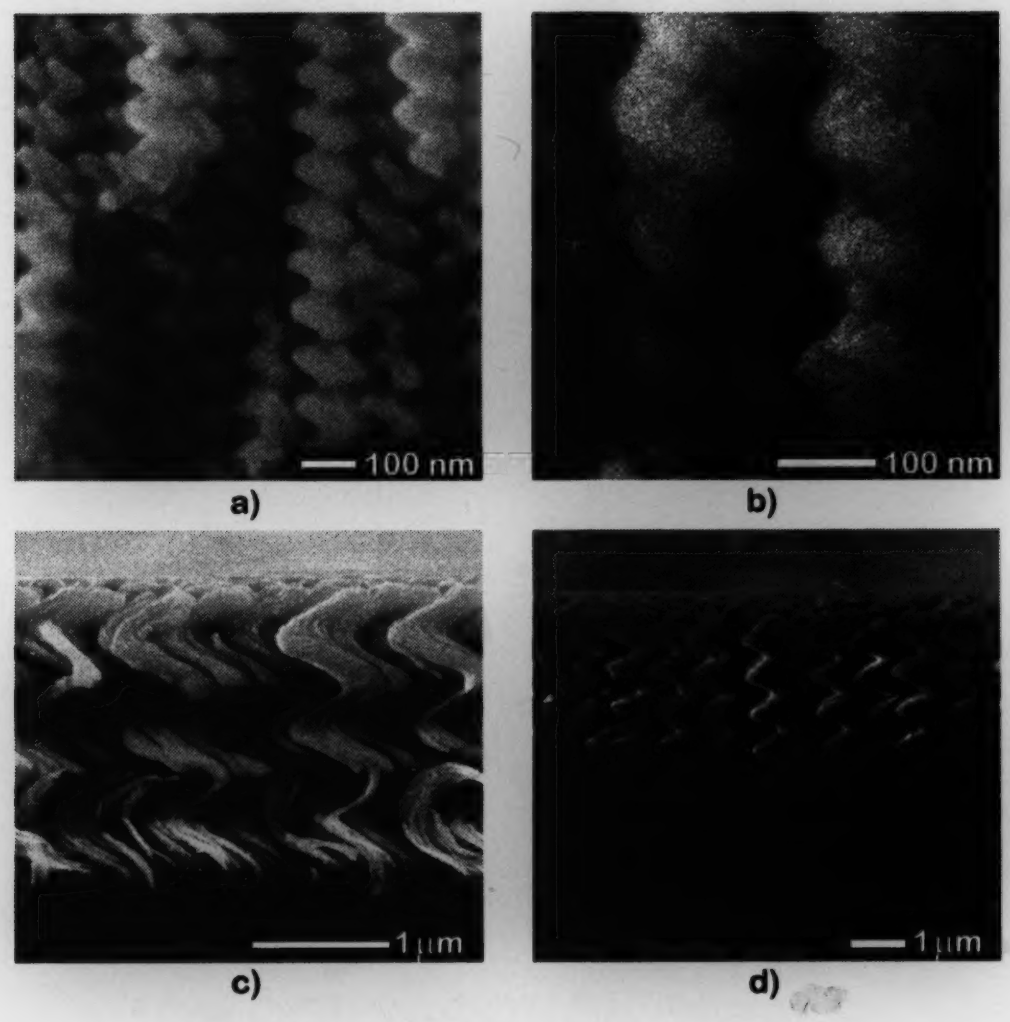

Figure 22: MgF_2 size scaling in helical structures from about 60 nm to about 650 nm. a) and b) were deposited onto a rapidly rotating substrate. c) and d) were deposited onto slowly rotating substrates.

possibilities for infrared and microwave applications.

Because of the fractal nature of thin film growth [79,8] and of the shadowing process in particular, zone 1 films exhibit scale invariant structure over a large range of scale sizes. In very thick zone 1 films, similar structure is observed from nanometer to millimeter scales. For constant rate rotating substrates, the resulting structure appears to be

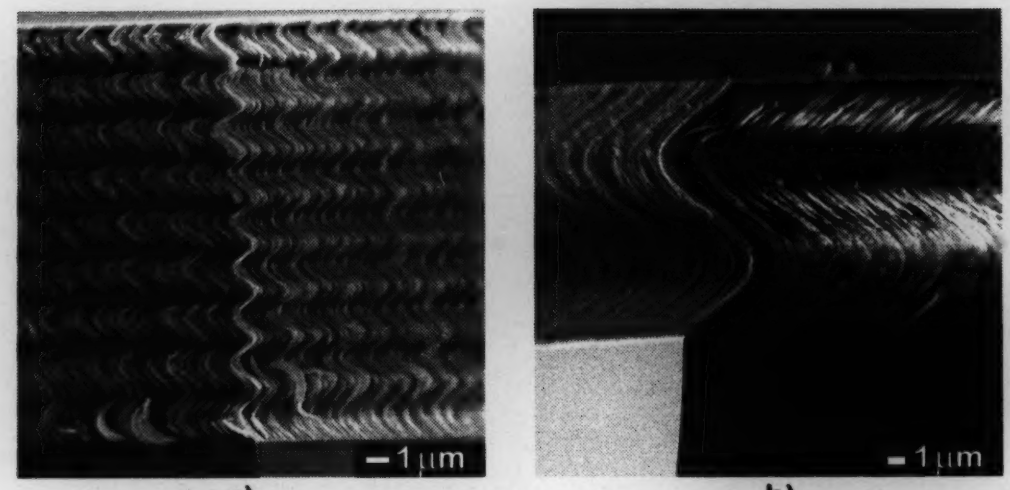

Figure 23: Size scaling in SiO helical structures from about 150 nm to about 13 μm. a) was deposited onto a rapidly rotating substrate, and b) was deposited onto a slowly rotating substrate.

helical for any rotation rate where the film thickness deposited during one rotation is substantially more than the average adatom diffusion length. Experiments indicate that there is really no upper limit on the size of structures produced with GLAD, other than practical deposition apparatus limits. The lower size limit appears to be bounded by the finite adatom mobility. As the structure size desired approaches the average adatom diffusion length, the structure becomes more and more blurred by the mobility of the adatoms. When attempting to make helical structured columns, the structure becomes a 'ribbed shaft' when the desired pitch is decreased to near the average adatom diffusion length. The structure exhibits circular posts when the desired pitch becomes less than the diffusion length.

3.1e) adatom diffusion from heating

While all films described in this thesis were deposited onto unheated substrates, heating effects are observed in many films. The resistively, or electron beam, heated vapour source, used in the film depositions, is a significant source of radiant heat. Temperatures comparable to the melting temperature of the source material are reached by the source material 'charge' and by the refractory metal foil boat (for resistive heating). Electron beam

evaporation produces substantially less radiant heating than resistive evaporation because of the elimination of the hot refractory metal boat. The heat radiated by either vapour source is absorbed by the vacuum chamber walls and fixturing, as well as the substrate and substrate holder. Also, as the vapour condenses on the substrate to form the solid film, the energy of the vapour, including the heat of condensation, is released, and contributes to substrate and film heating. The radiated heat energy absorbed by a unit area of the substrate tilted at α can be shown to be:

$$\frac{dQ}{dt} = \frac{\varepsilon_1 \varepsilon_2 \sigma T^4 A_s \cos\alpha}{4\pi r^2}, \tag{5}$$

where ε_1 and ε_2 are the emissivities of the source and film/substrate, σ is the Stefan-Boltzmann constant (5.67×10^{-8} W/m^2/K^4), T is the temperature of the vapour source (K), A_s is the area of the vapour source (m^2), and r is the separation between the source and substrate (m). Because of surface roughness, the emissivity of the film/substrate may be significantly different than that of the bulk material, and in the most porous of GLAD films might be high even for metal films. The characteristic sizes of the GLAD structure will affect the emissivity, and it might be possible to design a specific emissivity response as a function of radiation wavelength. Heat of condensation can be calculated from the vapour flux arrival rate and the heat of condensation of the film material. One interesting difference between heat arising from radiation, and heat from condensation is where the heat is deposited. The radiated heat is in the form of long wavelength infrared radiation which will, at least partially, penetrate the film/substrate/holder system. Heat of condensation, however, will be deposited only at the condensing surface of the film/vacuum interface. Limited thermal conductivity down the columnar film structure, particularly with GLAD where the columns are isolated, could lead to temperature differentials between the film surface and substrate. Also, in a vacuum environment, the thermal contact between the substrate and the substrate holder is typically very poor [73] resulting in limited conduction of thermal energy away from the substrate. Experimental difficulties, unfortunately, limit measurement of heating effects in thin film depositions. Thermocouples mounted on the back of a substrate are the most common techniques to measure substrate temperature for

preheated systems. With this technique, substrate temperature increases on the order of 100 °C have been observed, during deposition, for GLAD films, by J. P. Parks, but extrapolating this knowledge to quantitative discussion of film surface heating is not possible without a much more controlled experimental investigation.

Radiative and condensation heating raise the temperature of the substrate, and deposited film, and affect the film structure. In the description of film structure used in the structure zone models (Figure 5), the reduced temperature T/T_m is increased, and the structure moves away from zone 1 structure toward zone 2. Adatom mobility increases with heating and can begin to suppress the effects of atomic shadowing exploited by GLAD. The relationship between the many deposition parameters (substrate temperature, deposition rate, material, background gases) and the adatom mobility is complicated and difficult to discuss quantitatively. In a recent review of oblique deposition, Abelmann and Lodder [1] describe the many parameters affecting adatom diffusion length and develop an expression for average adatom diffusion length Λ as:

$$\Lambda = \sqrt{D \cdot \tau_m} \tag{6}$$

$$D = D_0 \cdot \exp\left(-\frac{E_h}{k \cdot T_f}\right), \tag{7}$$

where τ_m is the mobility lifetime (s), D_0 is the intrinsic diffusivity (m^2/s), T_f is the temperature of the film (K), and E_h is the energy required for site hopping by the adatoms (J). In an ideal material, the hopping energy, E_h, is about one fifth E_a, the activation energy for escape of an atom from the bulk material. Generally, materials with higher melting points will have large activation energies for site hopping, E_h, and will therefore exhibit shorter adatom diffusion lengths. This is seen in real films and is described in the structure zone models discussed in "adatom diffusion and shadowing" on page 11. In reality, E_h, τ_m, and even T_f will vary with the location of the adatom. Local geometry, chemistry, and temperature affect the observed adatom diffusion, complicating quantitative description of adatom diffusion effects. Other effects, such as high deposition rates limiting diffusion by 'burying' adatoms before they have a chance to diffuse, further complicate adatom diffusion characterization. The discussion of substrate/film heating and adatom mobility is

limited here, but the ongoing discussion can be found in the literature [1,2,121,122,129,60,120,79,34,73].

Figure 24 illustrates the effect of heating on the column thickness for a Cr film deposited at $\alpha = 86°$ onto a stationary substrate. The observed thickening of the column during growth is believed to be caused by increased adatom mobility due to heating of the film and substrate. GROFILMS (Grain Oriented Thin Film Microstructure Simulator) [32,33] is a line segment thin film microstructure simulator that was used to investigate this effect. When a constant adatom diffusion length was used in GROFILMS, the simulated film structure did not exhibit the column thickening observed in real films. Dr. D. Vick incorporated a dynamic adatom diffusion length into GROFILMS, and produced structures comparable to those observed in real films (Figure 24b and c) [125]. As GROFILMS is a two dimensional simulator, and cannot account for three-dimensional effects, it is possible that the column thickening effect is caused by a three-dimensional geometrical effect. But, as column thickening is observed in real films with one-sided, two-sided, and rotated depositions, heating is believed to be more likely the cause.

Other films exhibiting the effects of heating during deposition are shown in Figure 25. Figure 25a and b) show two views, at different magnifications, of an MgF_2 film exhibiting column broadening due to heating. Initially, column diameters are about 10-20 nm (Figure 25a). During the deposition, the column diameter increased significantly, until it reached about 100-300 nm at the top of the film (Figure 25b). To investigate the effect of heating, and to attempt to confirm that the column diameter increase was the result of film heating during deposition, Figure 25c and Figure 25d were deposited. Figure 25c demonstrates that column diameter doesn't increase indefinitely. If the observed column broadening was a scaling effect resulting from shadowing and the fractal nature of film growth, we would expect that the column diameters might continue to increase. If heating was the cause, we expect that the substrate will reach a temperature where it can radiate heat at the same rate it receives heat (limited thermal conductivity down the column however could lead to continual scaling). The temperature and the adatom mobility will then remain constant. As a final test, Figure 25d was deposited. It is a SiO film deposited in three steps. The ratio of the rotation rate to the deposition rate was kept constant

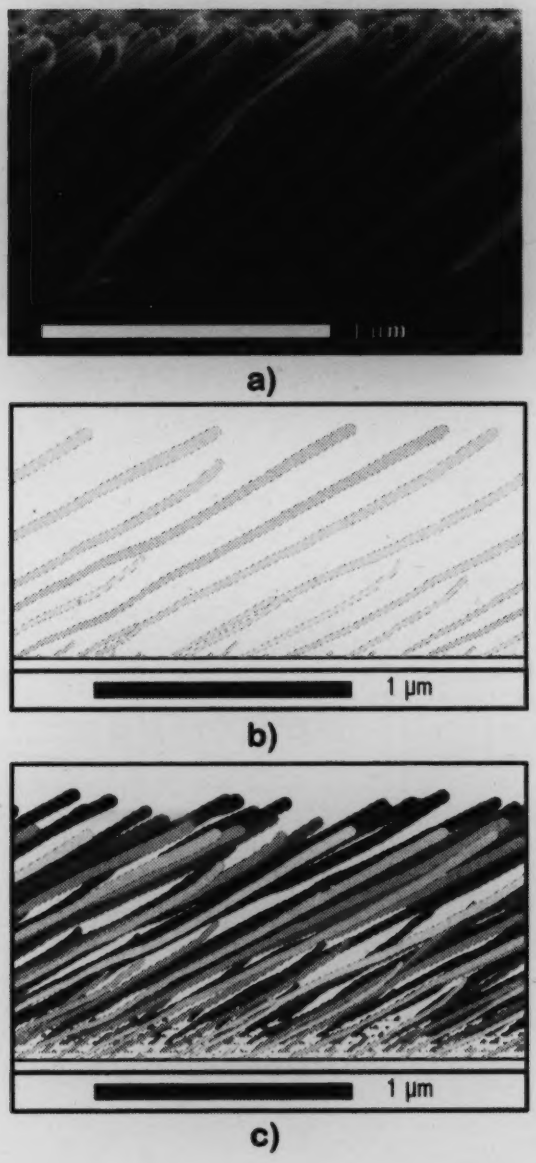

Figure 24: Film microstructure effects of heating. a) Cr film deposited at $\alpha = 86°$ onto a stationary unheated substrate. b) GROFILMS simulation [32,33] of a comparable oblique deposition with a dynamic diffusion length increasing from $\Lambda = 6.7$ nm at the substrate to $\Lambda = 20$ nm at the film surface. c) overlay plot of six such simulations to show the effect of three dimensional layering [125].

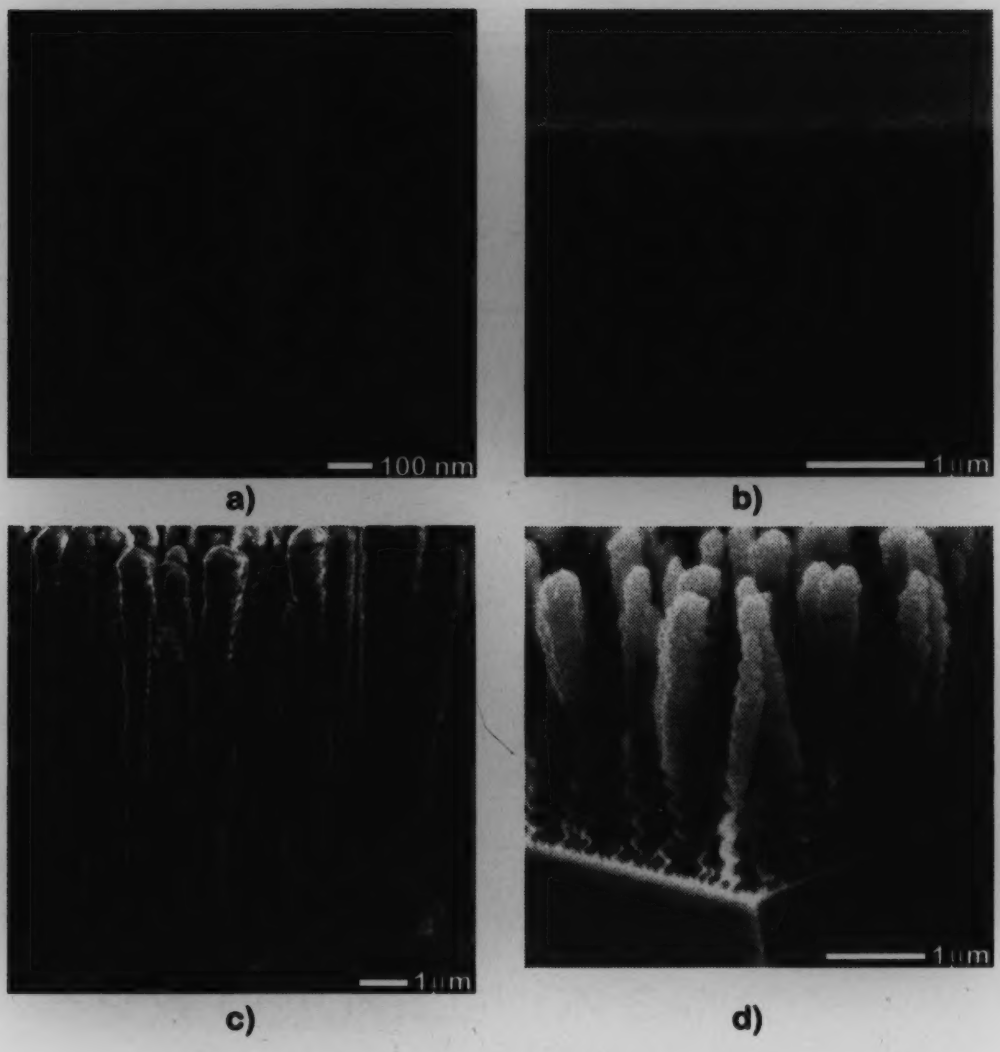

Figure 25: Films with microstructures that exhibit the effect of increasing adatom mobility due to heating during deposition. a) and b) show a MgF_2 film deposited at $\alpha = 85°$ with a deposition rate on the monitor of about 4 nm/s. c) shows a MgF_2 film deposited from a large source at $\alpha = 85°$ with a deposition rate on the monitor of about 8 nm/s. d) is a SiO film deposited at $\alpha = 88°$ in three stages with deposition rates of 0.5 nm/s, 8 nm/s, and 0.5 nm/s. The ratio of the rotation rate to the deposition rate was kept constant throughout c).

---

throughout the deposition, but the deposition rate was varied from slow (0.5 nm/s) to fast (8 nm/s) to slow again (0.5 nm/s). Deposition rates are as measured with the deposition rate

monitor placed close to the substrate and oriented facing the vapour source. The substrate was rotated five times in each of the three deposition periods with the pitch (thickness of film material deposited on the monitor during one rotation) kept constant throughout. Significant column broadening is apparent during the middle (fast deposition rate) section. After the deposition rate is reduced, the film slowly cools and the adatom mobility and column diameter decrease. This is shown in the re-emergence of the helical structure at the top of the film after the post structure observed during the fast deposition rate middle section.

To produce smaller scale structures with GLAD, and to produce thick films without adatom diffusion blurred structure, film heating must be understood and ultimately controlled. In this section, various heat sources (radiant, condensation) and sinks (radiated, conducted to substrate or substrate holder) are discussed. To control heating, the significance of these effects must be characterized and controlled. If radiated heat from the evaporation source is the dominant heat source, then shielding the substrate from the heated boat, or using electron beam heating should reduce heating effects. Alternatively, if heat of condensation is the dominant heat source, then reduced deposition rates will help. Heat removal from the substrate and film must also be investigated. If column broadening is occurring because of limited thermal conduction to the substrate holder, then better clamping or surface preparation techniques may reduce heating. Finally, radiation of heat from the film/substrate could be enhanced with placement of a cooled (possibly cryogenically) surface near the film/substrate. For this, because of the large tilt angle of the substrate, the geometry of GLAD is quite amenable. A flat cooled surface could be placed parallel to, and quite near to, the substrate without blocking the evaporant vapour flux.

3.1f) transmission electron microscopy

Transmission electron microscopy (TEM) is an analytical tool that allows a different observation of film structure than that obtainable with scanning electron microscopy. Atomic resolution is obtainable with TEM in some cases. Also, TEM allows 'dark-field' imaging of electron diffraction patterns, which provide information about the crystallinity of the sample. TEM analysis typically requires samples to be less than about 100 nm thick, making it difficult to analyze most GLAD films with an electron beam

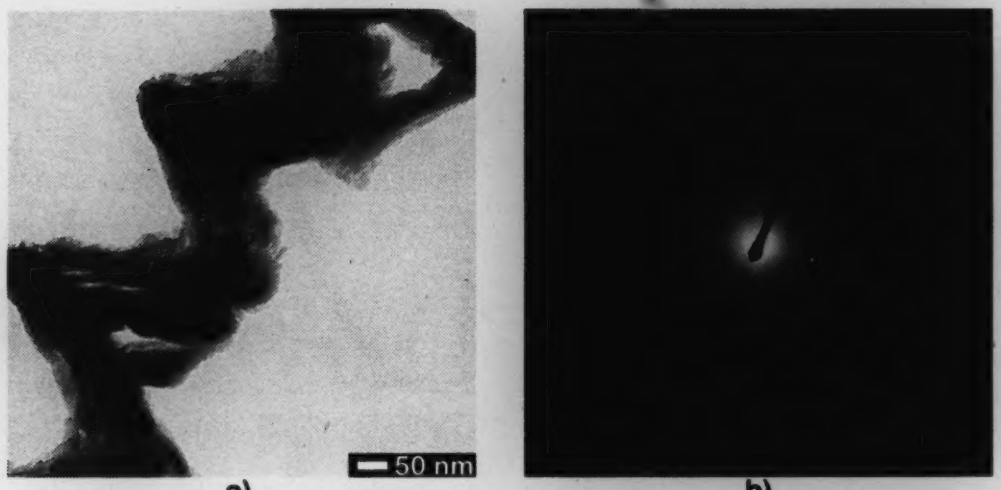

Figure 26: TEM image and electron diffraction pattern of a Si GLAD film. Diffuse rings in the diffraction pattern (b) show that the Si film is amorphous.

incident perpendicular to the substrate surface. One technique that may allow TEM analysis of a GLAD film in cross section would be to fill the pores of the film structure with a polymer or resin, then thin the sample to the required thickness by mechanical polishing and/or ion milling. Initial analysis, however, was performed by mechanically scraping (with tweezers), a small quantity of GLAD film material off of the substrate and onto a carbon coated TEM grid sample holder. The material was then sandwiched between two grids and imaged. While the bulk GLAD film structure was destroyed with this technique, it appears, from the TEM images obtained, that columns of material remained intact and were observable. I would like to thank Dr. K. L. Westra for suggesting the idea of scraping the film material onto a TEM grid, and M. Malek and Dr. R. Egerton for helping with the TEM analysis.

A TEM image of a single column of a Si helical GLAD film is shown in Figure 26a with the corresponding electron diffraction image in Figure 26b. The image of the film column shows that the column seen in SEM analysis is not solid, but is instead composed of many levels of filamentary structure down to the resolution of the image. The column is composed of smaller filaments, which are in turn composed of even smaller filaments. This

is in accordance with observations and discussions of the fractal nature of thin film growth [8,120] and with the evolutionary structure zone model described by Messier [81,79]. It appears from this analysis that the adatom mobility discussed previously may correspond to the smallest scale sizes, and that the enlargement of columns results from a scaling at all levels of growth, resulting from increased size of the smallest 'grains'. Terminology is difficult in this area as 'grain' and 'column' are used somewhat interchangeably in the literature. 'Grain' should be used to describe the smallest sized structures, frequently single crystal, resulting from the actual average adatom diffusion length. 'Column' should describe a collection of grains with a wide-ranging scale size. An atomic force microscopy study [129] gives good experimental observations of the scaling properties of film growth with varying material and adatom mobility.

The crystalline texture of evaporated thin films is affected by deposition parameters such as substrate temperature, surface chemistry, and vapour flux energetics. Some of the first investigations of oblique incidence deposition were based on crystallinity variation induced by oblique deposition [127]. Unfortunately, initial investigations with x-ray diffraction by M. Seto, and with electron diffraction, shown here, were unable to detect significant crystallinity orientational effects induced by GLAD. The diffuse rings in the electron diffraction pattern of the Si film shown in Figure 26b indicate that the crystal texture of the Si is amorphous, as is typical of Si evaporated onto unheated substrates. The temperature of the substrate is insufficient for Si adatoms to overcome the energy barrier for the formation of crystalline Si. The CaF_2 film shown in Figure 27 appears to be composed of small (~15 nm diameter x 40 nm long) single crystal grains. The image and diffraction pattern shown in a) and b) are at low-resolution, showing a large number of crystallites and the corresponding rings in the diffraction pattern. In c) and d), a higher resolution is used and the diffraction spots of individual crystals are observed in the diffraction pattern. Unfortunately, the diffraction patterns (b and d) were somewhat overexposed, limiting their usefulness for quantitative analysis. The CaF_2 film shown in the TEM images of Figure 27 is the same film shown in the SEM images of Figure 14c and d). Close examination of the SEM image reveals small 'fingers' that are the single crystallites seen in the TEM images, and a fuzzy column structure that results from the high porosity

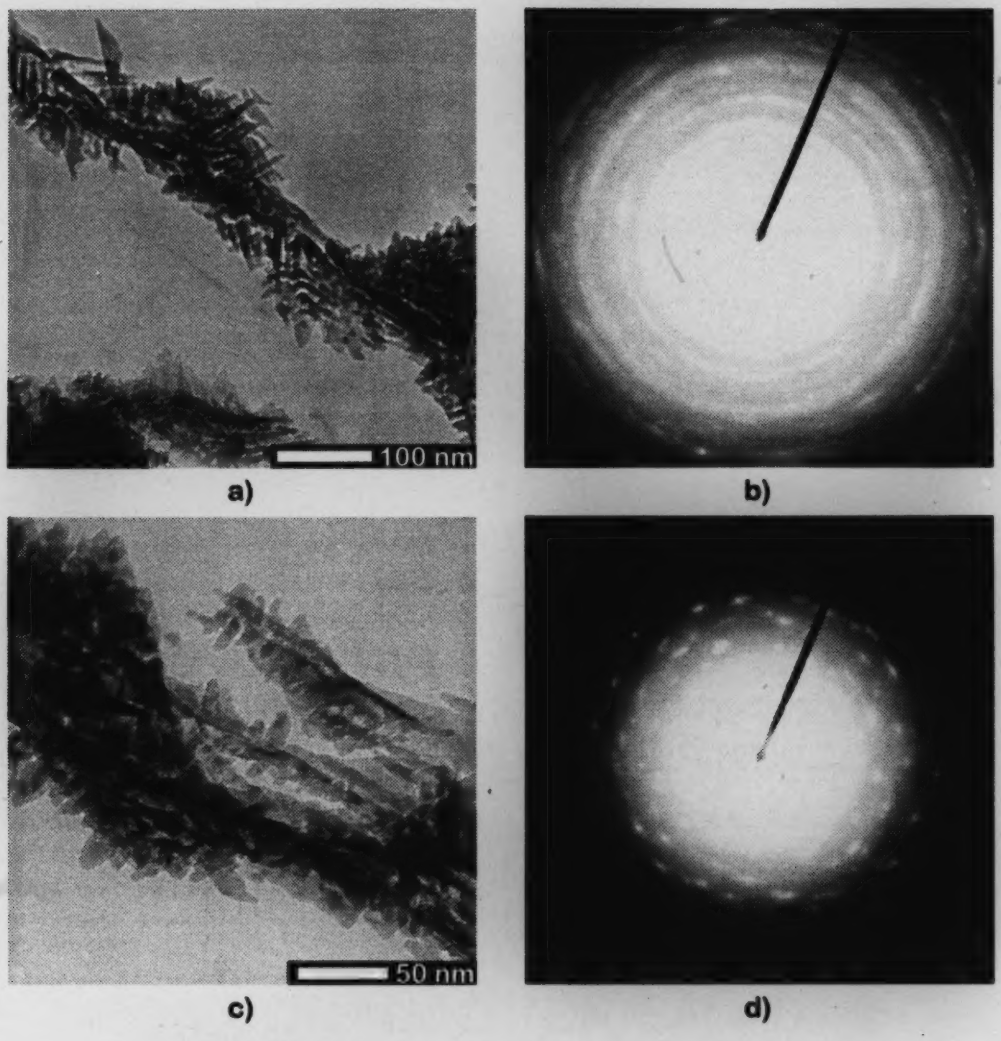

Figure 27: CaF_2 TEM images (a and c) and electron diffraction patterns (b and d). The film appears to be composed of small (~15 nm) diameter single crystals. Diffraction patterns b) and d) were obtained from a small portion (~20 %) of the area of the images a) and c) respectively.

of the individual columns.

3.2 Equipment Development

During development and investigation of the GLAD process, the deposition equipment progressed through multiple stages. The first deposition apparatus was very

simple, allowing the polar angle (vapour incidence angle α) to be set to a fixed value for each deposition run. Substrate rotation (ϕ rotation) was controlled manually without feedback from the deposition rate and was restricted to a limited range of rotation rates. Later improvements included: 1) design of a substrate holder with two axis of rotation (α and ϕ), both dynamically controllable during deposition; 2) incorporation of feedback from the deposition rate monitor to allow accurate control of structure independent of fluctuating deposition rate; and 3) design of a LabVIEW based software control system to allow description and use of complex substrate motions. This section describes the stages of equipment development and the current GLAD apparatus. I also suggest improvements for future GLAD system design.

3.2a) fixed polar angle

In its most basic form, an apparatus to perform GLAD would allow rotation of a substrate while the vapour incidence (α) was kept fixed at a large oblique value. A large range of simple structures, such as posts and helices, can be produced with this setup, and even some complex structures, such as those described as advanced techniques [96] (See "Advanced Techniques for Structural Control" on page 67.), are possible with fixed vapour incidence. The one requirement needed to produce complex structures with fixed α is some form of feedback control of the deposition rate. The fluctuation in deposition rate, which is common in most thermal or electron beam evaporation systems, would require that feedback be used to produce structures with accuracy and small scale control.

Two approaches for feedback control are possible. In the first, feedback control of the evaporation power source is used to produce a constant deposition rate. Many deposition systems allow the power delivered to the evaporation source to be controlled with feedback from a crystal oscillator deposition monitor to achieve a constant deposition rate on the monitor. With a constant deposition rate, film deposition becomes constant in time, and the desired motion can then be described as a function of time. The rotation or stepwise motion of the substrate can then be controlled with a simple control system where the motion is dependent on time only. The second alternative is to use feedback from the crystal monitor, in a more elaborate control system, to vary the substrate motion relative to the time-varying deposition rate. The power to the evaporation source is controlled

manually to produce a deposition rate near a desired value. The deposition rate can then drift in time. This approach has the primary disadvantage that variation in the deposition rate induces more variation in the deposition process than a simple increase in arrival rate of the vapour flux. Substrate heating, background contamination, and other processes vary with deposition rate, and therefore can vary during deposition with this control technique. This was, however, the control technique used in the work described in this thesis due to the the lack of available equipment to maintain a constant deposition rate. I believe that the method of using feedback to control the power delivered to the evaporation source, and produce a constant deposition rate, should be the preferred method of rate control with GLAD.

In the apparatus used for the research described in this thesis, the deposition rate was read from an analog output on the rate monitor with an analog to digital measurement input of a PC-LPM-16 Multifunction I/O card (National Instruments Corp.) in a Pentium based computer system. A LabVIEW (National Instruments Corp.) based control system was used to adjust the step rates of the motors controlling the substrate orientation, based on a mathematical description of the desired substrate position as a function of the deposited film thickness. Feedback of the deposition rate allowed adjustment of the substrate motion to account for varying deposition rate. The front panel of the LabVIEW control software is shown in Figure 29. A fictitious, but representative, fluctuating deposition rate is shown in the chart recorder box. Film structure and deposition parameters are set before deposition, the evaporation source is heated, and then the software begins control of the motors and fabricates the desired structure.

3.2b) variation of polar angle

To produce structures where the density and/or column spacing vary as a function of deposited film thickness, a substrate motion apparatus is required that allows variation of the flux incidence angle α during deposition. Deposition rate varies as a cosine of the polar angle (not α) between the source normal and the substrate location in the vacuum chamber, requiring minimization of substrate displacement within the vacuum system to achieve constant deposition rates with motion. This cosine dependence should not be confused with the second cosine dependence of rate arising from the tilt (α) of the substrate.

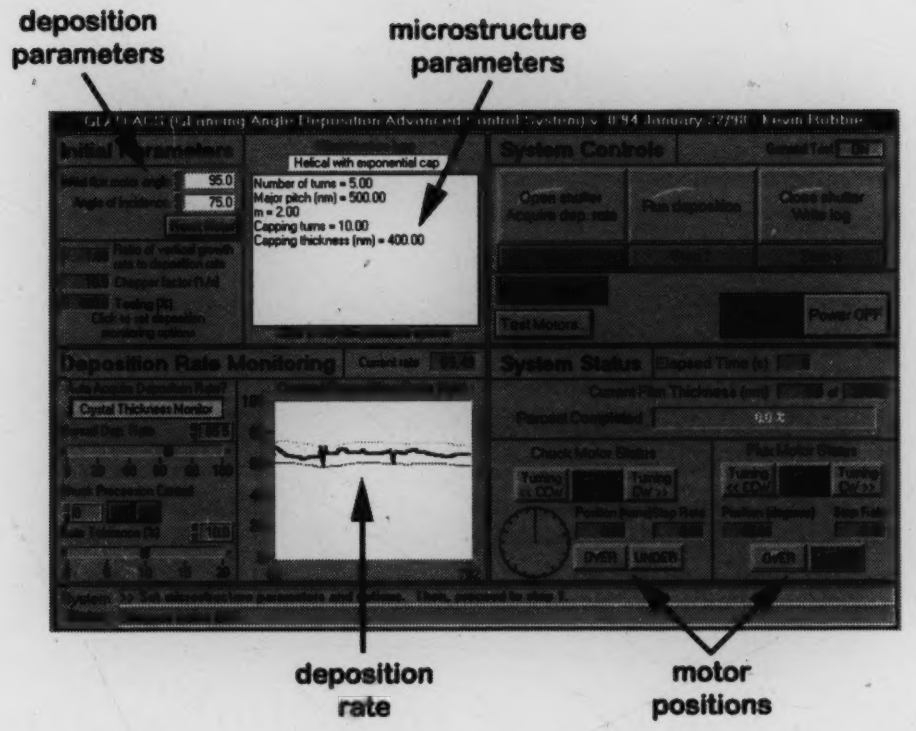

Figure 29: Front panel of LabVIEW control system for GLAD. A typical fluctuating deposition rate is shown in the deposition rate chart recorder box 'deposition rate'.

To minimize the effect of deposition rate varying with substrate motion, the substrate holder was designed to allow substrate tilt (vapour incidence angle α) with the axis of rotation passing through the film surface. This way the substrate tilts without any 'swing', and the only variation in deposition flux arises from the tilt angle.

Also, as described previously (See "Oblique Deposition" on page 15.) film structure depends critically on vapour incidence angle. At very large vapour incidence angle ($\alpha > 75°$), very small changes in α can lead to significant changes in film structure (See "extreme oblique deposition" on page 20.). To address this problem, a stepper motor with a 10:1 gearbox was used to achieve absolute control of α to less than 0.2°. For extremely fine control of density, even finer resolution may be required. However, with the

deposition apparatus used here, the finite size of the evaporation source resulted in vapour arrival angle spreads of ~5° limiting the usefulness of more precise control of α. If finer control is required, not only must α be more accurately controlled, the angular spread of the vapour source must also be reduced.

3.2c) techniques for stepper control

There are a number of techniques which can be used to control the motion of the stepper motors that set the position of the substrate during deposition with GLAD. Initially, a system was employed where the software control system sent pulses directly for each step required. This, unfortunately, requires high speed computation for complex motion descriptions and, therefore limits its usefulness. The power and utility of LabVIEW to allow simple description of the many structures desired for fabrication was considered valuable enough to warrant attempting other approaches. LabVIEW, running on an Intel 486 processer, available at the time, was too slow to allow single step control, so a system employing counters generating pulse trains was used. The software in LabVIEW was designed to determine step rates for the motors, and control free-running pulse generators, which stepped the motors. The pulse generators could then run (and step the motors) while the software was computing the required step rates for the next stage of the deposition. After the computation cycle (typically 100-500 ms), the software calculates the number of steps taken by the steppers from the known step rate and the elapsed time. This technique was very successful, allowing a much wider range of step rates than was previously possible (with single step control), and allowed fabrication of the advanced structures discussed later (See "Advanced Techniques for Structural Control" on page 67.) as well as many of the more complex films described throughout this thesis. Unfortunately, this technique has a significant flaw. Because of the imprecision of the clock available to LabVIEW from the Windows operating system (55 ms), the calculation of the number of steps taken by the steppers (from the known step rate and the elapsed time) is frequently wrong by a step. These step errors accumulate, leading to a precession effect. The software loses track of exactly what the substrate position is, and is unable to accurately fabricate some complex structures. More advanced structural control techniques, where the substrate must return to a specific position multiple times (100s in some instances), are particularly

difficult, and can be impossible because of this problem.

There are many possible solutions to the precession problem including: 1) using additional counters to actually count the number of pulses sent to the stepper driver electronics; 2) position encoders mounted on the steppers to read absolute position; 3) some form of single step motion control; and 4) an external clock with microsecond timing accuracy that can be read by the software to allow accurate calculation of steps performed. Newer versions of LabVIEW also address this problem with increasingly precise internal clocks.

3.2d) techniques for structure description

In the LabVIEW software which is the currently used GLAD control system, film structures are described with a plug-in software module where the position of the two motors is described as a function of film thickness deposited on the crystal thickness monitor. This approach allows simple creation of new structures while keeping the large majority of the software unchanged. However, one must be careful to describe motion regiments that the stepper motors are capable of performing. Abrupt jumps in substrate position or rapid accelerations in rotation rate are difficult for most steppers, and should be avoided. The current software checks for accelerations that are too rapid, or step rates that are too high, and limits both, while displaying an error message. When there is more time, the motor catches up to the desired position, but with some loss of accuracy in the described structure. A possible future improvement in the control software would be to allow the user to describe the columnar structure of the film as some mathematical function of form desired, instead of having to describe the motion of the substrate. The structural description would then be translated to create the motion algorithm necessary to fabricate the structure. The 'director' based approach described in [71,72] for optical properties would be a good starting point for this type of structural description.

3.3 Capping

For many applications of GLAD, a dense 'lid' or 'cap' is required. A cap allows the construction of a functional structure, for example, the deposition of electrodes for application of electric fields across the film structure. This could conceivably be used to

'squeeze' the spring structure to create transducers for acoustic applications, such as medical imaging (See "Squeezing" on page 120.). Unfortunately, fabrication of a dense cap atop a porous GLAD film can be difficult in some cases. The non-equilibrium nature of the film condensation process produces stress in the film which can lead to cracks and delamination [75]. Heating during deposition can also lead to structures which are difficult to cap. In this section, various techniques for capping of porous GLAD films are discussed, as well as difficulties and successes in film capping.

3.3a) capping with GLAD

Probably the best technique for producing a dense cap atop a GLAD film is to use GLAD substrate motion techniques to evolve the film structure to a dense layer. Care must be taken to avoid 'filling in' the pores in the porous film. In Figure 19 (page 35), a SiO film with a dense cap atop a 3-turn porous, helical, GLAD film is shown. The film was produced with a typical GLAD rotation of ϕ (to produce a helix) during the first portion, while keeping α constant at 84°. The cap was then fabricated by decreasing α to 0 while rapidly rotating the substrate (ϕ). This technique resulted in a dense, uniform cap which allowed the deposition of the top Al electrode seen in the figure. Variation of α toward normal densified the film structure, as discussed in "variation of vapour incidence angle" on page 27. SiO is a fairly simple material to cap with GLAD because it has an abrupt transition from a columnar structure to a dense structure as α is decreased below about 70°. Also, it doesn't build up excessive stress when deposited as a dense film. For MgF_2, however, neither of these mechanisms occur, making MgF_2 much more difficult to cap with GLAD. MgF_2 has strong intrinsic tensile stress when deposited by evaporation, resulting in fracturing of films when thicknesses of ~1 μm are fabricated in normally deposited films. The porous nature of GLAD films allows this stress to be relieved while the film is porous, but when a cap is desired, it can have significant effects. The exponential decrease in α used in capping the SiO film of Figure 19 was chosen because, in a study of MgF_2 capping, it was found to produce the best caps. Figure 30 shows two similar MgF_2 films capped with linear (a,b,c) and exponential (d,e,f) decrease in α. Substrate rotation (ϕ) was rapid for both capping examples. In the example with linear capping (a,b,c), densification of the capping layer has resulted in buildup of excessive tensile stress, resulting in fracturing of the

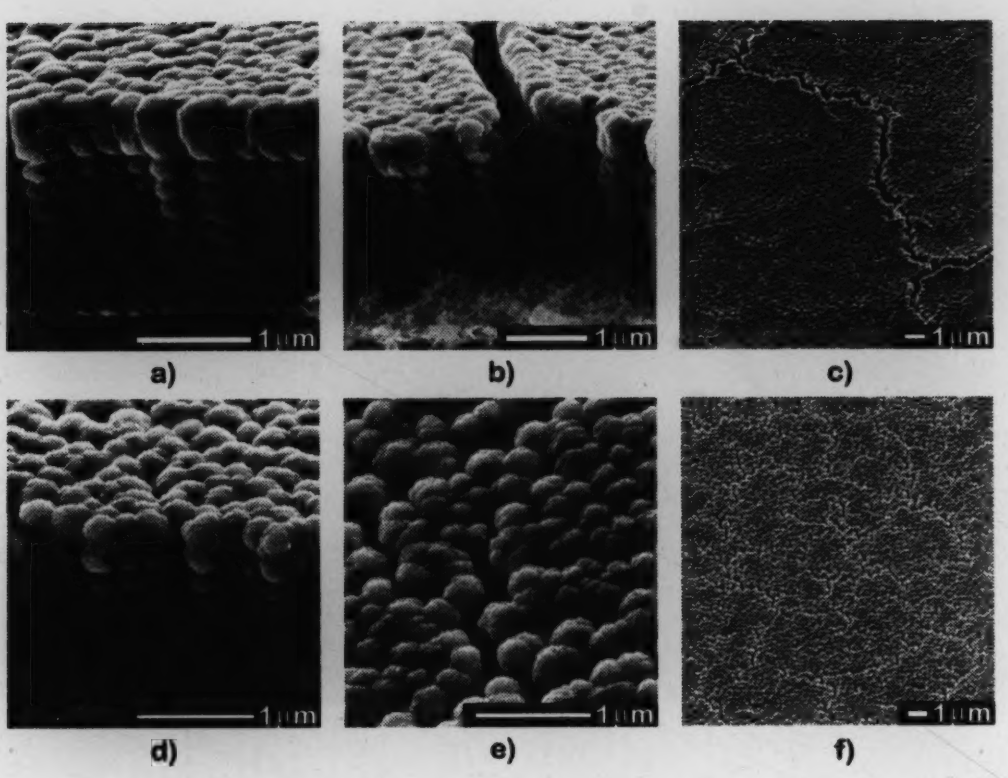

Figure 30: MgF_2 capping with linear decrease in α (a,b,c), and exponential decrease in α (d,e,f).

capping layer and formation of sizeable voids, which would be deleterious in most applications. When the helical MgF_2 film is capped with an exponential decrease in α, similar to the capping used for the SiO film of Figure 19, a fairly dense cap is produced, with only minor cracking (Figure 30d,e,f). This would be an acceptable cap for most applications as a metal deposited with normal deposition onto this cap could easily bridge the cracks and produce an acceptable electrode. Choice of the 'time constant' in the exponential function, used for the description of the variation of α, allows this capping process to be optimized.

3.3b) failure mechanisms

Failure of capping of a porous film due to tensile stress was discussed above in a case where minor stress had opened voids in the cap structure. In the extreme, tensile stress can lead to strong delamination of the film as is shown in Figure 31a. Here, an early attempt

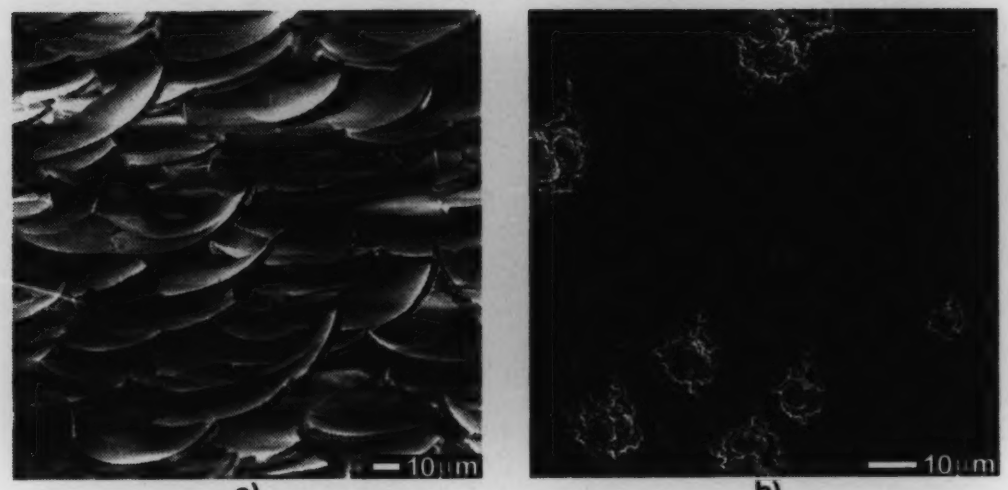

Figure 31: Failure mechanisms in capped GLAD films. a) nodule growth due to insufficiently clean substrates, and b) delamination of the film due to tensile intrinsic stress.

at film capping resulted in a very thick, dense layer, with strong tensile stress atop a porous GLAD film. The tensile stress was sufficient to fracture the film, resulting in dished film fragments. Interestingly, heating and charge buildup caused by the scanning electron microscope was sufficient to induce further fracturing, allowing direct observation of film cracking in real time. In Figure 31b, an additional capping failure mechanism is shown. We hypothesize that small dust particles on the substrate have led to the formation of 'nodules'. This is commonly seen in thin film growth [14], where substrate irregularities or preferential nucleation sites lead to a source of shadowing. The nodule propagates through the film structure, and creates a dome topped irregularity in the film. In GLAD, extreme shadowing accentuates this effect, resulting in significant defects on insufficiently clean substrates. With clean substrates, nodule formation was not observed, and very large areas were seen to be defect free. When capping a film with nodules, large holes occur near the nodules, resulting in a failed cap. This is not seen as a significant problem, as careful cleaning of substrates eliminates the nodules. It may, however, require that production use of GLAD be limited to a clean environment. None of the work discussed in this thesis was performed in a particulate-controlled environment (cleanroom) although some care was

taken to keep substrates particulate-free before deposition.

3.3c) alternate techniques

Densification of the deposited film with GLAD is not the only technique that can be used to cap porous GLAD films. Many techniques could be used, including chemical vapour deposition, chemical plating, sputtering, and ion-beam assisted deposition. To cap a porous GLAD film, a process is required that produces a dense layer atop the film without filling in the pores. Figure 32 shows the results of CVD capping of a SiO film. The film in a) is a large-pitch SiO film deposited with $\alpha = 86°$ resulting in a very porous structure. Capping with GLAD was attempted, but the high porosity and large pores, resulting from the highly oblique vapour incidence and substrate heating, have prevented the cap from forming. Capping of the film was then attempted with chemical vapour deposition (CVD) of SiO_2 (b and c), and SiN (d). The SiO_2 cap is quite dense (as seen from the top view - c), while the porous structure has not been filled (as seen from the cross-section - b). SiN capping by CVD was not as successful, resulting in a rough top surface without sufficient densification (top view - d). Differences in deposition mechanics between SiN and SiO_2 CVD may explain these differences, but a more detailed examination is required to eliminate experimental variation. The SiO_2 capped film, however, demonstrates that CVD capping techniques appear promising for capping of porous GLAD films.

3.4 Applications

Application of GLAD to a number of technological fields appears promising. The ability to engineer the structure of a material on the nanometer scale with the control possible with GLAD is unique, and suggests that the uses for GLAD may be broad and significant. In this section, I briefly describe a number of areas of possible application of GLAD, and in some cases, describe initial work that I have performed to investigate feasibility of these ideas. Availability of testing facilities have limited the number and depth of the investigations. I will present numerous application ideas and discuss the background for each. This section is by no means a comprehensive coverage of possible applications of GLAD. Many more ideas are currently under investigation.

3.4a) thermal barriers

Thin film thermal barrier coatings, on components of gas turbine engines, for

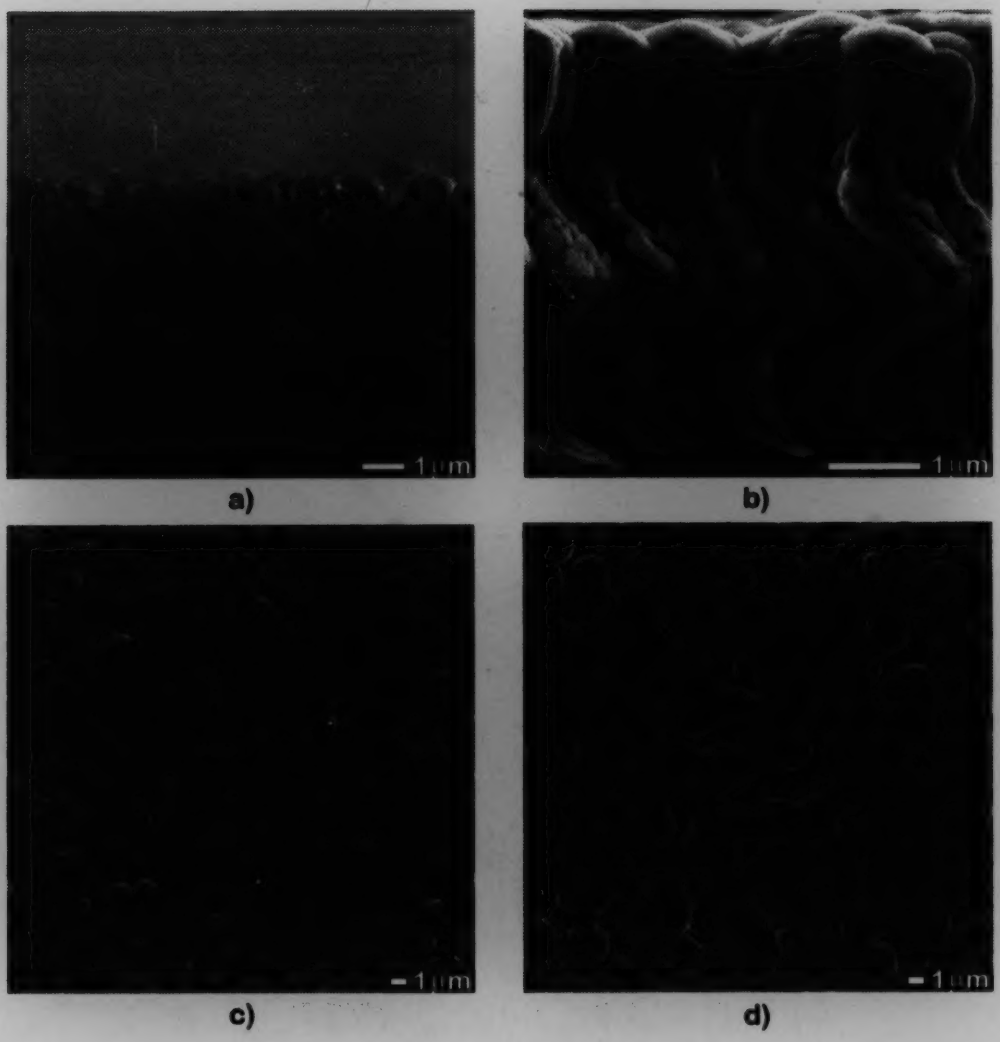

Figure 32: Alternate techniques for capping GLAD films. a) an essentially uncapped SiO film with large voids. b,c) cross-section and top view of the film in a) coated with SiO_2 by CVD. d) top view of the film in a) coated with SiN by CVD.

example, are a thick coating (~100 μm) of a material with an extremely low thermal conductivity, typically yttria stabilized zirconia (YSZ). In the past, most thermal barrier layers have been deposited with a plasma spray deposition process [76,87]. More recently, there has been a shift toward electron-beam evaporated YSZ because of improved thermal

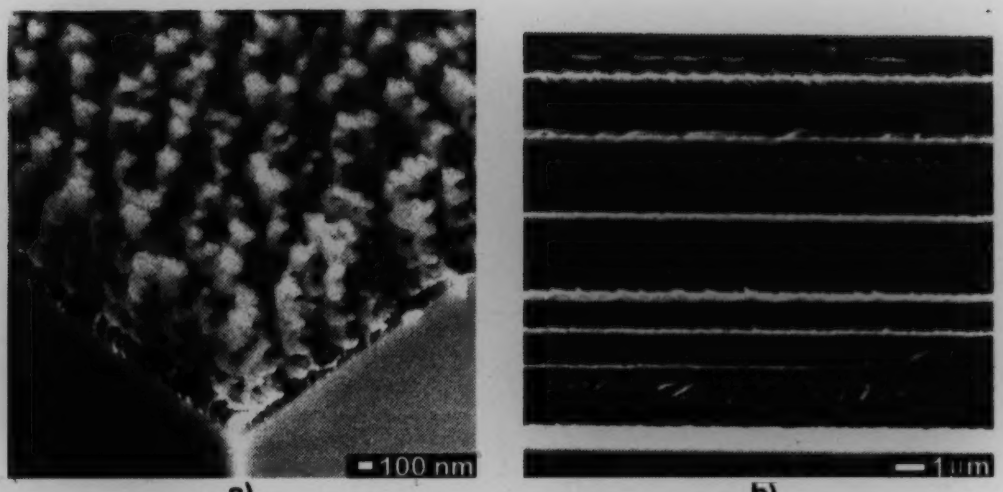

Figure 33: a) Helical zirconia (ZrO_2) film demonstrating GLAD control of structure for this important thermal barrier material, b) SiO realization of a thermal barrier coating design. Dense layers are alternated with porous layers to produce a robust coating with low thermal conductivity and thermal stress relief.

---

and mechanical properties [135]. The columnar structure of electron-beam deposited YSZ provides improved thermal insulation, because of the lower conductivity of the pores and grain boundaries of the structure, and improved resistance to thermal fatigue cracking, because the columnar structure allows expansion and contraction of the coating without fracturing. GLAD techniques appear promising as they would allow greater control of the structure, enabling engineered porosity and column shape. Columnar structure of YSZ can be controlled with GLAD, as is demonstrated with the helical film shown in Figure 33a. A thermal barrier design might be similar to the SiO film shown in Figure 33b, designed and fabricated with K. Harris, where dense (α small) and porous (α large - lower conductivity and thermal stress relief) layers are alternated to produce a robust coating while allowing thermal stress relief and enhanced thermal insulation in the porous regions. An additional benefit is that this film structure can be designed to Bragg reflect infrared radiation (See "Interference Optics" on page 113.) and further improve thermal characteristics. The SiO film shown in Figure 33b in fact displays a strong reflection peak in the infrared, matching the periodicity of the index varying structure.

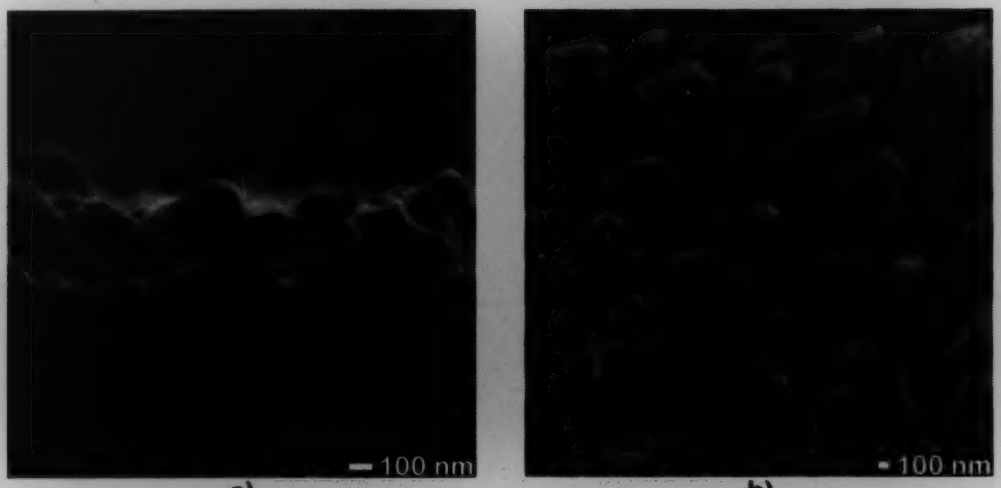

Figure 35: Organic dichroic dye evaporated with GLAD using a substrate motion intended to produce a single zigzag structure.

3.4b) dental adhesives

It is very difficult to anchor implants into the hydroxyapatite of teeth, and one idea is to provide small scale 'hooks' on an implant. This technique may find application in a variety of anchoring techniques in biological and other systems. A GLAD film with an inclined structure could conceivably be used to coat the shaft of an implant. The structure would slide easily into the tooth material in one direction, but microscopically lock into the surrounding material when pulled in the other direction. Figure 34 shows a Cr film, fabricated with J. Parks, deposited onto the cylindrical shaft of a dental implant pin. Raised ridges created in the machining of the pin caused shadowing during deposition, resulting in GLAD film growth only on the high points. As desired, however, the film growth does occur inclined axially along the shaft, and may allow use as a dental adhesive treatment.

3.4c) organic materials

All film depositions described in this thesis have been with inorganic materials - metals, metal oxides and fluorides, and semiconductors. There are a number of organic materials that can be evaporated with standard evaporation techniques that may be controlled with GLAD in a similar fashion to the inorganics described in this thesis. Figure 35 shows a dichroic organic dye deposited with GLAD in an attempt to produce a

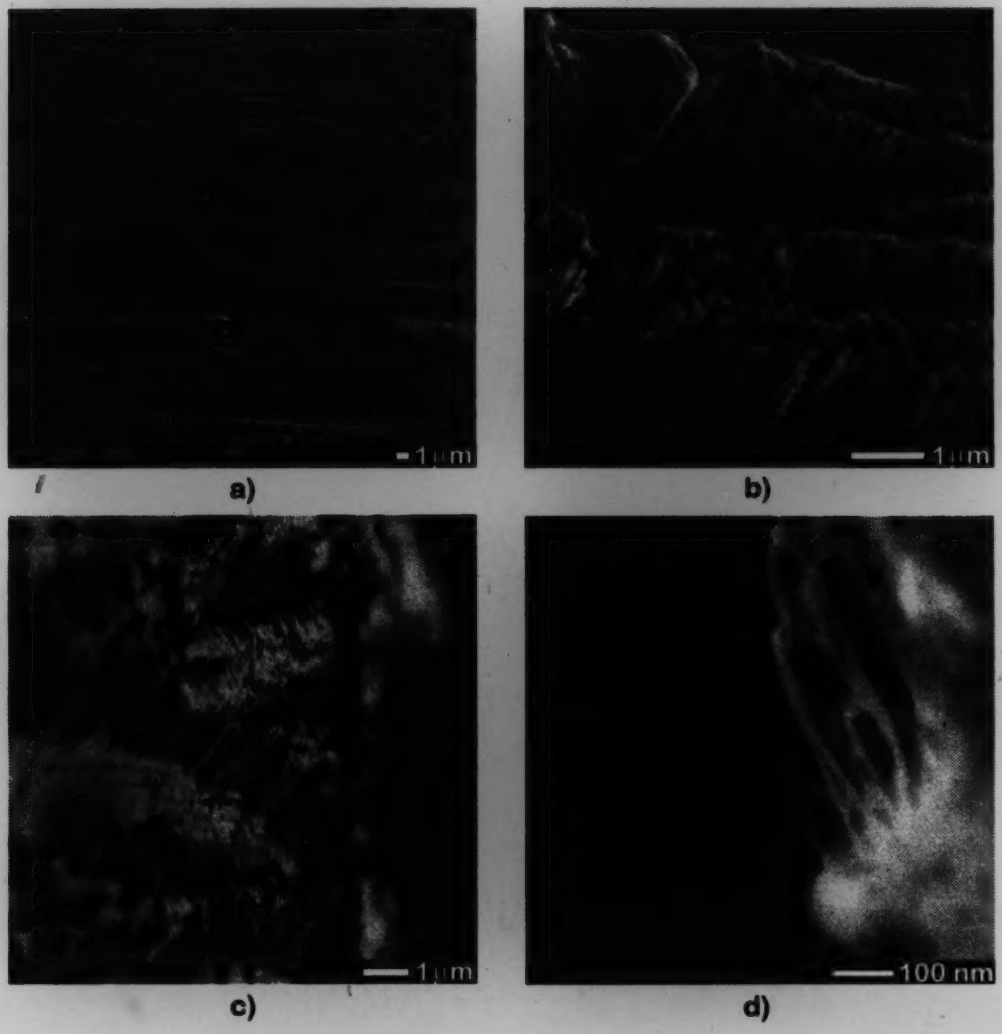

Figure 34: Cr film coated onto the cylindrical shaft of a dental implant. Circumferential ridges, created in machining of the shaft, result in GLAD film deposition only onto raised areas. The four images (a, b, c, and d) are different areas and orientations taken of a single film.

zigzag or chevron structure. The organic material displays structure, with some anisotropy, suggesting that GLAD has at least some effect on structure of this evaporated organic. When viewed between crossed polarizers, there was evidence of dichroism, arising from preferential alignment of the organic dye molecules by the oblique GLAD process.

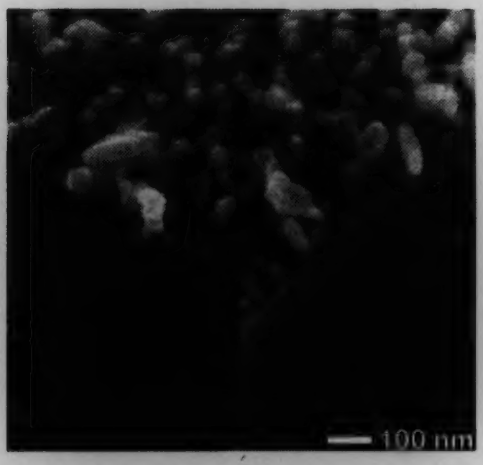

Figure 36: Porous GLAD platinum film.

3.4d) chemical sensors

The high surface area of the porous materials fabricated with GLAD suggest possibilities for application as chemical sensors. When a chemical species reacts with the surface of the film, it can change many of the film properties. Electrical conductivity, dielectric response, etc. will vary with surface reactions, indicating detection of the targeted sensing species. The films used in tests of electrostatic squeezing (See "Squeezing" on page 120.) are composed of a porous SiO film between Al electrodes, and are a suitable geometry to test a preliminary form of sensing. When humidity varies in the air surrounding the sensor, the capacitance measured across the electrodes changes. In initial tests conducted with A. Huizinga, substantial changes in capacitance were observed for very minor changes in humidity (for example, an additional person in a small room) by wiring the sensor as the capacitor in a resonant circuit, and observing the resonant frequency. Specific chemical species could be monitored by choosing the film material to undergo a desired chemical reaction with the target chemical [4,51,56]. Optical monitoring techniques could easily be used based on changes in the optical responses described in "Chiral Optics" on page 81 and in "Interference Optics" on page 113. The chemically important catalytic material platinum was briefly investigated for suitability for structural control with GLAD, but costs limited the trial to the one film shown in Figure 36. While a porous structure was observed with nanometer scale columns, no helical structure is

evident. Rapid rotation, and a very thin film, has resulted in a lack of helical structure, but because of the high melting temperature of Pt, and the correspondingly low adatom mobility, we expect that it should be easily (but not necessarily affordably) engineered with GLAD.

3.4e) magnetic materials

There is a long history of control of magnetic properties of thin films with oblique angle deposition [1,2,60]. Magnetic anisotropy, coercivity, and orientation vary with oblique incidence angle, α. Commercial Metal Evaporated (ME) tape is fabricated with an oblique deposition technique to exploits these effects. GLAD offers enhanced control over conventional oblique deposition techniques that may allow control of magnetic properties not possible with the stationary substrate methods currently used [22]. One example is the reduction of exchange coupling in magnetic media for hard-disk storage. Currently, Co-Cr alloys are sputtered onto disks, resulting in a fine-grained structure of tightly packed ~20 nm Co grains. Exchange coupling is reduced by composition segregation of the non-magnetic Cr. Cr diffuses to the grain boundaries and helps to magnetically isolate the magnetic Co grains. Unfortunately, even a few percent Cr content in the Co grains substantially degrades the magnetic properties of the Co. Current research into new material systems for magnetic media is concentrated on either optimizing the Cr/Co system for improved magnetic properties, or identification of new materials. The film shown in Figure 37 is a pure Co film deposited onto a rapidly rotating (ϕ) substrate at a fixed vapour incidence angle $\alpha = 85°$. It demonstrates that GLAD can produce physically separated, small grains (~25 nm diameter) which may help to reduce exchange coupling while eliminating the deleterious effects of Cr alloying.

3.4f) biomaterials

Materials used for biocompatible and biomedical applications frequently require a controlled geometry of porosity. Porous titanium plasma sprayed onto prosthetic devices promotes tissue and bone growth. Materials based on naturally porous structures, such as corals, are currently used in commercial biomedical applications [130,70]. Figure 38 shows a porous titanium film fabricated with GLAD. Structural control on the nanometer scale could enable use in biomedical applications.

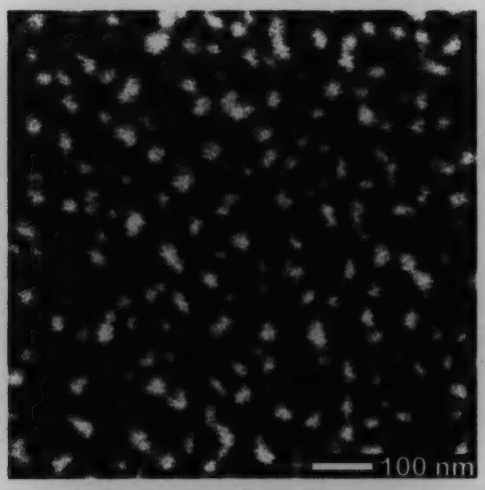

Figure 37: Co film deposited with GLAD demonstrating isolated ~25 nm diameter grains.

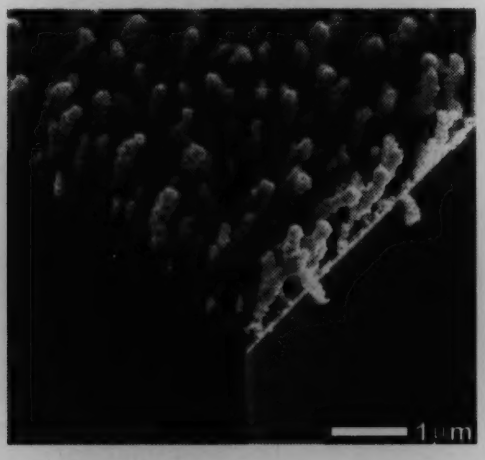

Figure 38: Porous Ti demonstration for biomedical applications. Controlled porosity allows design of biocompatible coatings.

3.4g) chiral catalysis

A huge portion of the chemistry in biological systems is stereospecific (See "chirality" on page 83.). Unfortunately, because of the similarity of the enantiomers in a stereo pair, stereospecific chemistry can be difficult. There is a great benefit in developing stereospecific catalytic products for use in the pharmaceutical and chemical industries. Stereospecific reaction rates have been observed on chiral quartz substrates as early as 1934

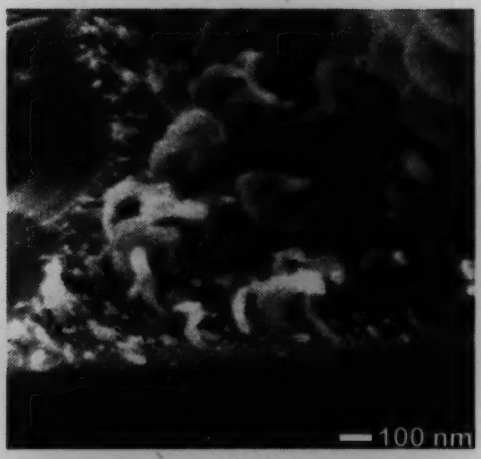

Figure 39: Small scale structure at initial stages of film growth. Before heating increases adatom mobility, film structures can be controlled on very small scale sizes.

---

[107], but designed stereo catalysts have not yet been realized. Attempts whereby a chiral molecule is used to induce chiral dislocations on a surface appear promising, but as yet have not yielded significant results [29]. Chirality in GLAD films might be used in stereo chemistry whereby the chiral structure of the GLAD material preferentially reacts with one enantiomer. One difficulty here is the differences in size between most chemical species of interest and GLAD films produced to date. Adatom mobility and heating effects ("adatom diffusion from heating" on page 40) limit chiral GLAD column sizes to 10s of nanometers, substantially larger than most chemicals used in pharmaceutical and chemical applications. Observation of the initial stages of film growth, before heating has increased adatom mobility, suggest that much smaller scale structures might be obtainable. Figure 39 shows a MgF_2 film that has fractured during preparation for SEM analysis. At the early stages of film growth, very small scale structure is observed. Substrate cooling or an alternate design of evaporation apparatus may allow stereospecific, chemically active, catalytic structures to be fabricated with GLAD.

4. Advanced Techniques for Structural Control[i]

The fabrication of structured materials, with vapour deposition techniques, has fundamental limitations which arise from the mechanics of the vapour deposition and film condensation processes. These limitations constrain the range of attainable structures. One example is that the mechanics of oblique deposition limit the possible 'tilt' angle of the columnar microstructure of fabricated materials. With the GLAD techniques described in this thesis, there is a limitation on structural control because the column inclination angle β and the film porosity cannot be controlled independently. Both of these structural characteristics are dependent on the oblique vapour incidence angle α. In this chapter, I present a modified GLAD technique for independent control of column inclination and film porosity. It enables the fabrication of a large range of microstructures not previously attainable.

4.1 Microstructure Restrictions

When thin films are deposited onto stationary substrates with the flux arriving at a non-normal angle α under conditions of limited adatom diffusion, an inclined columnar microstructure β is produced, Figure 7 (page 17). The column inclination angle β lies between the film normal and the vapour incidence angle α and is dependent upon many factors, including material, and deposition conditions, such as substrate and film temperature, angular distribution of the deposition flux, background gas pressure and composition, and flux energetics. However, it is accepted that there is a fixed relationship between flux angle α and column angle β for a given set of deposition conditions; the column angle β is uniquely determined by the choice of the deposition angle α. This relationship is complex and poorly understood, although a number of attempts at understanding and quantifying this relationship have been presented (See "column inclination" on page 16.). The empirical 'tangent rule' [88]:

$$\tan(\beta) = \frac{1}{2} \cdot \tan(\alpha) \tag{8}$$

---

i. Excerpted with permission from [96] K. Robbie et al., J. Vac. Sci. Technol. B, 16 (3) (1998), 1115-1122. Copyright 1998 American Vacuum Society.

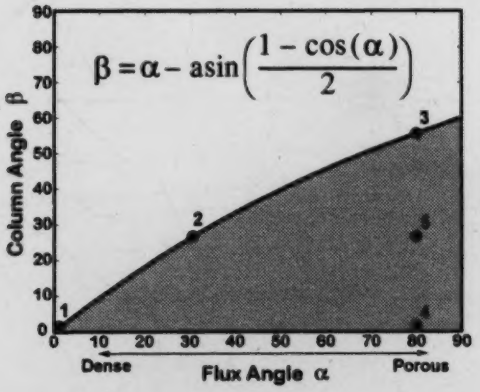

Figure 40: The solid line is the relationship of Tait [117] and describes the fixed relationship between the flux incidence angle α and the columnar growth angle β for a fixed set of deposition conditions (material, temperature, gas composition and pressure, vapour energetics). The shaded region is the microstructures attainable with the technique described in this chapter.

---

is a simple relationship based on near normal deposition and gives very poor results for α greater than about 50°. The relationship by Tait et al. [117] based on geometrical analysis:

$$\beta = \alpha - \text{asin}\left(\frac{1-\cos(\alpha)}{2}\right) \tag{9}$$

gives much better results for highly oblique angles (α large) (See "column inclination" on page 16.). While these relationships give some qualitative predictions of column angle β, they do not account for varied material or deposition conditions. For this discussion I have chosen to use the relationship proposed by Tait to describe this relationship, but must stress that this is only for illustrative purposes. Tait's relationship is shown in Figure 40. All columnar microstructures attainable with stationary substrate deposition are confined to the solid line of this graph (for a fixed hypothetical set of material and deposition conditions). So, for example, if a flux angle $\alpha = 30°$ were chosen for deposition, the resulting column angle β would be about 26°. Thus, points 1, 2, and 3 of Figure 40 indicate the resulting columnar microstructure inclination angles β if the flux angle α is chosen to be 0°, 30°, and 80° respectively. Scanning electron micrographs of chromium films deposited at $\alpha = 30°$ and 80° are shown in Figure 41 as are drawings illustrating α, β, and the resulting porosity.

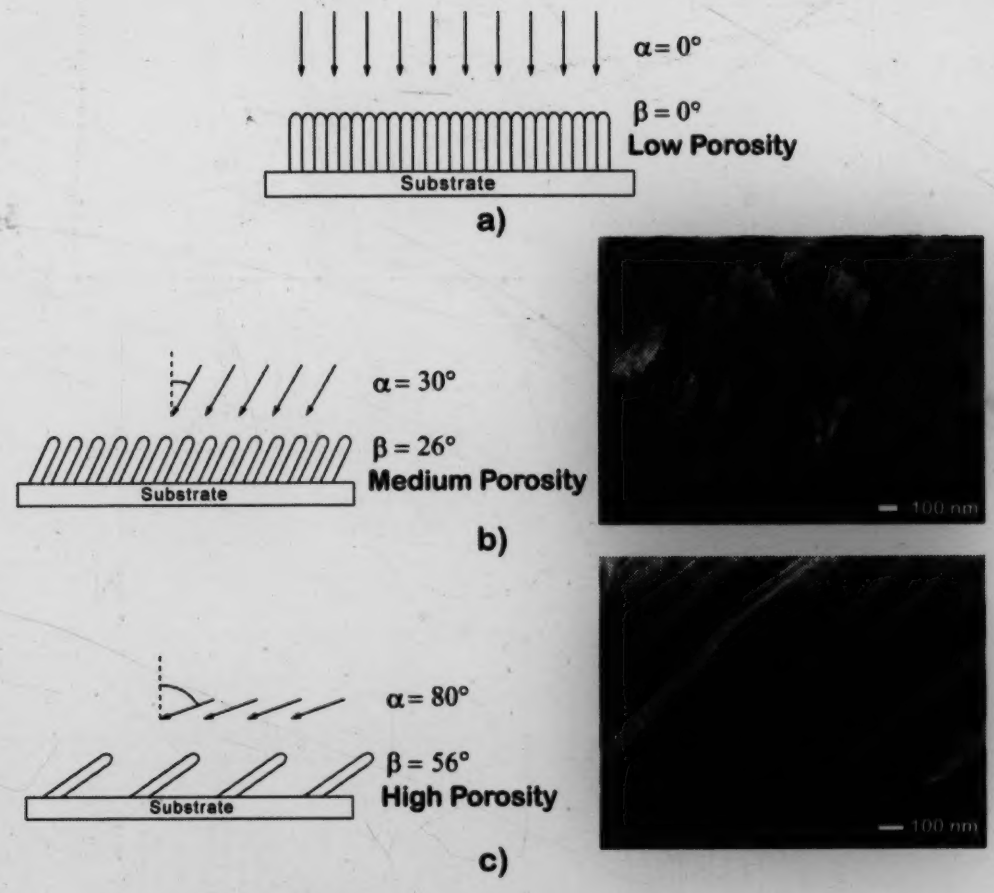

Figure 41: Cr films deposited at increasing oblique flux angle α onto stationary substrates. The film column angles β increase with flux angle α in a relationship similar to that described by Tait [117]. film porosity also increases with increasingly oblique flux angle.

The measured column inclination angles β for these films, deposited onto stationary substrates, approximately agree with the relationship proposed by Tait. Measured column inclination angles β are 22° and 52° for flux angles α of 30° and 80° respectively, while the column angles β predicted by Tait's rule are 26° and 56° respectively. These films also show the effect of film density change with increased oblique flux angle. The Cr film deposited at α = 80° is visibly more porous than the Cr film deposited at α = 30°. Measured porosities for films of 6 materials deposited at various oblique flux angles were presented

in Figure 15 (page 31).

Agreement with the rule proposed by Tait was also recently confirmed by Messier et al. [80] (shown in Figure 8 (page 18)) with a series of seven films of MgF_2 deposited onto stationary substrates with oblique flux angle α varying between 0° and 89°. Their results strongly confirm the validity of this rule for MgF_2 and suggest that an examination of the assumptions used in Tait's geometrical arguments may be useful in understanding column angle variation with varied material and deposition conditions.

From this earlier work describing the relationship between flux angle and column angle, it is seen that if one wished to fabricate a thin film with a specific column angle β, one could simply choose the desired β then read the required flux angle α off the graph of Tait's rule (or an experimentally derived equivalent for the desired material and deposition conditions). There is a significant limitation with this approach, however, in that the film porosity also changes with incident flux angle, as shown in Figure 41. Attempting to control the column angle β by simply varying the flux angle α causes the density to vary in a predictable but not independently controllable or desirable manner. This direct dependence on flux angle α of both column angle β and film density greatly restricts the range of thin film microstructures attainable. For example, a porous film with a vertical microstructure (point 4 in Figure 40) would be impossible. Point 4 represents a film with a column angle $\beta = 0°$, and with the porosity of a film deposited at the flux angle $\alpha = 80°$. Similarly, point 5, which represents a film with a column angle $\beta = 26°$ and a microstructure with the porosity of a film deposited with a flux angle $\alpha = 80°$, would also be forbidden. The new technique described in this chapter enables all microstructures represented by the shaded area below the line in Figure 40 to be fabricated. In this technique, the column angle and film porosity can be chosen independently. They may also be varied dynamically during deposition to produce complex structures.

4.2 Substrate Motion Techniques

In the following description of the advanced GLAD process, two substrate motion techniques are used to control column angle independently of film porosity; the 'zigzag' technique, and the 'spin' versus 'pause' technique. The 'zigzag' technique is based on the

effect that equal flux from two sides at equal polar flux angles α will produce vertical (β = 0°) porous microstructure[95]. The amount of deposition from the two sides is varied to control column angle β. The 'spin' vs.' pause' technique is based on the observation that when rapidly rotating the substrate during deposition (ϕ rotation), the flux appears to arrive equally from all azimuthal directions, and from a constant polar angle α. The resulting film has a vertical ($\beta = 0°$) columnar microstructure with the porosity set by the indent flux angle α. This effect is combined with stationary inclined oblique deposition, in a duty cycle manner, to allow any column angle β to be chosen independently of the film density.

The 'zigzag' technique may be better appreciated using an analogy in which we have two evaporation sources, one on either side of the substrate and with equal incident flux angles α. When 50% of the flux arrives from each of the sources, the resulting film has a vertical (β = 0°) yet porous structure as is depicted in Figure 42c. If 70% of the flux arrives from one source, and 30% from the other, more growth occurs toward the 70% source, and a somewhat inclined and porous microstructure results (Figure 42b). If all (100%) of the flux arrives from one source, an inclined and porous microstructure results (Figure 42a) with the column angle equal to that given by Tait's rule (this is simply conventional stationary substrate oblique deposition). To implement this technique with one evaporation source, the substrate was rotated (ϕ rotation) rapidly in 180 degree steps followed by pauses for deposition from each side (the 'zigzag' technique). In effect a 'zigzag' structure was created with each 'zig' lasting only long enough for a small amount (0 - 100 nm) of film to be deposited onto the crystal monitor. By varying the length of the 'zig' relative to the 'zag', the proportion of flux arriving from each side can be varied. This allows us to set the column angle β to any value between the maximum defined by Tait's rule and the normal to the substrate (β = 0°), while maintaining independent control over the porosity given by choosing the flux angle α.

Because this method is limited to two dimensional control, a second, more general, method was used to fabricate and control true three dimensional structures (the 'spin' vs. 'pause' technique). Instead of fixing the pause (or deposition) positions at 180 degree intervals of ϕ, the position of the pause is allowed to be placed at any azimuthal angle (ϕ). The deposition time during the pause is then varied relative to the deposition time during

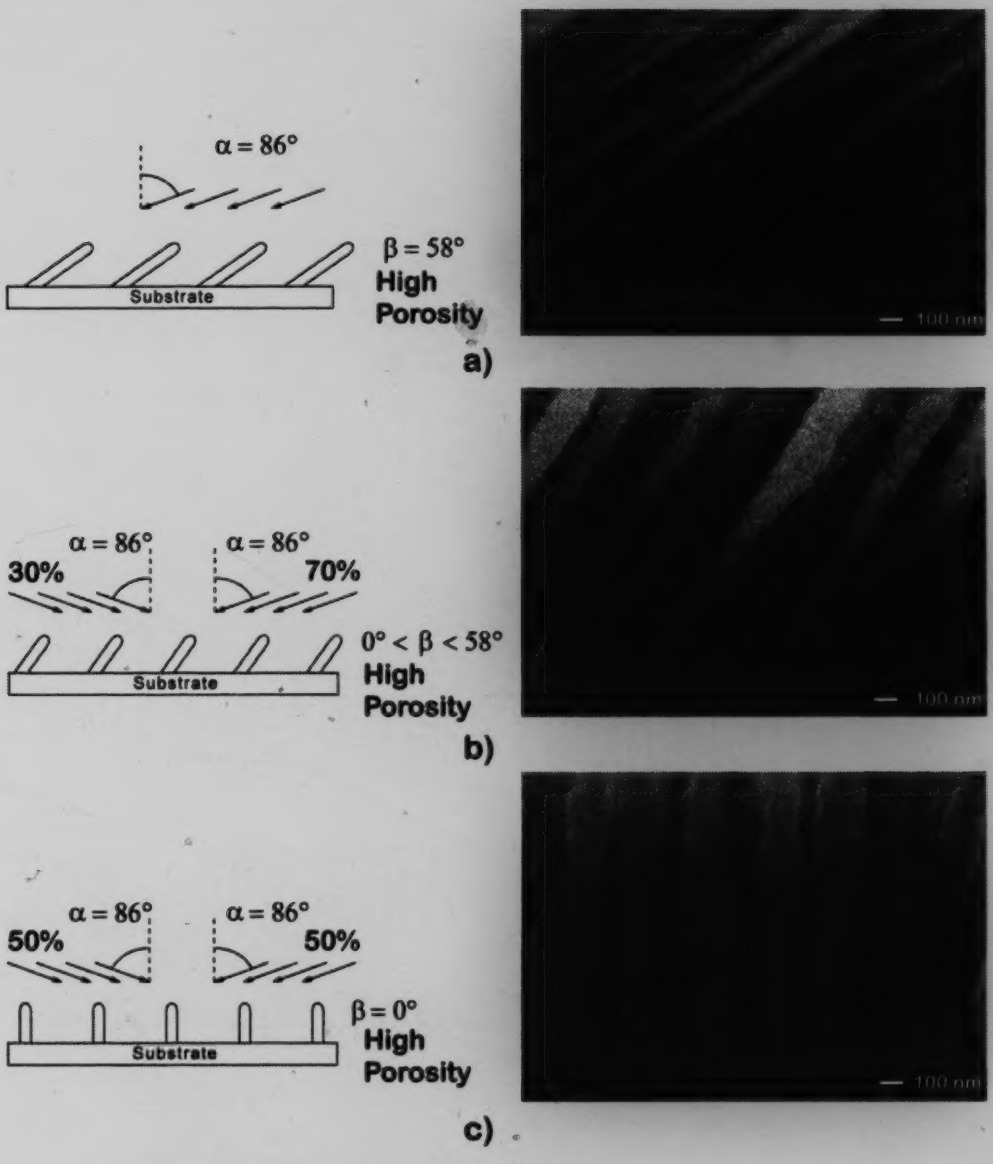

Figure 42: SiO films deposited with varying amounts of flux from two sides demonstrating independent control of column angle and film porosity. Porosity is approximately constant for all three films, while the column angle β) is controlled between inclined and vertical

the rotation from one pause position to the next. Growth that occurs while the substrate is rotating ('spinning growth') produces vertical microstructure, whereas growth while the

substrate is paused or stationary ('paused growth') produces inclined microstructure with the inclination angle given by Tait's rule. With our software implementation, the accumulated thickness on the crystal monitor during one complete rotation (called the 'minor pitch') is specified, and pause deposition thicknesses are varied relative to it. For all SiO films presented in this chapter, the 'minor pitch' was set to 20 nm and the pause length was varied relative to that thickness.

Thus, the microstructures of films created with advanced control GLAD depend on the choice of flux angle α, duty cycle of 'spinning growth' vs. 'paused growth', and the pattern of pause positions. To specify a desired microstructure, the flux angle α is chosen to control the film density, the duty cycle of 'spinning growth' vs. 'paused growth' is chosen to control the column inclination angle β, the pause position is chosen to control the local azimuthal direction of growth, and the time evolution of the pause position is chosen to control the type of three dimensional microstructure. Any of these parameters (such as flux angle α) can be varied dynamically during film growth to create even more sophisticated microstructures.

4.3 Advanced Structural Control Examples

Figure 42 shows SiO films deposited using the 'spin' vs. 'pause' advanced GLAD technique. The spin/pause growth proportions are equal to (0 / 100 %), (30 / 70 %), and (50 / 50 %) in Figure 42 a, b, and c respectively. The flux angle α was fixed at 86° for all three films resulting in high porosity. For these depositions, the pause position was kept fixed at $\phi = 0°$ corresponding to flux arriving from the right side of the views shown in the SEM micrographs of Figure 42. The density remains approximately constant, and the column angle β is controlled between the inclined (at the stationary deposition angle - Figure 42a) and the vertical (Figure 42c), demonstrating independent control of porosity and column angle. We observe, however, that the column diameter is larger for the vertical column film (Figure 42c) than for the inclined films (Figure 42a and Figure 42b). This effect is evident in the other films discussed below, and we believe that it is the result of two characteristics of the deposition process: 1) heating of the film and substrate during deposition due to radiant heat from the source and heat energy released from film condensation resulting in

increased adatom mobility as the deposition progresses; and 2) spinning of the substrate creating a geometrical effect where deposition occurs in a ring on the top of a film column instead of on a small disc as occurs during stationary substrate deposition. The significance of each of these effects is currently under investigation.

Periodically bent nematic (PBN) materials were proposed by Meyer [82]. They have not been observed in nature, yet theoretical analysis of their optical properties based on a liquid crystal model of their realization has been conducted [83,89]. The first claim of fabrication of a PBN was with the "Sculptured Thin Films" (STF) technique proposed by Messier et al.[80]. In the STF technique, PBN films with 'S' and 'C' shaped columns were produced by varying the flux angle α, and hence the column angle β, during deposition. While these films do have controlled column angle, they will also necessarily have a periodic density variation due to the varying flux angle during deposition. To produce the 'S' shaped columnar microstructure, film deposition is normal to the substrate ($\alpha = 0°$) for the vertical portions of the 'S', creating a high density film, and film deposition is oblique ($\alpha \sim 85°$) for the slanted portions of the 'S', creating a low density film [117,94]. Optically, the effective refractive index of the film will vary with the periodically varying density, causing the film to act as a multilayer or rugate interference filter with peak wavelength matching the periodicity of the 'S' or 'C' of the STF. We have intentionally exploited this effect in [101] to produce rugate interference filters. Also, as the STF technique employs near normal deposition, it can only be used effectively with materials which produce a pronounced columnar microstructure from near normal deposition. These materials are a small subset of evaporable materials and include MgF_2, which was the material used by Messier et al. to demonstrate the STF technique.

In this chapter, I present the first constant density PBN materials fabricated with the advanced control GLAD technique. In fabrication of 'S' or 'C' shaped columns with the advanced GLAD technique, the column angle is varied while maintaining a constant film density through application of substrate motion during deposition. The advanced GLAD technique is also not restricted to strongly column forming materials because it allows the flux angle to be kept oblique (α large), forcing columnar structure from materials which are quite uniform when deposited with the flux angle near normal (α small). I chose SiO to

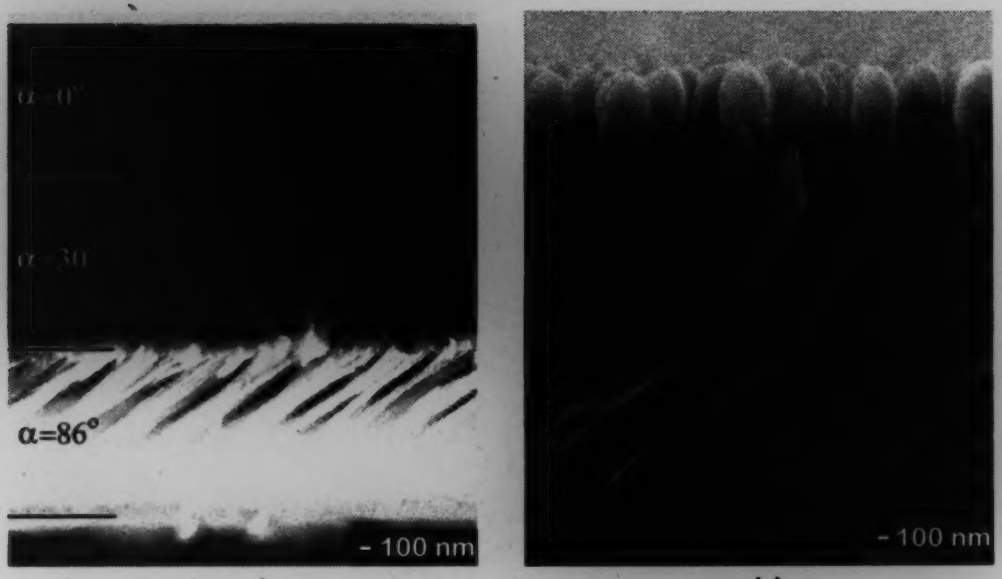

Figure 43: SiO films deposited in 3 steps, varying the column angle β. The column angle is varied by a) changing the flux incidence angle α, and by b) our technique of substrate motion during deposition while keeping the flux angle α constant at α=86°.

demonstrate the GLAD technique as it does not form distinct columnar microstructures when deposited near normal incidence, yet at oblique incidence can be forced to exhibit columnar structure and be shaped with GLAD.

Figure 43 demonstrates the difference between the STF and GLAD approaches to controlling column angle. The STF approach of changing the flux angle α to control column angle β was used in Figure 43a while the GLAD technique with the flux angle kept constant was used in Figure 43b. For both SiO films, deposition was performed in three steps and the goal was to vary the column angle β from that obtained with stationary oblique deposition (β = 58° for α = 86°) to that obtained with deposition normal to the substrate (β = 0° for α = 0°). Figure 43a demonstrates the density variation inherent in the STF technique. The lower third of the film is much more porous than the middle and the top is a structureless dense slab. If a strongly column forming material such as MgF_2 were used for these depositions, the resulting films would appear to be alike, but a strong density

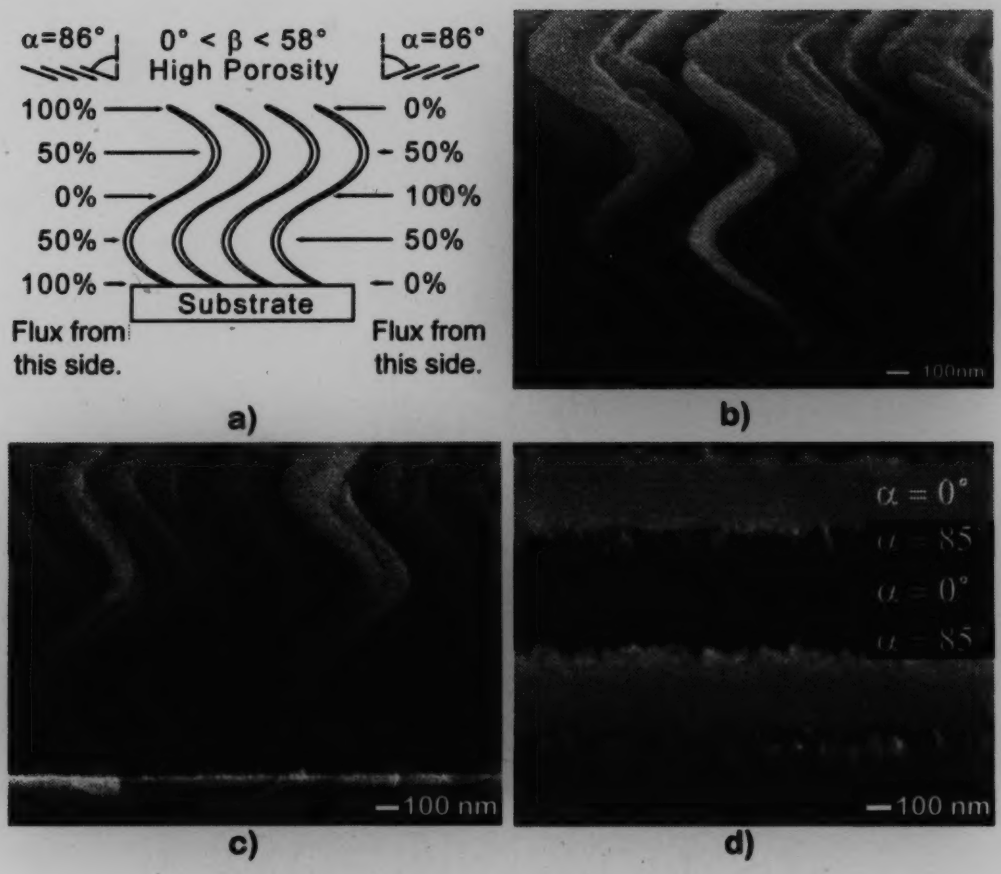

Figure 44: Schematic description and SEMs of SiO films with column inclination angle β varied dynamically during deposition while keeping the porosity constant (b and c). The flux angle α was fixed at 86° for b and c. These are thin film realizations of constant density periodically bent nematics. In d, the flux angle α was varied continuously between 0° and 85° four times with the substrate azimuthal position ϕ held constant.

variation would persist in the STF film where the flux angle α was varied. The film deposited with the GLAD technique (Figure 43b) has near uniform porosity as the column angle is varied from slanted to normal, although some increase in column diameter is evident.

The column angle can also be varied dynamically during deposition as is shown in Figure 44. In the two evaporation source analogy described earlier, this deposition

corresponds to varying the proportion of flux arriving from the two sources dynamically between 50% and 100% twice during the deposition. Figure 44b and Figure 44c illustrate the effect of similar but different advanced GLAD techniques. In Figure 44b, the 'zigzag' technique was used where the sum of the 'zig' deposition and the 'zag' deposition thicknesses was fixed at 100 nm on the crystal thickness monitor. To control the column angle, the proportion of the 'zig' relative to the 'zag' was varied. The individual 'zigs' and 'zags' used to control column angle can be seen in the first 200 nm of growth of the film shown in Figure 44b, before heating from the evaporation process has heated the film and substrate and increased the adatom mobility. In Figure 44c, the 'spin' vs. 'pause' technique was used. The relative proportion of growth while the substrate was spinning ('spinning growth') was varied relative to the growth while the substrate was stationary ('paused growth'). As the minor pitch was set at 20 nm, the structural building blocks ('spinning growth' and 'paused growth') were much smaller than those with the 'zigzag' technique and the stepwise growth cannot be seen even at the early stages of growth. Figure 44d demonstrates the result if one attempts to produce this structure by varying the flux angle α, in the manner of the STF technique. The flux angle α was varied continuously between 0° and 85° while the azimuthal angle was held constant. In the SEM micrograph, the structured thin layers were deposited with the flux angle α large, and the broad uniform layers were deposited with more normal flux angles. The periodic density inhomogeneity of Figure 44d creates an effective index variation, causing the film to have a brilliant red colour from an interference reflection peak. For strong column forming materials such as MgF_2, a more 'S' shaped columnar microstructure would result, similar to Figure 44b and Figure 44c, but with a strong periodic density variation.

The films in Figure 44b and Figure 44c are thin film realizations of the periodically bent nematic (PBN) concept proposed by Meyer [82]. These films have the required periodic structure and, with our advanced GLAD technique, density inhomogeneity has been largely eliminated. We expect these films to have similar optical properties to the theoretically conceived liquid crystal concept of a PBN, including various Bragg phenomena [83,124].

The 'zigzag' technique is limited in that it is a two dimensional method. Because

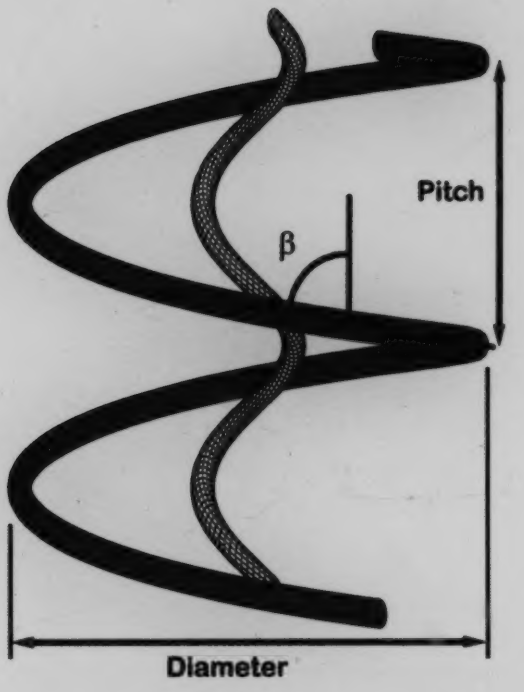

Figure 45: Two helices with equal pitch but different column angles β and diameters. The outer helix represents a helix which can be produced with conventional substrate rotation. The inner helix represents a helix which can be fabricated with advanced GLAD techniques.

the flux arrives from only two sides, control of only two dimensional structures can be achieved. Also, films deposited in this manner frequently have strong structural anisotropy in the plane of the film[95,118]. This anisotropy may be useful, but in many applications would be detrimental and should be minimized or eliminated. In the more general method of deposition 'spin' vs. 'pause' where the pause position can be any azimuthal angle ϕ, and the amount of growth during a pause is varied relative to the amount of growth during rapid spinning, complex three dimensional structures can be fabricated.

An example of the degree of control possible with this technique is demonstrated in Figure 45 and Figure 46. If a helix is fabricated with one rotation of the substrate for one rotation of the helical columnar growth, the column growth angle is fixed at the value set by Tait's rule. This is represented by the outer and darker helix of Figure 45 and is shown

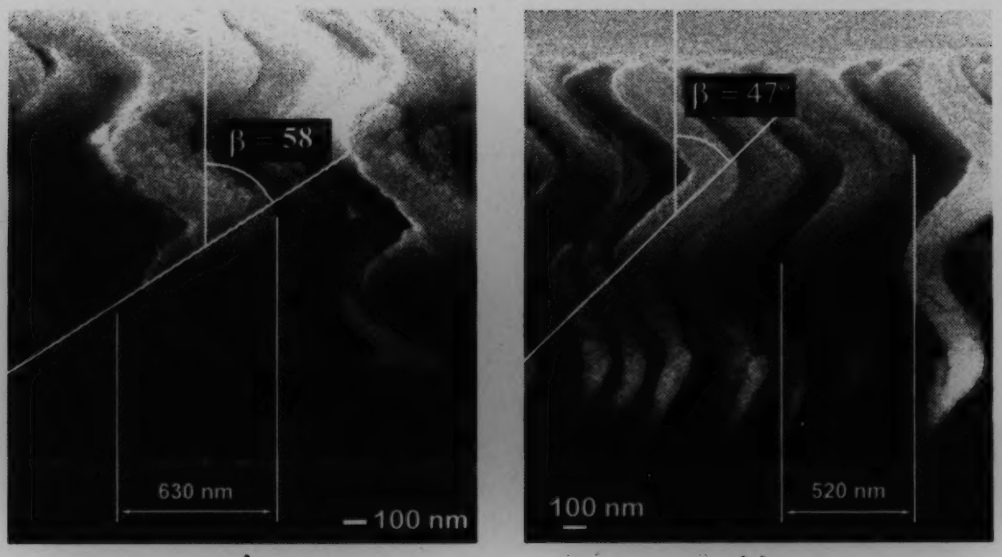

Figure 46: Two helical columnar films of SiO deposited with a) conventional GLAD with substrate rotation resulting in a column angle β equal to that resulting from stationary substrate deposition, and b) the advanced GLAD technique where the column angle is made more normal while keeping the porosity constant.

---

in the micrograph of Figure 46a. The fixed column angle constrains the diameter of the helix for a chosen pitch. Figure 45 shows two helices with equal pitch, but different column angles β and helix diameters. The inner helix cannot be fabricated with single substrate rotation equal to single helical rotation deposition, but can be fabricated with the advanced GLAD technique. This is demonstrated in Figure 46. Figure 46a was fabricated with 3 substrate rotations for 3 helical column rotations. The column angle is equal to that specified by Tait's rule and the helix has a large diameter. In Figure 46b, 80 rotations of the substrate were used to produce 2 helical column turns. This deposition was performed with a series of ϕ rotations of 369° followed by short pauses for deposition. This is the 'spin' vs. 'pause' duty cycle technique for three dimensional structures. The film porosity was specified by choosing the flux angle α to be 86°, the column angle β was specified by choosing the duty cycle of 'spinning growth' vs. 'paused growth', and the helical

microstructure was specified by choosing a simple precessing angle of the pause position ϕ. The column angle has been made more vertical (β smaller than specified by Tait's rule), and the helix diameter has been reduced for a helix with a pitch approximately equal to that of the helix in Figure 46a.

While this example of changing helical geometry may appear simplistic, Venugopal et al. [124] have shown theoretically that optical properties, such as second harmonic generation, of chiral structures like those fabricated with GLAD, depend strongly on helix geometry. Greater control over structure will allow optical response to be tuned and optimized in a manner not previously possible.

5. Chiral Optics

The structure of thin films fabricated with GLAD can be controlled on a nanometer scale, in three dimensions. This unique degree of control allows many properties of the resulting materials to be engineered. Optical properties, in particular, are easily controlled due to the manner that light interacts with a medium composed of optically small regions of varied electromagnetic response [69,74]. The porous nature of GLAD film materials (See "Growth Mechanics" on page 25.) allows us to mix two mediums, with different electromagnetic responses, with a great degree of control, and at scale sizes ranging from shorter (~10 nm) to longer (~100 μm) than the wavelengths of visible light. The two mediums that are mixed are the film material, and the pores (the space between the columns), that can be filled with air or other materials. Liquids and gases easily permeate GLAD materials, and solids may be incorporated in the pores with chemical vapour deposition (CVD), high temperature injection [47], chemical deposition, or other techniques that allow the filling of nanometer scale structures. A polymer can be used to fill the pores by impregnating the pores with the desired monomers, then polymerizing with heat or UV radiation.

Materials composed of mixed mediums, on scales comparable to the probing light wavelength, are generally described by 'effective medium' theories. Maxwell-Garnett [35] and Bruggeman [16] theoretical formulations are the basis of extensive work describing mixed mediums [111,47,53,48,49,50,68,65,70]. An excellent review is given in 'Selected Papers on Linear Optical Composite Materials' [69]; the introduction entitled 'Cakes and Pastries, and Linear Optical Composite Materials Too', by Lakhtakia, is a humorous, but effective discussion of the range of composite materials study.

By controlling the structure of a GLAD film material, optical properties can be tailored to produce optical filters and devices with desired properties. Circular polarizers [52], retardation plates, isolators, frequency converters [124], notch filters [133,134], rugate filters [101], transparent conducting materials [50], optical sensing devices, and other optical components appear promising as achievable with GLAD [70].

Work in this chapter concentrates on two main topics: optical properties of chiral GLAD films; and optical properties of hybrid materials, where the film pores have been

filled with liquid crystalline materials. The following chapter will discuss another form of composite optical material that can be fabricated with GLAD, interference (or rugate) filters. A precise electromagnetic description of the materials is: chiral GLAD films are rotationally inhomogeneous, bianisotropic mediums [65], while GLAD interference filters are linearly inhomogeneous uniaxial mediums [101].

5.1 Chiral GLAD Films

Chiral GLAD films, composed of helical shaped columns, have optical properties similar to the technologically important chiral nematic (or cholesteric) liquid crystals (CLCs), including optical activity (or circular birefringence - rotation of the polarization orientation of linear polarized light), and circular dichroism (selective absorption/scattering of one circular polarization of light) [100,104,105]. We have found that while helical films and CLCs have many similar optical properties, helical films also exhibit unique effects not seen in CLCs [17,99] or in isotropic chiral mediums [9].

'Chiral optics' describes the class of optical effects that result when films with helical column shapes are fabricated with GLAD. Note, however, that while helices are chiral objects, chiral objects aren't necessarily helical, and chiral GLAD films needn't be helical either. Helices are simple chiral objects, which are amenable to scientific investigation, and were, therefore, chosen as the chiral objects of study for initial experiments. The 'square helix' shown in Figure 12e (page 26) is also a chiral object and may exhibit, in some form, the optical effects described here.

The observed optical response of chiral GLAD films described here is scientifically interesting, and technologically promising, and suggests that new types of chiral optical filters and devices will be possible with GLAD. It also confirms the similarity in response of chiral GLAD films and chiral liquid crystals (CLCs), and suggests that GLAD films may be useful for a variety of applications envisioned for CLCs. GLAD films may be used in applications that CLCs are too delicate for, such as high power or high temperature filters. Also, with GLAD, complex structures are simple to fabricate with minor software modification, allowing great flexibility for engineering of optical response. Figure 47 shows a variety of column shaping techniques that are easy to perform with GLAD that

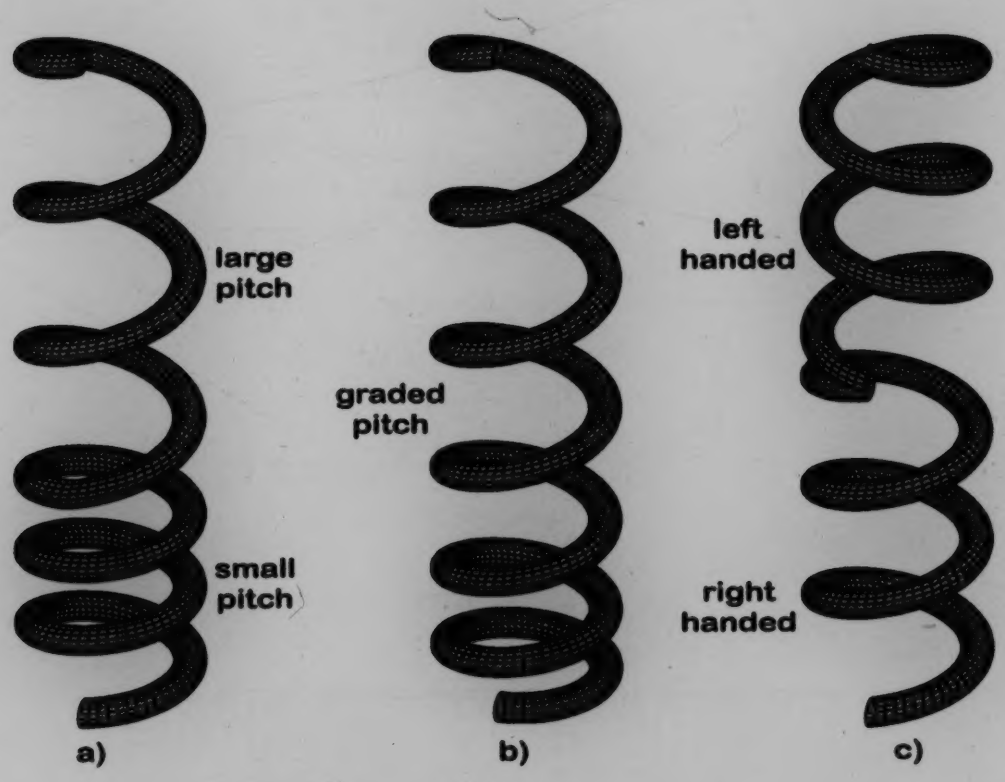

Figure 47: Chiral film column shapes which are easy to fabricate with GLAD including a) multiple pitches, b) graded pitch, and c) varied handedness. These structures are difficult, if not impossible, to create in chiral liquid crystals (CLCs).

---

could be used to tailor optical properties. These structures are difficult, if not impossible, to create in CLCs, where engineered structures (such as graded pitch) are currently created with elaborate chemical techniques like diffusion controlled UV polymerization [15].

5.1a) chirality

The term *'chirality'* (from the Greek *chir* = hand) was introduced by Lord Kelvin in his Baltimore Lectures, delivered in 1884, to describe an object "if its image in a plane mirror, ideally realized, cannot be brought to coincide with itself". It has replaced the similar term *'dissymmetric'* used by Pasteur to describe objects "which differ only as an image in a mirror differs from the object which produces it" [91]. A helix is a chiral object because it, and its mirror image, cannot be superposed (made to coincide with), since

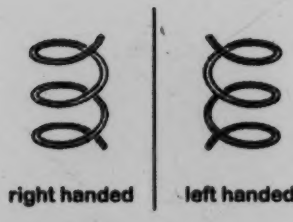

Figure 48: A right handed helix and its left handed mirror image. These different enantiomers cannot be superposed (made to coincide with each other) under any spacial rotation or displacement.
This figure is from Barron [9].

reflection reverses the screw sense (Figure 48) [9]. A chiral object has two possible states, called enantiomers, and the objects are said to exhibit enantiomorphism. Pasteur [91] and Fresnel [30, 31] established the chiral structure of optically active molecules through the study of optical rotation (optical activity) in fluids (such as turpentine) or solutions (such as sugars). For many years, Pasteur investigated solutions that exhibit optical activity. There was great interest in the similarity between the optical activity observed from solutions and that seen from chiral crystals, such as quartz (which has two chiral states or enantiomers), and finally, he crystallized paratartaric acid from solution and separated (with tweezers, under a microscope) the left and right handed crystals. When he formed solutions with the separated crystals, he found that the 'left' crystals caused a clockwise rotation, the 'right' crystals caused a counterclockwise rotation, and a solution composed of equal parts (racemic mixture) of either handedness caused no rotation. From this, he proposed, correctly, that the rotation was caused by the form of the molecules in solution, and that there existed two distinct states, or enantiomers, that were identical in chemical composition, but varied in form.

Since the time of Pasteur and Kelvin, science has seen the importance of chirality in everything from crystal formation to molecular biology to elementary particle physics (where interactions depend absolutely upon right and left handedness in spin polarized particles) [10]. In molecular biology, all amino acids which make up the proteins in biological systems have two possible enantiomers, yet only the left handed forms are found in terrestrial biochemistry. Amino acids found in meteorites, however, contain very nearly

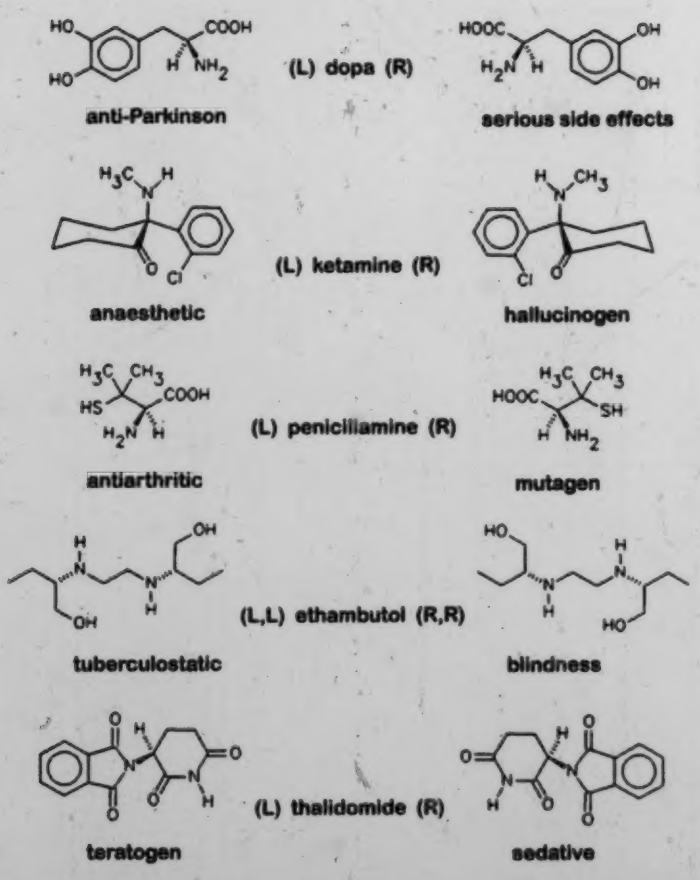

Figure 49: Chirality in medicine. Identical drugs in chemical composition can have very different effects depending on enantiomer. Thalidomide (R) was widely prescribed in the 1950s as a sedative to pregnant women. Unfortunately it racemerizes (switches enantiomeric states) in the human body creating L thalidomide which causes birth defects (teratogen).
Figure courtesy of Dr. K.-H. Ernst, EMPA.

racemic (equal parts left and right handed enantiomers) mixtures of amino acids. Figure 49 and Figure 50 show examples of chiral molecules in chemistry and medicine. An excellent review of the role of chirality in systems ranging from elementary particles to the deep space origins of life is given in [6].

5.1b) optical activity

The first observation of the effects of chirality on optical response of a medium was

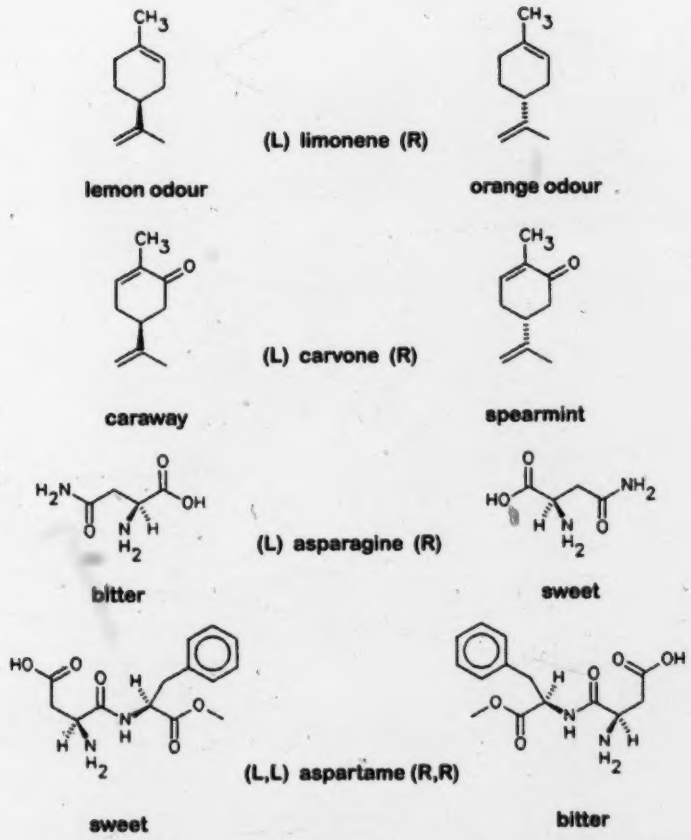

Figure 50: Examples of handedness in organic chemistry. While identical in chemical composition, different enantiomers can have quite different effects in biochemical reactions.
Figure courtesy of Dr. K.-H. Ernst, EMPA.

---

the observation of colours in sunlight upon transmission through a quartz crystal, along its optical axis, and between crossed polarizers, by Arago [3]. This effect was called 'optical activity' and is now known to be a fundamental characteristic of chiral materials. A solution of chiral molecules that exhibits optical activity is described as an isotropic chiral medium, because the orientation of the chiral molecules is random. This is different from chiral GLAD films where all the helical axes are aligned, perpendicular to the substrate, or from chiral crystals where there is also a strongly preferred orientation. When electromagnetic (EM) waves (light or microwaves, for example) interact with a chiral

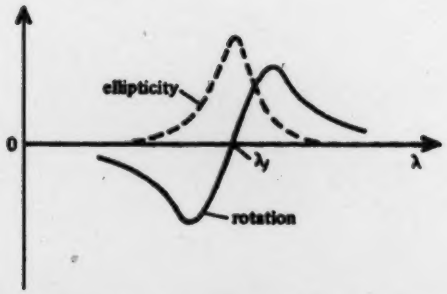

Figure 51: Optical activity in solutions of chiral molecules.
This figure is from Barron [9].

medium, the resulting fields (reflected, refracted) can be described as resulting from scattering of the EM wave from the electrons and nuclei of the medium. The sum of the interference of the scattered waves specifies the radiation field produced by the excited medium. Chiral objects scatter right and left circularly polarized EM waves differently, leading many theoretical and experimental investigators to employ circular polarizations of EM waves. The theory of optical rotation proposed by Fresnel in 1825 [31] attributed rotation of the plane of polarization of linearly polarized light to a difference in velocity of propagation of left and right circular polarized components of the linearly polarized light in the medium. The phase difference between the circular polarized components rotates the orientation of the plane of polarization of linearly polarized incident light. Newer treatments describe the chiral objects quantum-mechanically and investigate the interaction of wave functions to describe the radiation field [9].

'Optical activity' describes the alteration of the orientation and ellipticity of the incident light polarization state upon reflection from, or transmission through, a chiral medium. Typical optical rotation and ellipticity spectra, observed upon transmission through a solution of chiral molecules, are shown in Figure 51. Similar optical activity spectra are observed in chiral liquid crystals (where there is a helical structure of stacked layers of uniaxial molecules) [36], in chiral crystals (where there is a helical rotation of crystallographic anisotropy), and in solutions composed of chiral molecules. It occurs when there is a preferred interaction (absorption in chiral molecules and Bragg reflection in chiral liquid crystals) between the medium and one of the right or left circularly polarized

components of the EM wave. Barron shows that these interactions arise from non-zero components of the real dynamic material property tensors arising directly from the shape of the chiral medium [9]. Scattered light is composed of fields radiated from induced oscillating charges and currents excited within medium, by the incident light wave. Recently, Lakhtakia and Weiglhofer [68,65,67,66] have proposed a framework for describing 'Helicoidal Bianisotropic Mediums' (HBMs) for theoretical investigation of chiral, and other, complex materials, including CLCs and GLAD chiral films.

Experimentally, electromagnetic properties of chiral media have been investigated with light in CLCs and chiral polymers [25,15], microwaves in wire spirals [9], and other chiral systems with suitable wavelength EM radiation. The first observation of polarization effects in chiral thin films was when Young and Kowal [132] observed optical activity at a single wavelength, in MgF_2 films deposited obliquely onto a rotating substrate. At the time (1959), no structural analysis was performed (such as by SEM), but the optical activity suggests that the film structure may have been similar to some of the helical films shown in this thesis. However, the films were deposited at much shallower deposition angles ($\alpha<60°$) than is used for most of the work herein, suggesting much denser films (of nearly bulk density) than are typically shown here. Their optical rotation measurement suggested the 'chirality' of films deposited onto rotating substrate, yet their measurements were at one wavelength, limiting the usefulness of the analysis. Optical activity in a chiral medium varies with the incident light wavelength (producing the strongest effects when the light wavelength in the film matches the physical periodicity of the chiral medium), and the phenomenon is called optical rotatory dispersion [69].

The optical rotatory dispersion spectrum of the 15 turn MgF_2 helical thin film shown in Figure 12d (page 26), and Figure 57a, was measured with a polarimetry technique (Figure 52) for a range of wavelengths, 560 nm $\leq \lambda_{vac} \leq$ 633, in the visible spectrum, and is shown in Figure 53. The measurement was performed with A. Elezzabi and M. R. Freeman of the Physics department of the University of Alberta. From comparison with CLCs [9,25], we expect that optical rotation will be largest near where the pitch Ω matches the wavelength of light in the film, which can be described as the light wavelength in vacuum, λ_{vac}, divided by a suitably averaged refractive index n_{avg} of the film [69]. In order

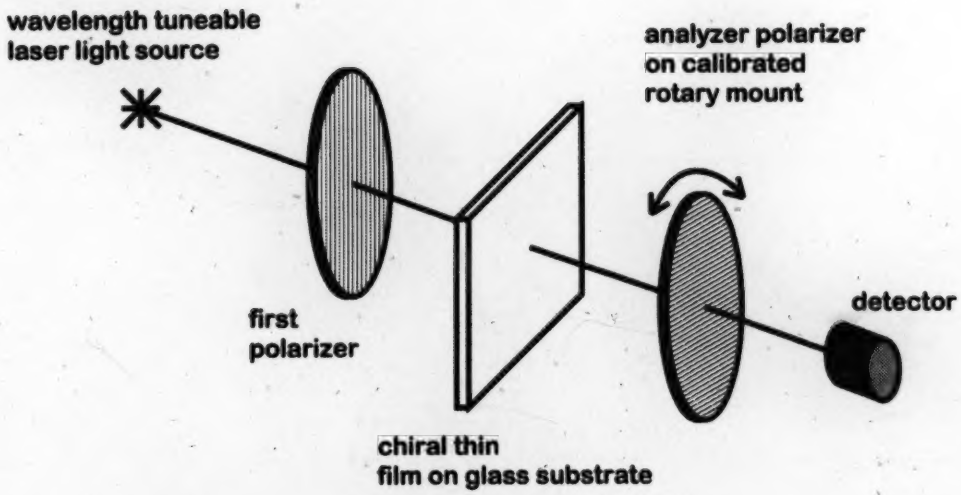

Figure 52: Polarimetry technique used to measure optical rotatory dispersion of chiral thin films.

---

to estimate n_{avg} of the MgF_2 chiral thin film, density measurements and a simple mixing rule were used. The average index was estimated as the density weighted sum of the index of the film material (MgF_2, $n = 1.38$) and the index of the air in the pores ($n \approx 1.0$) [69]. This is a substantial simplification, but acceptable for initial investigation; more detailed electromagnetic response theories are described in [68,65,69]. With $n_{avg} \approx 1.2$ and $\Omega \approx 320$ nm, we expect the MgF_2 thin film to show very large optical rotation when $\lambda_{vac} \approx 400$ nm. In the same regime, strong circular dichroism (depolarization of linearly polarized light) is expected [9,25] as one circular polarization is strongly scattered from the helix. In CLCs, the circularly polarized waves with the same sense as the helix are specularly reflected, producing bright colours in this wavelength range. One must be cautious with comparisons between CLCs and chiral films fabricated with GLAD, however, as the former are locally uniaxial, whereas the later are locally biaxial (See "ellipsometry and effects of orientation" on page 91.). Theoretical investigations describe CLCs as a multilayered system of thin uniaxial layers with a small rotation of orientation between each layer [17]. Chiral films produced by oblique deposition are similar to a first approximation, but must be treated as biaxial to obtain an accurate description. When materials that are not purely dielectric are used to construct chiral films, helicoidal bianisotropic descriptions must be used [65].

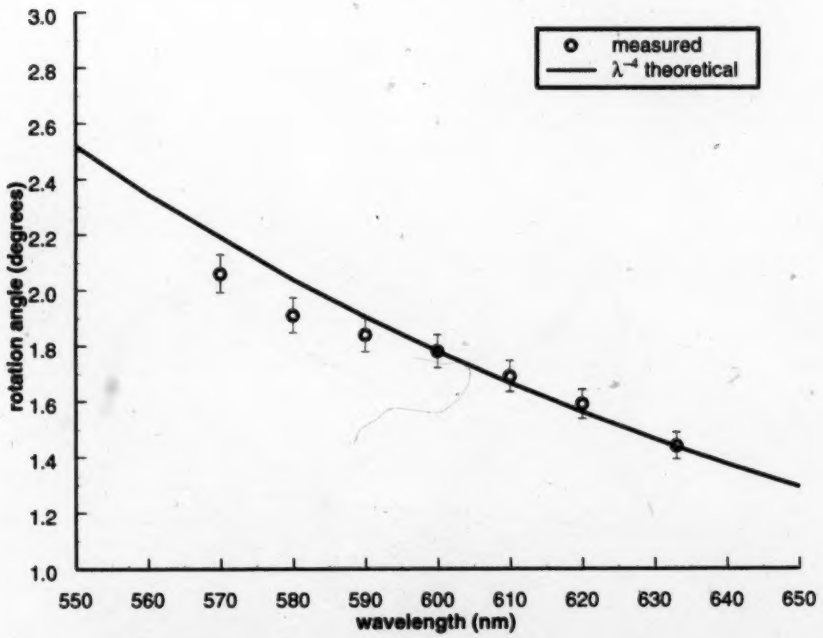

Figure 53: Optical rotation as a function of wavelength (optical rotatory dispersion) of the MgF_2 helical (chiral) thin film shown in Figure 57. The solid line shows the λ_{vac}^{-4} behavior predicted for chiral nematic liquid crystals by the de Vries formula at large values of λ_{vac}/Ω [27].
This figure is from Robbie et al. [100].

Optical rotations, in the wavelength region of Figure 53, were measured for enantiomeric pairs of chiral films (an identical pair where one has exclusively left-handed helices and the other has exclusively right-handed helices). Measured values were found to be counterclockwise for the right-handed helices and clockwise for the left-handed helices of the enantiomeric pair, when looking into the beam. The magnitudes of the two optical rotations were identical. In addition, no optical rotation was observed for a glass substrate without a film.

These measurements demonstrate the ability of GLAD to produce chiral films with the optical properties expected from chiral materials. The measurements are limited as they only measure optical rotation in a narrow range of wavelengths with the range not within the 'resonance regime' (the so-called 'zone II' in HBM literature [68], and the 'zone of

selective reflection' in chiral liquid crystal literature [58]). Also, the ellipticity of the transmitted polarized light was not measured. Together the optical rotation and the ellipticity of the transmitted light over a range of wavelengths, including the resonance region, are needed to characterize a chiral medium.

5.1c) ellipsometry and effects of orientation

To further investigate the optical properties of chiral thin films fabricated with GLAD, better characterization of the polarization state of the light upon transmission or reflection was required. Spectroscopic ellipsometry provides one excellent choice of analytical tool. Transmission ellipsometry analyses the polarization ellipse of an initially linearly polarized light beam, after transmission through a sample. While the polarimetry technique described above (Figure 52) analyses only the rotational orientation, ellipsometry analyses the transmitted polarization state in both orientation and ellipticity. Some forms of ellipsometry analysis even allow discrimination between right- and left-elliptical polarizations. Spectroscopic ellipsometry employs light of different wavelengths to probe the sample and allows for investigation of resonant regions where the wavelength of the light matches the periodicity of the chiral films.

Transmission ellipsometry was conducted at two locations on samples fabricated with GLAD. Measurements at the National Research Council in Ottawa, Canada, were conducted by me with assistance from Dr. G. Clarke, and P. Rovira conducted measurements at Pennsylvania State University in State College, USA [105] (on samples prepared by me). The first measurements showed an optical rotation spectrum through the 'resonance region', where the wavelength of the light matched the pitch of the helical film structure, but were unable to detect ellipticity variation or handedness because of equipment limitations. Effects of orientation on optical rotation were briefly examined with the ellipsometer in Ottawa. A more detailed analysis was then performed at Penn. State where a novel 'rotating-compensator multichannel' ellipsometry technique was used to allow accurate measurements of ellipticity and degree of polarization. Optical rotation spectra were comparable between the two ellipsometry techniques used.

In Ottawa, the ellipsometer used was a commercial, variable angle spectroscopic ellipsometer (VASE) instrument from J. A. Wollam Co. in the fixed polarizer, rotating

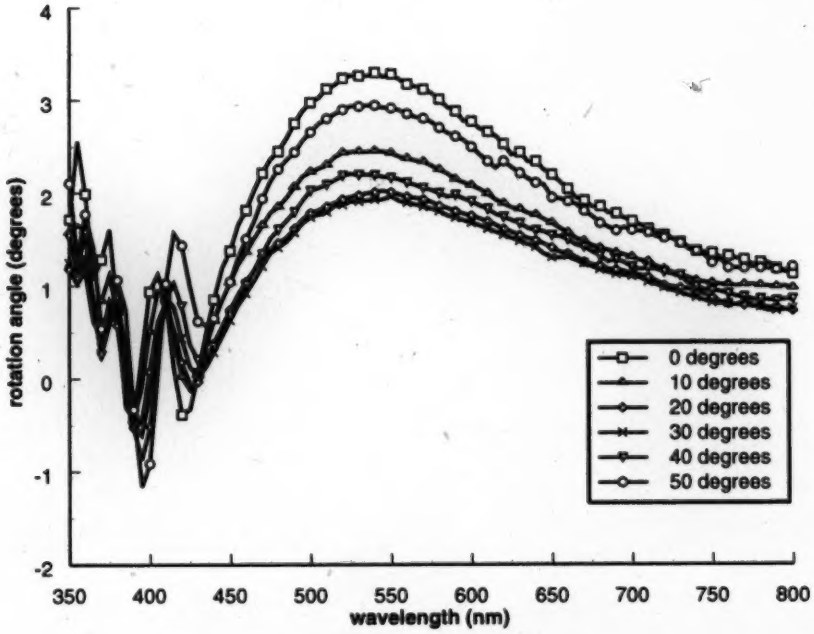

Figure 54: Optical rotation as a function of orientation of chiral film. The film is rotated in 10° increments about the helical axis which is parallel to the substrate normal.

This figure is from Robbie and Brett [99].

---

analyzer configuration. The optical rotation spectra shown in Figure 54 are for linearly polarized light incident along the helical axis, measured upon transmission through the film shown in Figure 57a. The long wavelength behavior is similar to the polarimetry measurements, performed on the same film, and discussed in the above section. Orientation of the chiral film relative to the incident linear polarized light was not recorded with the polarimetry measurements, so absolute comparison is not possible. The spectra in Figure 54 do show an interesting effect that is not observed in other chiral mediums. With both CLCs and isotropic chiral mediums, rotation about the helical axis has no effect on optical properties (there is no preferred axis for isotropic chiral mediums so any rotation is allowed). It is possible to understand the source of orientation effects on optical properties by examining the differences in the optical geometries of the various chiral mediums. Isotropic chiral mediums (for example, a solution of chiral molecules) are isotropic in their

response to light, with identical properties for any propagation direction. Chiral nematic liquid crystals are rotationally inhomogeneous, uniaxial, mediums where the helical axis is the axis of symmetry. They are well described as a stack of uniaxial birefringent sheets with a small rotation from one sheet to the next. Rotation about the helical axis has no effect on optical properties while propagation along any other direction will have varied response. Obliquely deposited thin films are rotationally inhomogeneous like chiral liquid crystals, but unlike CLCs, they are locally biaxial and have a non-zero rise angle of the helix above a plane perpendicular to the helical axis. Because of these differences, chiral thin films exhibit optical rotation that varies with rotational orientation about the helical axis.

While the structure of the optical rotation spectra in Figure 54 is very similar to that of CLCs, with sharp oscillations in the resonance region and a decrease toward zero at long wavelengths, the variation with rotation about the helical axis is unique to chiral thin films. The orientation dependence has a minimum in peak rotation (at about 550 nm) with the sample rotated between 20° and 30° from the arbitrarily set 0° position. Unfortunately, these measurements are limited and more detailed study is required to fully characterize the behavior. An analysis based on the theory of Barron [9], Chandrasekhar [17] and Lakhtakia and Weigelhofer [65] could be used to examine these effects, but more detailed experimental results would be beneficial.

The rotating compensator multichannel transmission ($PSC_{ROT}A$: Polarizer Sample $Compensator_{ROTating}$ Analyser) ellipsometer developed at Pennsylvania State University is shown schematically in Figure 55, and is described in detail in [26,105]. The rotating compensator ellipsometer configuration has many benefits over rotating polarizer and analyzer systems for measurements of the response of chiral thin films. It provides accurate measurement of polarization states with very small ellipticity. This was the limiting factor in the measurements performed with the rotating analyzer ellipsometer used in Ottawa. The $PSC_{ROT}A$ configuration also provides the handedness of the elliptical states as well as the degree of depolarization caused by light scattering from inhomogeneities. With multichannel detection, the measurement speed is rapid, with a 50-point spectrum detected in ~20 ms.

Optical rotation, ellipticity, and degree of polarization of a linearly polarized light

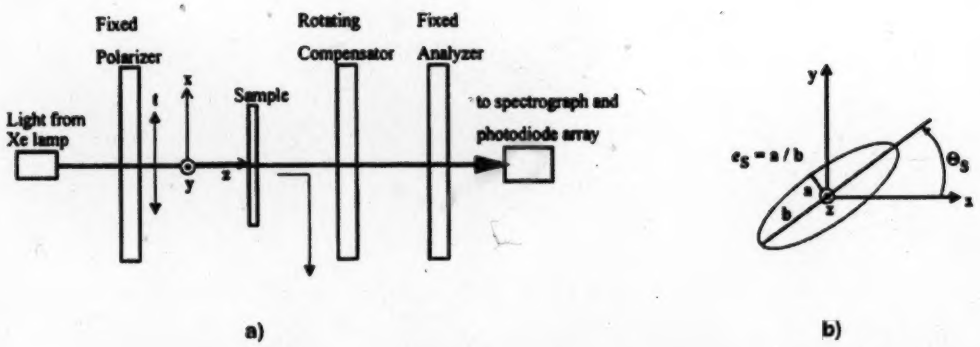

Figure 55: Schematic of the $PSC_{ROT}A$ transmission ellipsometer at Pennsylvania State University. In (a), t represents the transmission axis of the fixed axis, which defines the optical plane (parallel to the x-axis). In (b), the optical rotation (Θ_s) and the ellipticity (e_s) imposed by the chiral film are defined. *This figure is from Rovira et al. [105].*

---

wave upon transmission through a MgF_2 chiral GLAD film on glass are shown in Figure 56. The GLAD film was a 12 turn MgF_2 film, with a helical pitch of about 380 nm, deposited with a vapour incidence angle α = 85°. Based on microbalance mass measurements of similarly deposited films, we estimated the density as a percentage of bulk density to be about 40%. Effective medium theory [69] estimates the effective refractive index n_{avg} to be about 1.15, from the refractive index of bulk MgF_2 and the index of the air in the voids. From the measurements and calculations of pitch and effective index, the resonance region of the spectrum is expected to fall between 430 nm and 450 nm, which nicely brackets the observed features (430-450 nm) in Figure 56. The optical rotation spectrum and ellipticity compare qualitatively with the optical response of CLCs and isotropic chiral mediums with features similar to the molecular Cotton effect [58]. Quantitative comparisons with theory were not attempted due to limited experimental results and lack of detailed observations of the effects of orientation. The degree of polarization measurement shown in Figure 56c shows that the observed rotation and ellipticity represent nearly pure polarization states and that no significant depolarization has occurred, due to scattering from inhomogeneities, for example. These measurements confirm the chiral optical response of helical thin films and introduce chiral films fabricated with GLAD as a novel chiral material for theoretical and experimental investigation, and

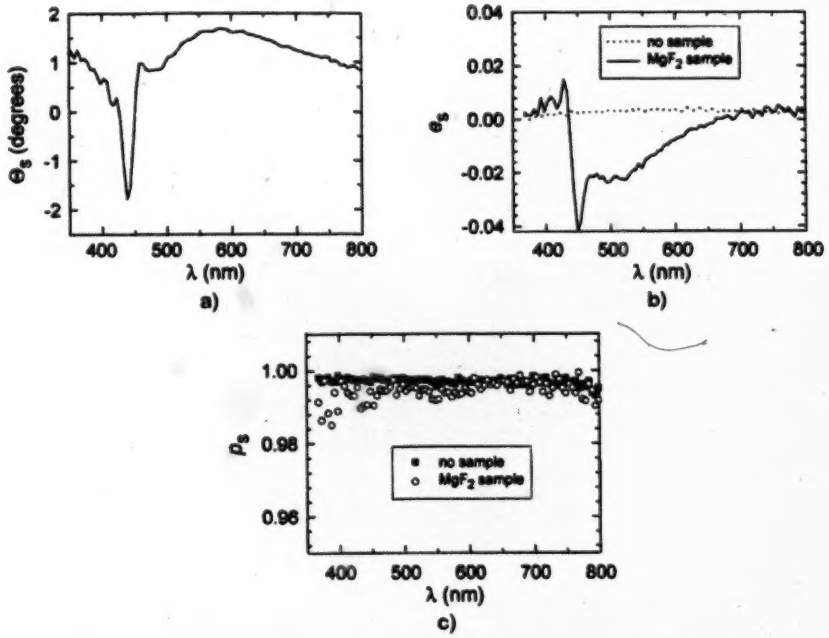

Figure 56: (a) Rotation angle Θ_s, (b) imposed ellipticity e_s, and (c) degree of polarization p_s measured by rotating compensator multichannel transmission ellipsometry for a 4.7 μm thick MgF_2 chiral film on glass. A linearly polarized light wave was incident on the film side of the film/ substrate system. Ellipticity and degree of polarization in the absence of the sample are also shown.

This figure is from Rovira et al. [105].

technological application.

5.1d) circular polarization effects

Light propagating in a chiral medium can be most simply understood by assuming circularly polarized modes of propagation. The linearly polarized light used as the probe in ellipsometry can be completely described as the sum of left and right circular polarization modes (LCP and RCP) of equal amplitude and opposite phase. Polarized light of any arbitrary polarization state can be described equivalently as either the sum of two linear or two circular polarized components, with independent amplitudes and phases. Optical rotation of linearly polarized light can be described as occurring when the two circular polarizations propagate at different velocities, arising from different effective refractive

indices [31,9]. The circular polarizations shift in phase relationship, and the resulting linear polarization is rotated. Non-zero ellipticity of the initially linearly polarized beam results when either of the right or left circularly polarized components are preferrentially absorbed or scattered. A logical technique to investigate chiral thin films is to probe the medium with circularly polarized light and measure transmittance and reflectance. The effect of the film chirality on the circular polarizations can then be examined separately.

To investigate circular polarization effects of chiral GLAD films, films were probed with circular polarized transmission spectroscopy at Philips, in Eindhoven, The Netherlands, by Dr. D. J. Broer and me. The spectrometer was equipped with optics (depolarizer, linear polarizer, quarter wave retarder, film/substrate, depolarizer, detector) to produce left and right circularly polarized light incident on the film. Films were helical MgF_2 GLAD films on glass substrates. Right and left circular polarized transmission through the film and substrate is shown in Figure 57b ('film'), as measured, and does not account for interface reflections or absorption in the glass. Clearly, transmission is dependent on wavelength, and on the handedness of the incident light. RHP is transmitted more than LHP, which is in accord with results from left handed CLCs (the film tested is left handed) where the LHP is constructively reflected from the chiral structure (circular Bragg reflection) [17]. This is the effect that gives the bright colour to many beetles, who secrete a CLC onto their shells. Reflected light from these shells has been observed to be circularly polarized. Figure 57c is the difference spectrum where the LHP transmission is subtracted from the RHP transmission to show the differential effect of the film on the two circular polarizations. The transmission difference has a peak at about 480 nm which corresponds, within experimental uncertainty, with the estimated peak of $\lambda = p^* n_{avg} = 420$ nm, where n_{avg} is an effective refractive index of the film which can be estimated as the density (60%) weighted sum of the index of the MgF_2 columns (n=1.38) and the index of the air in the voids (n=1.00). The slightly low prediction of peak wavelength might be a result of highly humid air (The Netherlands in June), or water absorption within the voids, both of which would tend to increase the effective index and shift the peak wavelength to higher values.

Both LHP and RHP light show significant reduction in transmission at shorter

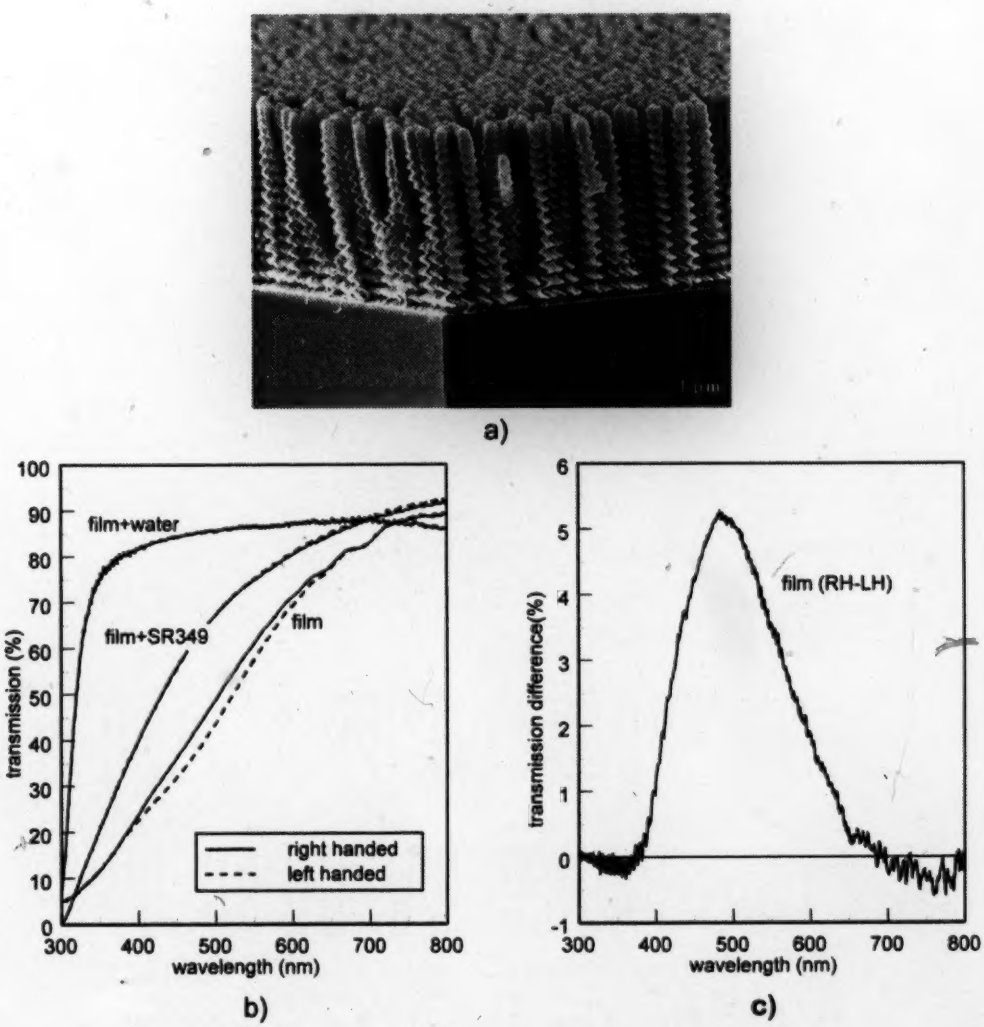

Figure 57: Left and right circular polarization transmission through the film shown in a). b) shows transmission through the as-deposited film (n=1.38), transmission through the film with the porous spaces filled with water (n=1.33) and with the spaces filled with an optically isotropic polymer SR349 (n=1.56). c) shows the difference spectrum with the RH transmission minus the LH transmission for the as-deposited film shown in a).

---

wavelengths (Figure 57b) which can be attributed to diffuse scattering from the porous structure of the GLAD film, and absorption in the glass substrate. For many applications

the scatter will be deleterious and may need to be eliminated or reduced. Filling the voids with a partially index matching material, or deposition of less porous films, may help to reduce scatter. In CLCs, Bragg reflection is highly specular [109], producing brightly coloured surfaces. Chiral GLAD films appear to the eye to be somewhat cloudy when the porosity is high. Discrimination between specular and diffuse preferential scattering of one circular polarization state was not attempted, but could be measured with bidirectional scatter distribution functions (BSDF) [109], or techniques similar to those described in [42,43]. While our transmission measurements do not conclusively demonstrate circular Bragg reflection (LHP preferential absorption could give similar results), comparison to CLCs suggest that Bragg reflection is a likely explanation.

The hypothesis so far has been that chiral optical effects in GLAD films arise from the difference in refractive index between the film material (MgF_2, n=1.38) and the air in the void regions (n=1.0). Other possibilities exist however, such as helical crystalline orientation, that could produce similar results. Logically, if index difference and shape are the origins of chiral optical properties, filling the void regions with a material that has a refractive index that matches that of the film should eliminate chiral optical effects. This was tested with water (n=1.33) and an optically isotropic polymer (ethoxylated bisphenol diacrylate - SR349, n=1.56, cured with UV exposure). The results are shown in Figure 57b

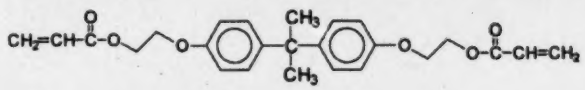

SR349

and as difference spectra in Figure 58. When the film was impregnated with water (n=1.33 - chosen to closely match the index of MgF_2 - n=1.38), almost all transmission difference was lost (Figure 58a). The difference spectrum shows some structure with differences less than 1%, but it is difficult to tell if there is any real difference or if the observed spectrum corresponds to imperfections in the spectrometer configuration. Water added to the film also allows us to observe the amount of light scatter arising from the porous structure. The difference between the water and film transmission spectra above 350 nm (Figure 57b) is attributed to diffuse scattering from inhomogeneities within the film. Absorption by the glass substrate used is strong for wavelengths less than 350 nm, causing the reduced

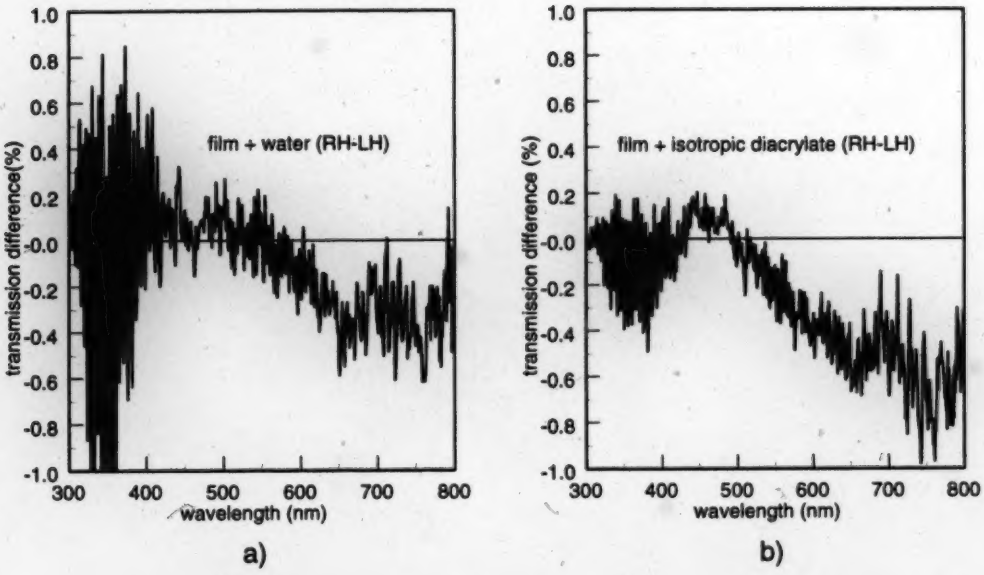

Figure 58: Difference spectra for the film shown in Figure 57a filled with index matching materials. The film is MgF_2 (n=1.38) and the matching materials are a) water (n=1.33) and b) ethoxylated bisphenol diacrylate - SR349 (n=1.56) cured with UV exposure.

transmission observed. The second impregnating material tested (SR349) is an optically isotropic polymer that has an index of n=1.56 after curing with UV exposure. The transmission spectra are shown in Figure 57b ('film+SR349'), and as a difference spectrum in Figure 58b. Similarly to the water impregnate, no difference between right and left handed transmission is seen. Also, transmission reduction from diffuse scatter is less than the film alone, but not as low as for water. This is attributed to the lack of good index-matching between the SR349 polymer and the film MgF_2. It is interesting to note that the film with the polymer impregnate SR349 shows little or no transmission difference. With fantasy, one might imagine a small maximum in transmission difference for both the water and polymer films near 450 nm (Figure 58), but the effect is minimal. Because there is a still a substantial difference between the film index (n=1.38) and the polymer index (n=1.56), one would expect that circular polarization effects should still exist to some extent when the pores are filled with the polymer. Limited experimental results preclude any detailed discussion of this, but a worthwhile experimental test would be to use an

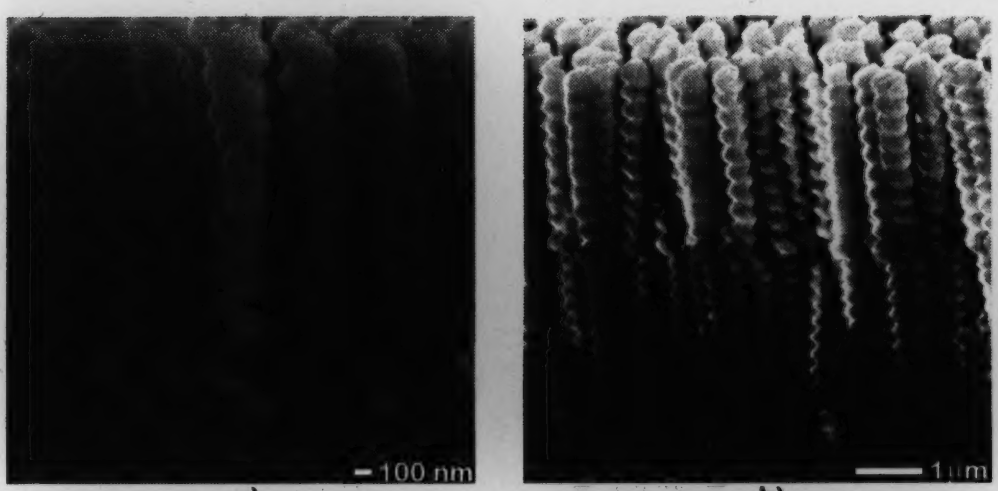

Figure 59: Graded pitch and right-left handed MgF_2 films. Chiral optical properties can be controlled through structural design with GLAD.

isotropic impregnate with an index lower than the GLAD film material. One possible explanation for the lack of circular polarization effects might be preferred propagation of the light waves in the higher index (in this case the polymer) material. Alternatively, the difference might be too small to measure with our experimental apparatus. Further investigation is clearly needed.

From the transmission spectra through the film with and without the optically isotropic impregnates, we conclude that the chiral optical response seen in the as-deposited film arises from scattering at the film/air interfaces of the helical shaped columns. As expected with this hypothesis, when the voids are filled with an index-matching material, the effects disappear.

Two interesting structures, shown in Figure 59, have been fabricated recently, but have not been optically tested. The pitch has been continuously varied from large to small to large again in Figure 59a, possibly resulting in broadened chiral optical response [15]. Adatom mobility increase due to heating is believed to have caused the observed blurring of the structure. In Figure 59b, a left-handed chiral layer was deposited atop a right-handed layer. The pitches of the two layers are slightly different. This film is expected to exhibit an optical response characterized by the superposition of left and right handed responses at

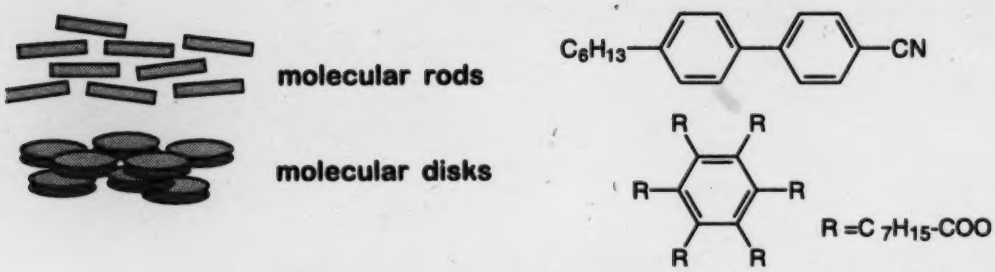

Figure 60: Rodlike (calamitic) and disklike (discotic) molecules form liquid crystalline phases.
Figure courtesy of Dr. D. J. Broer, Philips.

slightly different peak wavelengths.

5.2 Liquid Crystals

Liquid crystals (LCs) are materials that exhibit a material state between the liquid and solid states. They occur in melts and solutions of many organic materials, and have many of the characteristics commonly associated with a liquid (flow, viscosity etc.) yet also have positional and/or orientational order similar to solid crystals. They are typically long chain organic molecules with a backbone of rigid bonds forming rod (calamitic), or disc (discotic) shapes (Figure 60). In their simplest ordered state or phase (nematic), rodlike molecules align with strong orientational order yet little positional order. The molecules have a general average orientation (they all 'point' in the same direction - called the director), yet are free to move about like molecules in isotropic liquids (Figure 61). Other phases (smectic, chiral nematic) have varying degrees and types of positional and orientational order. Because of their ordered state, LCs exhibit optical, electrical and other physical properties usually seen only in solid crystals. The tailorable properties of these materials, combined with switching and control possibilities arising from their liquid characteristics, make them very useful for a large range of applications (including the liquid crystal display of the portable computer with which I am writing this sentence).

In bulk, liquid crystalline materials form structures very much like magnetic domains, with many small highly ordered regions separated by boundaries of disordered material. To induce long range order, external alignment mechanisms are used. The most

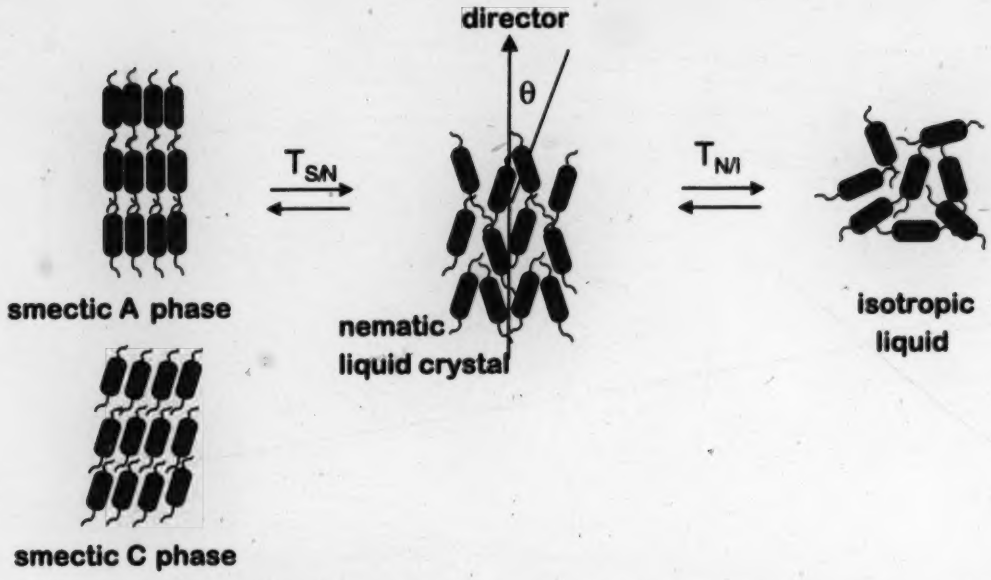

Figure 61: Liquid crystalline phases in thermotropic (change state with temperature) liquid crystals.
Figure courtesy of Dr. D. J. Broer, Philips.

common LC alignment techniques are surface treatments that allow control of the LC orientation at the interface between the alignment surface and the bulk LC. The structure in the bulk of the LC is affected by the alignment layer, but cannot be controlled directly. Because of the porous nature of GLAD films, their void regions can be filled with fluids, including liquid crystals. We have found that the form of the GLAD film directly controls the structure of the LC, in three dimensions, with the nanometer scale control obtainable with GLAD. This section discusses the investigation of impregnating GLAD films with various fluids, including isotropic liquids, optically isotropic polymers, and various anisotropic materials (liquid crystals). The work was performed in collaboration with Dr. D. J. Broer of Philips and the University of Eindhoven in The Netherlands. Films were fabricated at the University of Alberta, and investigation of impregnation was conducted in the Netherlands by myself and Dr. Broer.

5.2a) chiral nematic liquid crystals

Two type of LC alignments or phases will be discussed in this chapter: nematic, and chiral nematic. The nematic phase of LCs arises when rodlike molecules of the LC have

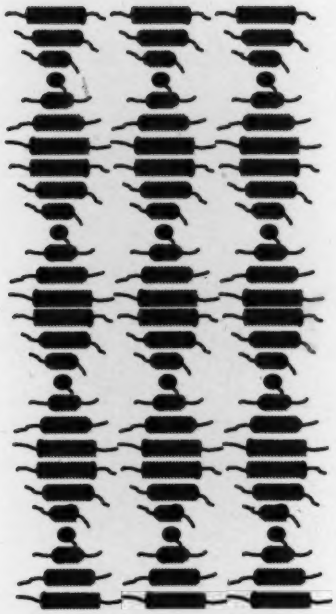

Figure 62: Chiral nematic or cholesteric LC phase.
Figure courtesy of Dr. D. J. Broer, Philips.

some degree of orientational order, but no positional order. The position of each molecule is essentially random, (like in most liquids), but they have a preferred average orientation or alignment in a direction called the director. If the molecules are birefringent or dichroic, this results in a net birefringence of dichroism of the LC domain. In the chiral nematic phase, the molecules are essentially rodlike, but with some asymmetry - they are chiral molecules. The chiral molecular structure causes the director to rotate in a helix through the thickness of the LC layer, with the helical axis perpendicular to the director of each layer of aligned molecules (Figure 62). Pitches of the director helix are typically of the order of the wavelengths of visible light, making many chiral nematic LC phases brightly coloured to the eye. The helical structure results in optical properties including optical rotation, circular birefringence, circular dichroism, and circular Bragg reflection. Because the pitch of the director helix is typically strongly dependent on temperature, chiral nematic liquid crystals (CLCs) can be used as thermochromic indicators with applications including implants in baby soothers to indicate fever, and the ever popular 'mood rings'.

5.2b) chiral optical devices

Chiral optical devices are used primarily for filtering of polarized light, for example in liquid crystal displays. Various optical switching techniques based on chiral liquid crystals (CLCs) have been envisaged, with optical properties superior to linear polarization based devices. In fact, twisted nematic cells, currently the state-of-the-art in LC displays, are one type of chiral optical device where the chiral 'twist' length is considerably longer than the wavelengths of visible light. The chiral optical devices discussed here have twists or pitches comparable to the wavelengths of visible light, and operate within the 'resonance' regime, corresponding to the 'zone of selective reflection' in the CLC literature [17]. Switching with a resonant chiral optical device is based on the phenomenon of circular Bragg reflection, where one of the left or right circularly polarized light components is selectively reflected by the helical structure in the chiral material. Circular Bragg reflection arises from constructive scattering of circular polarized light from helical structures, and is fundamentally very similar to constructive interference reflections of plane polarized light from high/low index multilayers (which can be fabricated with an alternate GLAD technique - See "Interference Optics" on page 113.). Circular Bragg reflection allows light to be polarized for switching (in display and other photonic applications) without the use of absorbing polarizers, such as those used in linear polarization devices, which reduce power efficiency by absorbing half of the light available for transmission through the device. A commercial display device based on CLCs was recently introduced onto the market by Kent Displays Inc. but is still considerably limited in capabilities. The major roadblock for realization of the benefits of chiral liquid crystal optical devices has been difficulty in creating sufficient long range alignment of the helical structure in a preferred orientation. Alignment attempts, to date, have used surface alignment layers on either side of the cell containing the liquid crystal to produce strong alignment at the surfaces. Two of the most common are 'rubbed' polymer layers [18,20] and obliquely deposited thin film layers [21,126]. Both types of alignment layers have an anisotropic microstructure that constrains the orientation of the liquid crystal molecules in contact with them, and allow specific liquid crystal architectures to be created. Recent techniques create surface anisotropy with photopolymerization of a polymer film with

linearly polarized light [19], or by construction of patterned self-assembled monolayers (SAMs) of anchoring molecules [39]. The alignment techniques can be compared to the practice of providing a seed crystal for epitaxial crystal growth of solids. One of the difficulties in achieving desired optical response designs is that orientation order is never perfect, and is usually short-ranged. If a LC layer is made too thick, orientation (and optical properties) will degrade. Recently, work to produce better long range order in LCs has produced polymer dispersed liquid crystals (PDLCs) [13,23,57,108] and liquid crystal gels where the liquid crystal is embedded in the pores of a cross-linked matrix. These techniques allow thick, stable, cells to be fabricated with small randomly oriented droplets of LC material, and are promising for diffuse scattering based optical switches and displays.

The most commonly used chiral optical material, chiral nematic liquid crystals (CLCs) [11,17], are composed of calamitic (rodlike) molecules with a small asymmetry in shape, or a mix of calamitic molecules with an asymmetric (chiral) additive. Within a range of temperatures or concentrations, the calamitic molecules form a phase very similar to the nematic LC phase where all the rods are oriented parallel to one another. The structure of a layer of these molecules in the chiral nematic phase can be described as being composed of many sheets, with all the rodlike molecules aligned within a sheet, but with a small rotation in orientation from one sheet to the next. The orientation (director) rotates in a helical fashion through the cell, with thickness for one full molecular rotation called the pitch, Ω. (Note: the first liquid crystals which displayed this orientation were closely associated with cholesterol and this phase was originally named the 'cholesteric' phase. The more accurate name for this phase is 'chiral nematic', however, and is the name that will be used here.) The polarization selection property of CLCs, circular Bragg reflection, occurs between $\lambda_1 = \Omega n_0$ and $\lambda_2 = \Omega n_e$ where n_o and n_e are the ordinary and extraordinary refractive indices of the locally uniaxial structure. Within this reflection band, right handed light is reflected from a right handed helix, and left handed light is transmitted. Alternatively, left handed light is reflected from a left handed helix, and right handed light is transmitted. Light with wavelength outside of the reflection band is transmitted in all polarizations. The width of the reflection band is on the order of 75 nm for typical materials

with $n_o \sim 1.5$ and $n_e \sim 1.7$. From [11], the reflectivity R as a function of wavelength, λ, is approximately:

$$R(\lambda) = \frac{k^4\delta^2 \sin^2(\beta L)}{4q_0^2\beta^2 + k^4\delta^2 \sin^2(\beta L)} \tag{10}$$

where

$$\beta^2 = k^2 + q_0^2 - k\sqrt{4q_0^2 + k^2\delta^2} \quad , \quad k = \frac{\pi(n_o + n_e)}{\lambda} \quad , \quad \delta \cong \frac{n_e^2 - n_o^2}{n_e^2 + n_o^2} \quad , \quad q_0 = \frac{2\pi}{\Omega} . \tag{11}$$

The peak theoretical reflectivity can be very high for thicker layers of CLCs; up to R~99.988% (a contrast ratio of 40 dB) for a 5 μm thick layer, and $R \sim 99.999998\%$ (a contrast ratio of 80 dB) for a 10 μm thick layer of a typical CLC material with $n_o \sim 1.5$ and $n_e \sim 1.7$. For thinner, or less than ideally aligned layers, the observed reflectivity can be considerably less [109]. CLC filters with extinctions of over 35 dB have been demonstrated to date. Obviously, thickness has a very strong effect on polarization contrast (40 dB to 80 dB by doubling the thickness). Previously, this advantage has been difficult to realize because of loss of alignment with thicker layers of CLCs.

5.2c) chiral GLAD/LC hybrid materials

In this section, I demonstrate a technique where the liquid crystal material is embedded in an inorganic porous backbone structure (a film fabricated with GLAD) to produce strong control of the molecular architecture of the LC, in three dimensions. Cell thickness should be limited only by difficulties in fabrication of thick films, with 10s of μm thicknesses conceivably obtainable. In addition, liquid crystal alignment structures can be designed to engineer desired optical responses. For example, the narrow bandwidth of transmission/reflection typical of a CLC cell can be increased by producing a structure with a pitch gradient. Previously, one way of accomplishing this was by crosslinking reactive CLCs by photopolymerization with a diffusion controlled concentration gradient [15]. This technique, while useful for passive optical component fabrication, solidifies the structure and doesn't allow for switching. With GLAD, the LC molecules are only loosely bound to the surface of the GLAD columns, and should be switchable with electric or magnetic fields, as is done in conventional liquid crystal displays. And, pitch gradients or other

structures can be accomplished with simple software modification to the deposition control system. Finally, because of the versatility of GLAD, fabrication of all polarization components needed for a switching cell might be accomplished with a small number of deposition steps, all based on GLAD, to produce a complete device. While many particulars still remain to be investigated, GLAD appears to be a promising technique for creating liquid crystal devices for display applications.

Porous films with a structure composed of helical shaped columns of MgF_2 were fabricated with GLAD (See "Glancing Angle Deposition" on page 24.). Alone, the helical films fabricated with GLAD are chiral, as discussed through optical activity measurements in "Chiral GLAD Films" on page 82. They exhibit optical rotation and circular dichroism as would be predicted from comparisons to other chiral systems, including isotropic chiral mediums, such as solutions of chiral molecules [9], and CLCs [17]. Limited optical anisotropy and the lack of a switching mechanism limit their use in display applications. It may, however, be possible that chiral films without LC additives could be used as circular polarizer layers in a display application based on the switching properties of hybrid chiral film/LC systems.

To investigate the optical response of chiral films impregnated with LCs, circular polarized transmission spectroscopy was performed. An ultraviolet-visible spectrometer was configured with the optical path comprising: light source, depolarizer, linear polarizer, quarter-wave retarder oriented at +/- 45° to the linear polarization, sample oriented film side toward light source, depolarizer, and detector. Transmittance was measured for each sample for both right and left circular polarizations by changing the orientation of the quarter-wave retarder from + to - 45° relative to the orientation of the linear polarizer. The porous chiral film was impregnated with various materials including: water, optically isotropic polymer, reactive and non-reactive nematic LCs, and a chiral-nematic LC. To impregnate the film, the sample was covered with a thin glass slide held in place with small pieces of tape at two edges. A small drop of the impregnating material was placed at one of the open edges and rapidly filled the porous film, as observed by a change in light scattering.

Two films impregnated with various materials will be discussed here. The films are

very similar, as both films were deposited with vapour incidence angle set to about $\alpha = 85°$, resulting in comparable porosity. The first is shown in the SEM micrograph of Figure 57a. It is composed of helical columns of MgF_2 with a helical pitch of about 350 nm and about 15 turns. Difficulty in absolute calibration of length measurements with a scanning electron microscope limits the accuracy of the pitch measurement to about 10%. The density of similar films was measured with a microbalance mass measurement technique [94] (See "variation of vapour incidence angle" on page 27.) and found to be about 60% of bulk density. Again, the accuracy of this measurement is limited as only similar samples were measured, and the density varies strongly with the vapour incidence angle α which cannot be set to great accuracy with the current deposition configuration. Work is ongoing to improve the repeatability of the chiral films deposited with GLAD. The second film discussed is almost identical to the first, with a slightly larger pitch.

Circular polarized transmission spectroscopy was conducted on the as-deposited film, and on the film after impregnation with isotropic fluids: water and a photopolymerized polymer. These results are discussed in detail in "circular polarization effects" on page 95.

When optically anisotropic impregnates such as liquid crystals are used, there is a remarkable effect. The film shown in Figure 2a was filled with the LC diacrylate C3M,

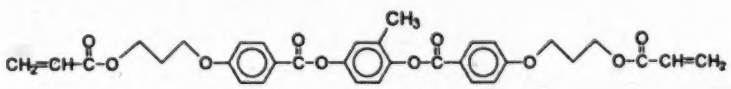

C3M

polymerized at 80 °C, and the non-reactive LC blend ZLI4792 (Merck). After polymerization the C3M polymer network has $n_o = 1.5488$ and $n_e = 1.6880$. The ZLI4792 blend has $n_o = 1.479$ and $n_e = 1.573$. The second film mentioned above, with slightly larger pitch, was impregnated with the non-reactive nematic E7 (Merck) with $n_o = 1.5$ and $n_e = 1.7$. All three of these materials usually exhibit nematic phases at room temperature, and as such, have no differential effect on circularly polarized light. The difference spectra for the ZLI4792 and C3M materials impregnated into the film shown in Figure 57a are shown in Figure 63, and in this case, are normalized to the measured right handed transmission to eliminate diffuse scatter contributions. Absolute transmission was

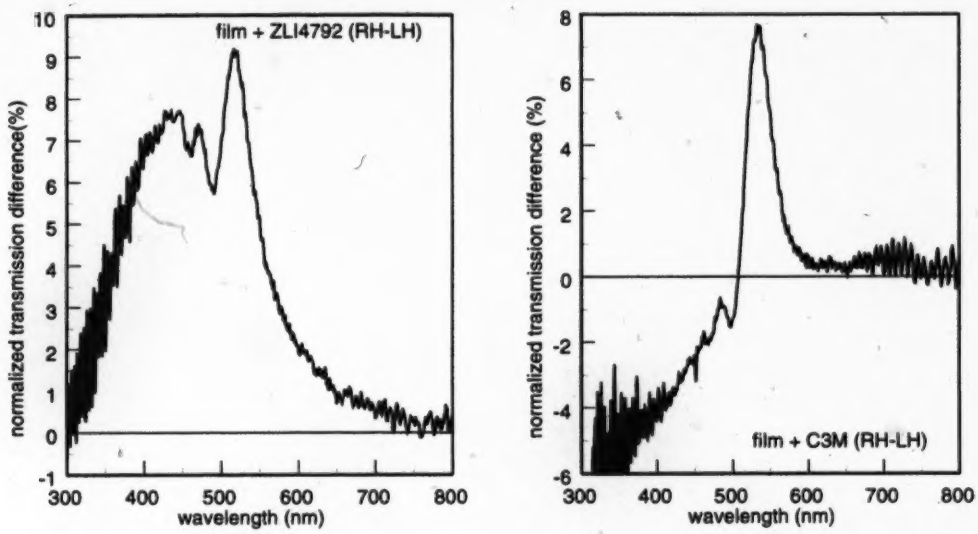

Figure 63: Difference spectra for the film shown in Figure 57a impregnated with a) ZLI4792, and b) C3M.

comparable to that observed for the film impregnated with SR249 (shown in Figure 57b) with the ZLI4792 impregnate exhibiting somewhat higher transmission and the C3M exhibiting somewhat lower. If the LC impregnates are induced into a chiral nematic order by the helical structure of the GLAD films, the circular Bragg reflection will have a maximum at $\lambda = \Omega n_{avg}$, where n_{avg} is a suitably averaged effective refractive index of the medium. Taking a simple mixing rule of the density weighted sum of the index of MgF2 and the average index of the LCs ($\lambda_{C3M} = \Omega n_{avg} = 520$ nm), the maxima should occur at about 520 nm for C3M and at 500 nm for ZLI4792. Measured transmission difference maxima are within experimental error, indicating that GLAD films do indeed induce chiral nematic order in simple nematic LCs.

Absolute transmission and normalized transmission difference through the second film impregnated with the nematic E7 is shown in Figure 64. Here, the observed transmission difference is much stronger than that observed with the C3M and ZLI4792 impregnates. Again, the maxima occurs, within experimental error, at the predicted wavelength, based on an assumption of chiral nematic order of the LC within the GLAD

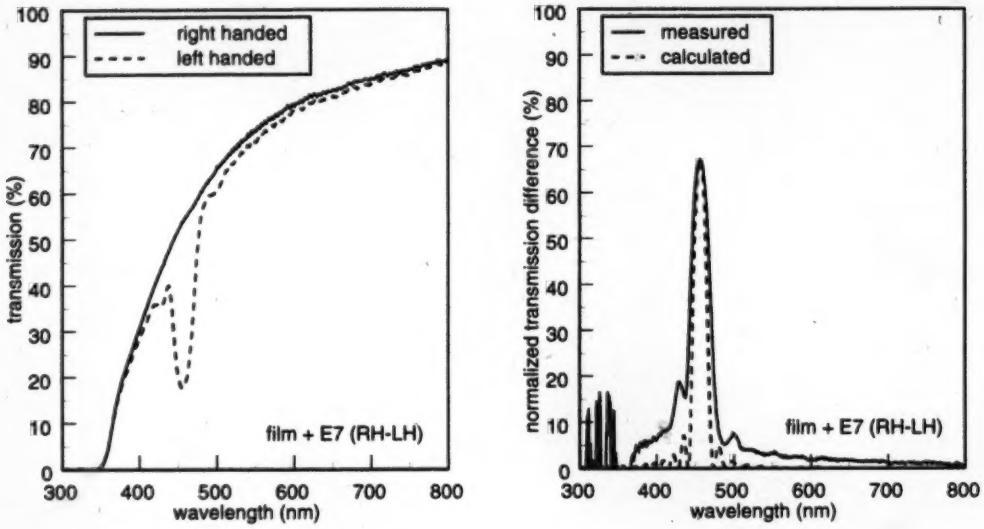

Figure 64: Absolute (a) and difference (b) transmission spectra for a film similar to that shown in Figure 57a impregnated with E7 liquid crystal.

film. Figure 64b shows a calculated curve from equation (10), where the transmission difference peak magnitude and wavelength have been chosen to match the measured spectrum. In matching the measured curve, an average index of n_{avg}=1.4275 and an anisotropy δ=0.0245 were used. From the simple mixing rule described above, an average index of n_{avg}=1.47 can be calculated, within experimental error. This optical anisotropy is much less than that of E7 alone (δ~0.12). Given the complex mix of film anisotropy and LC anisotropy, it is difficult to calculate the anisotropy for the composite material, and was not attempted here.

The film impregnated with the E7 LC is seen to have substantially stronger Bragg reflection than the film impregnated with the other LCs. One possible explanation is the difference in surface anchoring between the different types of LCs. Some aspects of surface anchoring effects are described in [126]. While the two LCs which exhibited weak alignment (C3M and ZLI4792) have fairly uniform electron densities, the E7 molecules have a cyano group (-CN) at one end of the molecule, which provides the possibility of chemical bonding to the GLAD film. If this is the case, the E7 LC molecules will align

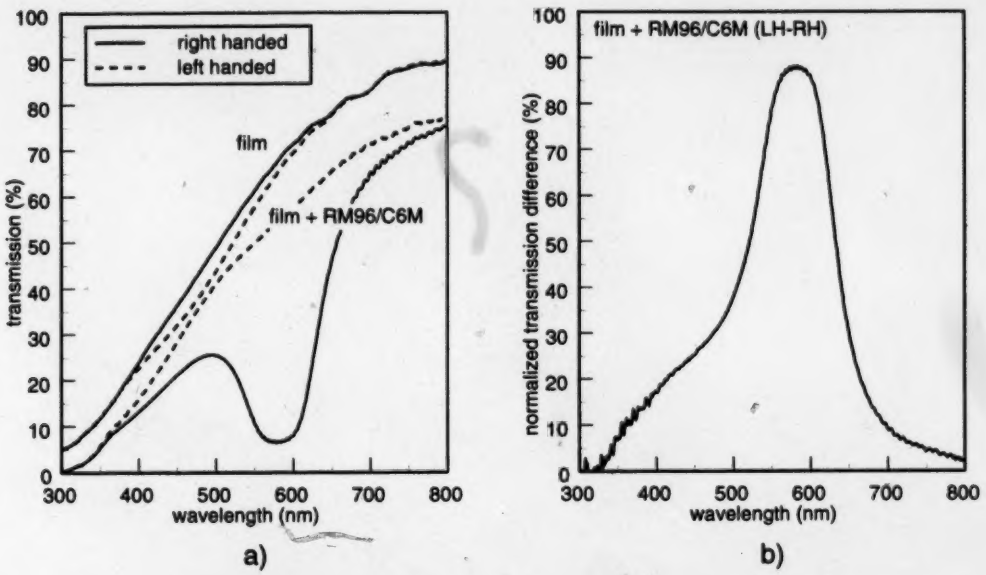

Figure 65: Transmission and difference spectra for the film of Figure 57a impregnated with a LC which usually exhibits a right-handed chiral nematic phase.

homeotropically (perpendicular to the surface) along the helical GLAD columns. The other two LC molecules, we hypothesize, are aligned homogeneously (parallel to the surface) along the GLAD columns. The homeotropic bonding appears to result in a stronger overall alignment of the LC within the voids, resulting in stronger Bragg reflection effects. Testing of switching voltages and temperatures or variation of film and LC materials will help to clarify bonding effects.

5.2d) chiral nematic impregnates

Finally, a LC material, which exhibits a chiral nematic phase at room temperature, was used to impregnated the film of Figure 57a. The handedness of the CLC phase of the LC material was chosen to be right handed while the film was left handed. Absolute transmission and transmission difference spectra are shown in Figure 65. We see from the spectrum that the Bragg reflection is dominated by a right handed reflection from the CLC and that the left handed film has little or no effect of creating a left handed alignment of the CLC. Surface anchoring, again, could help to explain this result, and with appropriate choices of film and LC material, effects of competition between left and right handed

alignment tendencies might be observed. The broadness and asymmetry of the peak in the difference spectrum (Figure 65b) may be a result of influence of the film structure on LC alignment.

In this section, I have demonstrated chiral nematic alignment of liquid crystal materials inside the porous voids of an inorganic structure of MgF_2. Nematic liquid crystal materials impregnating the porous voids within the inorganic structure fabricated with GLAD, composed of helical shaped columns of MgF_2, were induced to form a phase very similar to the chiral nematic phase seen in other liquid crystal materials. This was demonstrated with measurements of transmission through the film with right and left circularly polarized light. Circular polarization selective reflection from the helical structure of the chirally oriented liquid crystal results in differential transmission, in good agreement with theoretical predictions. GLAD materials are thus a promising new technology for the alignment of liquid crystals, suggesting use in display and other photonic switching applications.

6. Interference Optics

Thin film interference filters are usually fabricated with two or three materials deposited in a multilayered stack. The materials have different refractive indices, and are used to create a designed refractive index profile. Spectral response is engineered by specifying a refractive index profile to provide the desired filtering characteristics. Thin film interference filters require apparatus with complicated control systems to vary the material, and refractive index, deposited [38].

Interference filters can be fabricated with GLAD, from a single material, by varying the film porosity, and hence the effective refractive index as a function of film thickness [101]. Layers are produced by alternating dense (high refractive index) and porous (low refractive index) microstructures of a single evaporated film material. In plane inhomogeneity and anisotropy can be eliminated with rapid substrate motion, producing a periodically inhomogeneous, uniaxial, medium with the axis of symmetry perpendicular to the film surface. Alternatively, anisotropic effects can be exploited to produce polarization sensitive filters [78]. Complex refractive index profiles can be created by controlling the film porosity through variation of the vapour incidence angle α (See "Growth Mechanics" on page 25.). The wide range of densities obtainable with GLAD films [97] (See "variation of vapour incidence angle" on page 27.) allows complex index profile designs to be realized, resulting in great latitude in filter design. Highly porous layers are also low in stress which allows thicker films to be fabricated than would be possible with standard thin film filter fabrication techniques [106]. Finally, diffusion of gases, and other fluids, into the porous regions, or absorption of chemical or biological species onto the large surface area inside the optical filters, will alter the optical response, enabling a new type of optical sensor technology [70,103] (See "chemical sensors" on page 63.).

6.1 GLAD interference filters

Because GLAD films are partially porous, with a structure size on the order of the wavelengths of visible light, they can be used as tunable refractive index materials [44]. The effective refractive index of the porous GLAD material is between that of the film material and the air which fills the voids, and is approximately equal to a density weighted

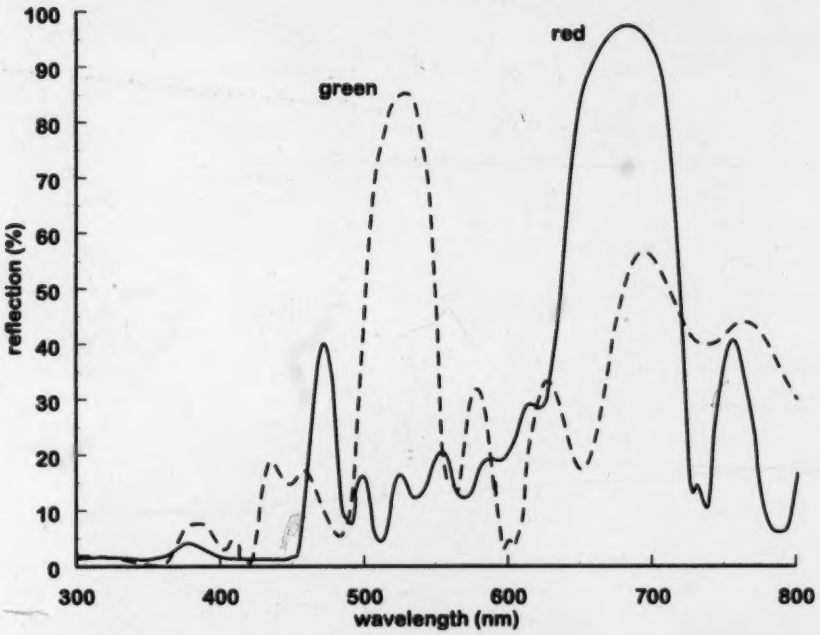

Figure 66: Reflection spectra of two interference filters fabricated with GLAD. The 'red' spectrum was obtained from the film in Figure 16 (page 32). The 'green' spectrum was obtained from similar film with a slightly smaller spacing between the porous layers.

---

sum of the indices. Effective medium theories [69,128] examine the optical response of composite mediums such as these, and could be used to derive more accurate predictions. Refractive index can be tuned by varying the porosity of the film through control of the vapour incidence angle α (See "Growth Mechanics" on page 25.). With intelligent design of substrate motion during deposition, multilayer interference optical components can be fabricated in a single deposition.

The two spectra shown in Figure 66 are from the first two interference filters fabricated with GLAD. They were fabricated with a sinusoidally varying vapour incidence angle α, with a half rotation (ϕ) of the substrate per period of α variation. The exact motion of the substrate and the film structure are shown in Figure 16 (page 32). Imperfections in the motion control produced a somewhat imperfect structure for an interference filter with some aperiodicity in the index variation. This resulted in the complicated reflection spectra

shown in Figure 66.

The fabrication of a simple interference filter with GLAD by fairly simple substrate motion suggests a wide range of possibilities in optical filter design. Because index can be varied continuously by choosing the vapour incidence angle α, complex filter designs could be easily realized. Anti-reflection, bandpass, notch, and other filter designs can be fabricated by designing the desired transmission or reflection spectrum, and choosing an index variation design for fabrication with GLAD. With calibration of density and index as functions of vapour incidence angle α, it should be possible to generate any desired index variation.

One possible limitation of GLAD interference filters, not investigated in detail in this thesis, is scattering from the porous structure or 'haze'. Because the structures fabricated with GLAD are not substantially smaller than the wavelengths of light, some light scattering will occur at irregular interfaces within the film. It should be possible to reduce this effect through careful fabrication with the intention of reducing structure sizes, but 'haze' may be a significant problem with GLAD interference filters. The filters shown in Figure 66 were slightly cloudy to the eye because of light scattering, whereas the filter in Figure 67 was substantially more transparent. The SEM micrographs of these films show that the porous structure of the latter film was significantly smaller than the former. Upon examination by eye, of the scattered light from a bright beam of white light passing through the film, the filter in Figure 67 exhibited similar haze as a commercial narrowband multilayer filter fabricated with SiO_2 and TiO_2. Investigations of haze and scatter characteristics of obliquely deposited films are discussed in [42,43].

Another possible effect that should occur with interference filters fabricated with GLAD is modified optical response when the pores of the film are filled with something other than air. Humidity is known to cause significant effects in porous films, and may cause stability problems for filters fabricated with GLAD [45,123]. On the other hand, sensitive chemical filters may be possible which exploit this effect. If a film were fabricated with a material that has a reaction with a target chemical, varying optical response could give a measurement of concentration [70]. Methods exploiting any change in the optical properties discussed in this chapter could be used for chemical detection. The capacitance

based humidity sensor discussed previously could be constructed as an optical detector with minor design modifications (See "chemical sensors" on page 63.).

6.2 Rugate Filters[i]

Rugate filters are optical interference filters that consist of sinusoidal index variations described by:

$$n(x) = n_{avg} + \frac{\Delta n}{2} \cdot \sin\left(\frac{2\pi x}{\Lambda}\right) \tag{12}$$

where Δn is the peak-to-peak index variation, n_{avg} is the average refractive index variation, and $\Lambda=\lambda_0/(2n_{avg})$ is the physical thickness of one period. The bandwidth, BW (approximately FWHM), and reflectance, R, of the reflection peak for small index variations are given by [114]:

$$\log(1-R) = -0.6822 \cdot \frac{\Delta n}{n_{avg}} N + \log\left(\frac{4n_0}{n_s}\right) \tag{13}$$

$$BW = \frac{\Delta n}{2n_{avg}} \tag{14}$$

where n_o is the index of the incident medium (air for our reflectance measurements), n_s in the index of the substrate and N is the number of periods. The above equations give fast estimates of the bandwidth and reflectance. However, to obtain accurate reflection spectra, the characteristic matrix method (CMM) [12] was used in a theoretical analysis conducted by A. J. P. Hnatiw [101]. Since the equations for bandwidth BW and reflectance R are only approximate when the index variations are large, there is some difference between the theoretical predictions above and those calculated by the CMM.

To improve the quality of filters fabricated with GLAD, the deposition apparatus was improved to allow more accurate control of substrate motion (See "Equipment Development" on page 49.). An improved film interference filter was constructed with much better sinusoidal index variation (rugate filter) and is shown in Figure 67. I formed a collaboration with photonics researchers A. J. P. Hnatiw, Dr. R. I. MacDonald and

i. A portion of this section has been published in [101] K. Robbie et al., Electron. Lett. 33 (14) (1997), 1213-1214. Copyright The Institution of Electrical Engineers 1997.

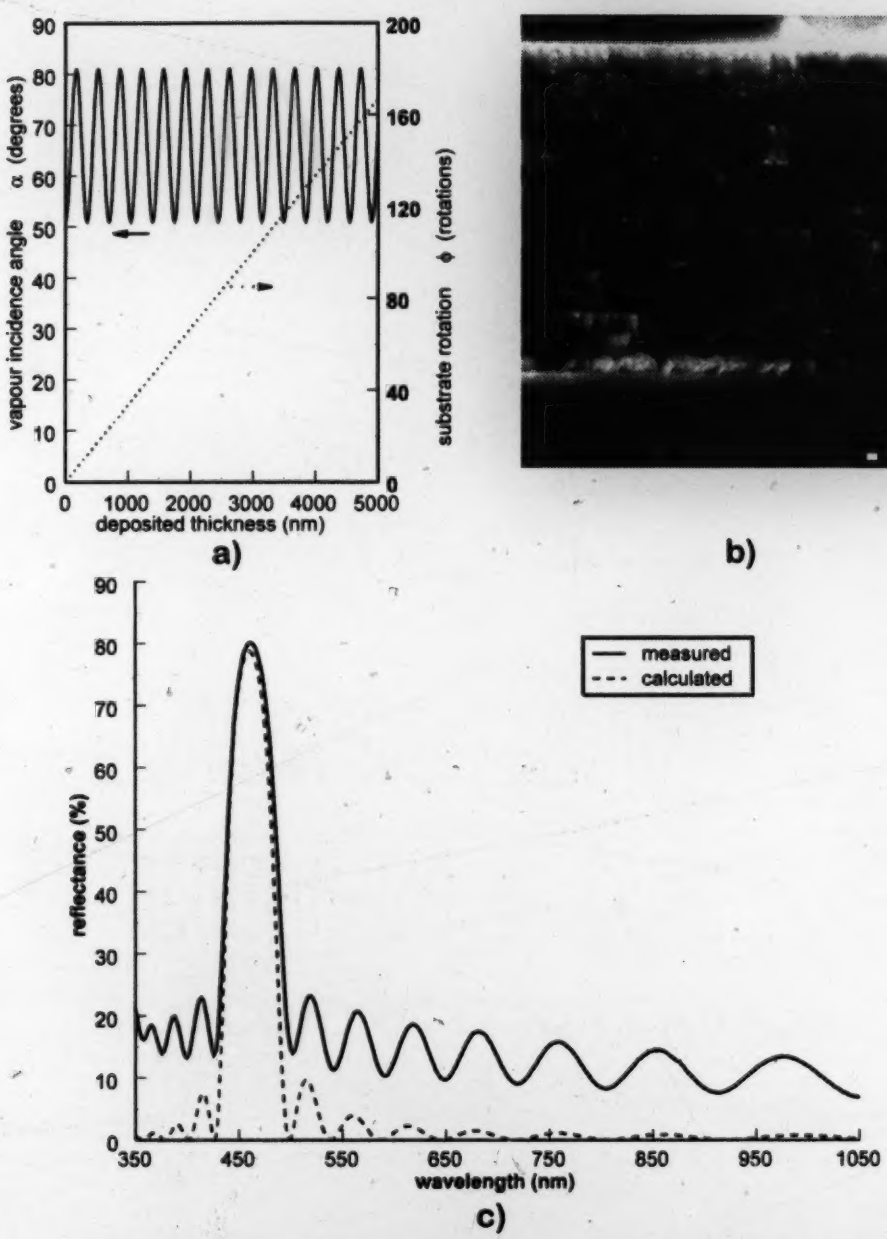

Figure 67: High quality interference (rugate) filter with periodic index variation. a) The vapour incidence angle α was varied sinusoidally while the substrate was rapidly rotated, ϕ. b) Film structure exhibits periodic stratified layers of alternating dense and porous material. c) Theoretical and measured reflection spectra. Bandwidth $BW = 50$ nm. Reflectance $R = 82\%$.

Dr. J. N. McMullin where they would investigate filter designs and modeling while I fabricated and tested filters. Figure 67c shows the first measured and calculated spectra for the simple rugate film shown in Figure 67a. The film is MgF_2, and was generated by varying the vapour incidence angle α sinusoidally between 51° and 81° during the deposition. The substrate rotation ϕ was rapid throughout, generating a vertical porous columnar structure (posts), eliminating any helical columnar structure (some periodic stratification can be seen at high magnification with a vertical period of about 20 nm).

In [94] I discuss measurements of density and effective refractive index of films fabricated with GLAD, where a simple density weighted sum of the index of the film material and the index of air was found to predict the effective refractive index as measured by a prism coupler. Based on similar measurements, the density of the MgF_2 was estimated to vary between approximately 90% and 30% of bulk when deposited at α=51° and α=81° respectively. From these estimates, the refractive index range in the film was estimated to be between 1.11 and 1.34 (n_{avg} = 1.22, Δn = 0.23). The thickness of the film was measured with the SEM to be approximately 2.6 μm, corresponding to N = 14.5 periods and Λ = 180nm. A thickness of 2.6 μm is large for thermally evaporated MgF_2, which typically fractures from intrinsic stress when deposited thicker than about 1 μm, lending support to the assumption that these films have low intrinsic stress. Using the data from above, the theoretical reflection spectrum was calculated, by A. J. P. Hnatiw, using the characteristic matrix method implemented in FORTRAN. The measured and theoretical reflection spectra are shown in Figure 67c [101]. Fitting the CMM model to the measured spectrum, using the known film thickness and estimates of the density variation, we found the index variation to be between 1.13 to 1.31 (n_{avg} = 1.22, Δn = 0.18), in good agreement with the estimates from the film density variation. The measured peak reflectance is R = 82%, and the bandwidth is BW = 50 nm, centered at 460 nm. Using the above equations we obtain BW = 34 nm and R = 92% which demonstrates the inaccuracy of these formulas for large index variations. While these formulas can be useful for fast calculations, accurate results require a more powerful method, such as the CMM. Since the effect of intrinsic stress is low in these films, we anticipate that very thick filters with correspondingly narrow passbands can be grown. Such filters are of current interest for wavelength division

multiplexing applications in optical communication systems. Other filters with designed spectral response should be possible with this technique allowing fabrication for a wide range of applications.

7. Squeezing

It is a natural question to ask if the layers of helical 'springs' can be squeezed, or compressed. Do springs fabricated on a nanometer scale respond similarly to macroscopic springs? Obviously the films will be somewhat compressible, with a possible limit being the compressibility of the bulk material. I have attempted to 'squeeze' sets of GLAD springs with electrostatic attraction between charged electrodes sandwiching the springs. The physics of macroscale springs was used to estimate the spring constant, and predicted observable motion. An analysis performed with M. Seto, based on macroscale springs, was used to design spring geometries for fabrication with GLAD, in hope of demonstrating squeezing. Unfortunately, difficulties in fabricating capping layers on very porous films (discussed in "Capping" on page 54) have made it difficult to fabricate optimal geometries. Using available spring/electrode structures, I was unable to measure any deflection of the top electrode when a 16 V (peak to peak) low frequency (kHz) voltage was applied across the structure. Working with G. Steeves and M. R. Freeman of the Physics department of the University of Alberta, I modified an existing fibre interferometer to achieve motion detection limits of about 10 picometers (pm). However, an analysis based on macroscopic springs predicts motion on the order of the detection limit for the structures tested. Structures with higher porosity and with larger pitches are expected to show substantially more motion. The force provided by electrostatic attraction is quite weak in the geometry tested, and other methods for deflection were considered. An acoustic transducer, for example, should produce more deflection, and even a direct mechanical force, such as from an indenter or probe microscope, could easily provide more squeezing force. Unfortunately, most methods were either unavailable or would not allow the absolute observation that an interferometer measurement gives. I chose electrostatic deflection and interferometric detection as a source of an absolute demonstration method; this should not be thought to limit the possible application of squeezed GLAD films with other actuation methods.

In this short chapter, I will discuss calculations of the properties of springs, based on their structure, leading to guidelines for a structure to be fabricated with GLAD. I will discuss interferometry and the highly sensitive interferometer I helped construct. Finally, I

will discuss the measurements I have performed and the significance of the lack of observable motion to the detection limit of the interferometer.

7.1 Springs

The mechanical properties of helical or coil springs depend strongly on the geometry of the spring. Spring constant (deflection obtained for an applied force) and resonant frequency vary with the shape. Total theoretical compression of a macroscopic spring is given by [93]:

$$\frac{\Delta t}{F} = \frac{1}{k} = \frac{64R^3 n}{Gd^4} \cdot \left[1 - \frac{3d^2}{64R^2} + \frac{3+\nu}{2+2\nu} \cdot \tan^2\theta\right] \tag{15}$$

where Δt is the total shortening (m), F is the applied force (N), k is the spring constant (N/m), R is the coil radius (m), d is the wire diameter (m), n is the number of turns, G is the shear modulus (Pa), ν is Poisson's ratio, and θ is the rise angle of the spring (measured from the surface; $\theta = 90° - \alpha$). It is convenient to express the geometrical parameters as functions of the pitch, and the coil radius R can be related to the pitch Ω and the rise angle θ as:

$$R = \frac{\Omega}{2\pi\tan\theta}. \tag{16}$$

When a set of springs is arranged in parallel (as in the GLAD film layers), the spring constants of each spring add to give the overall spring constant of the structure. Electrostatic attraction between charged plates above and below the helical film allows a controllable force to be applied. A helical film similar to that shown in Figure 68 can be fabricated with helical columns of film material, with a dense cap, all sandwiched between conducting electrodes of Al. The force per unit area applied to the 'spring' film when a voltage is applied across the electrodes is:

$$F = \frac{\kappa\varepsilon_0 V^2}{h^2} \tag{17}$$

where F is the force (N/m^2), κ is the dielectric constant of the film, ε_0 is the permittivity constant (8.85×10^{-12} F/m), V is the applied voltage (V), and h is the separation of the electrodes (m).

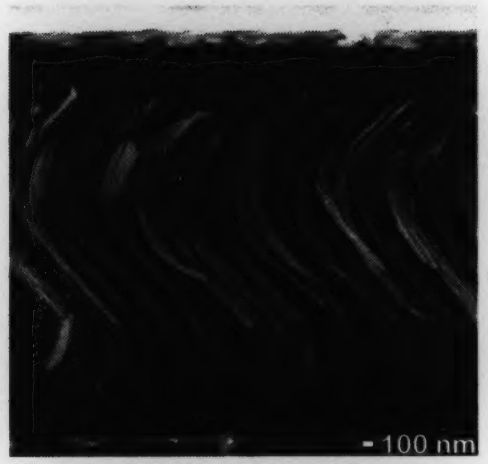

Figure 68: One turn helical film for squeezing. Aluminum electrodes are fabricated above and below the capped SiO film.

While it is somewhat difficult to get accurate measurements of the film parameters used in these equations, some general trends can be seen by assuming realistic values and varying others. One other parameter is needed to calculate the theoretical deflection of a helical film, the number of columns per unit area. I have chosen to express this as the average area occupied by each spring - a^2 (m^2). In Figure 69, the following parameters were used to calculate theoretical deflections:

$n = 1$, G = 30 GPa, $\nu = 0.3$, $\theta = 45°$, $\kappa = 5$, V = 10 V, $h = n\Omega$.

In Figure 69a, the wire diameter was kept fixed at d = 80 nm and the column spacing (porosity) was varied. The average area occupied by one helix (square a x a) was increased from fully dense ($a < d$ = 80 nm) to considerably porous (a = 200 nm). The maximum theoretical deflection is very small for small pitch (Ω small) or more dense (a small) structures. For the $\Omega \sim 2.5$ μm pitch film shown in Figure 68, the porosity must be high enough that $a > 150$ nm to get an expected motion of greater than 100 pm (1 angstrom). In Figure 69b, the porosity is kept constant (a = 100 nm), and the wire diameter d is varied. Small decreases in the wire diameter give substantial decreases in spring constant, and a resulting increase in maximum deflection. In a $\Omega \sim 2.5$ μm pitch film, if the wire diameter d can be decreased from 80 nm to 60 nm, the expected deflection more than triples. Unfortunately, fabrication of films with large pitches, small column diameters, and

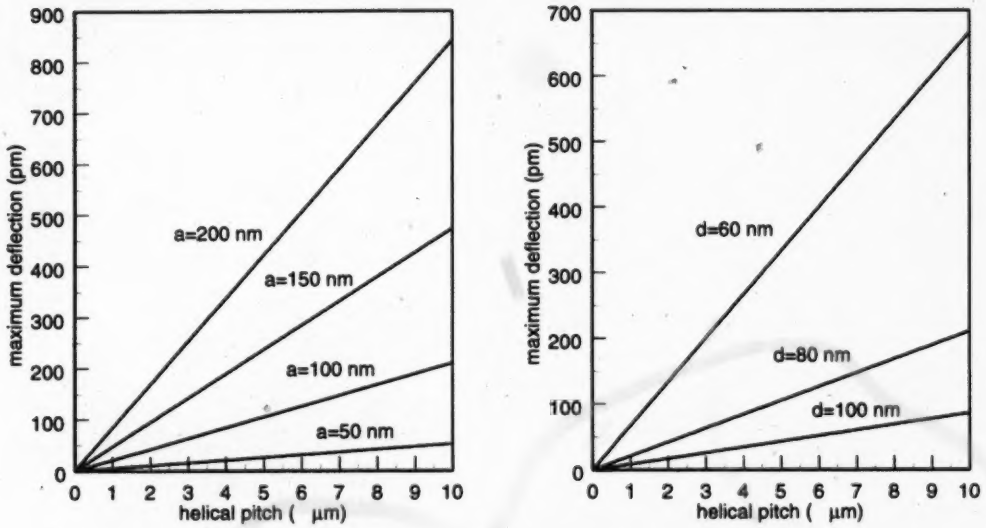

Figure 69: Theoretical deflection of helical springs. In a), the density of the film is varied (a is the average area occupied by one column), and in b), the diameter (d) of the 'wire' is varied.

adequately dense caps is quite difficult due to heating and fractal roughening effects (See "Growth Mechanics" on page 25.). Also, because of breakdown in the film or the pores, the voltage that can be applied is limited (at least with SiO films with air voids). When voltages greater than the breakdown are applied, electrical current punches through the film, possibly at defect sites, and creates substantial local heating. The film is destroyed, as is shown in Figure 70 where a crater into the Si wafer has been created through the Al top and bottom contacts, and the MgF_2 helical film.

7.2 Interferometry

Interferometry is a technique where the constructive and destructive interference of light is used to measure distance or displacement. The experiment employes two beams of light (usually a laser) which are separated with a partial mirror, and then recombined, after one beam reflects off of the object of interest. A screen or detector measures the recombined light, observing bright and dark fringes on a screen, or a sinusoidally varying intensity on a detector. The interference of the two beams allows very accurate

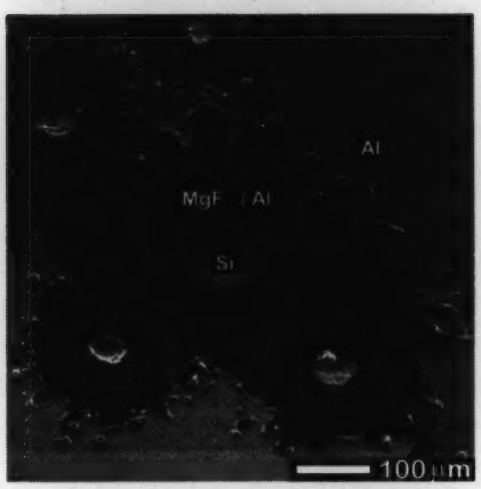

Figure 70: MgF_2 film destroyed by electrical breakdown while attempting squeezing. Energy dispersive x-ray analysis (EDX) was used with the SEM to characterize the material composition shown.

measurement of differences in the path lengths travelled. Recently, fibre optic interferometry has become the method of choice for measurements of deflection in planar geometries like the thin film springs investigated here. Electromechanical properties of helical polypeptides were investigated in [54] with an optical fibre interferometer with motion detection limits in the tenths of pm (~10^{-13} m). In a fibre interferometer (shown schematically in Figure 71), a glass optical fibre is placed close to the film (can be positioned to µms with a good quality screw positioner). Light from a laser is sent into the fibre, emerging from the fibre end above the film. Part of the light is reflected back into the fibre from the interface of the glass and the air. This is the first of the two interfering light beams. Part of the light that emerges from the fibre reflects off of the film, and re-enters the fibre. This is the second light beam. After passing through the fibre coupler, the reflections are detected with a photomultiplier. The path difference between the reflections is double the distance between the film surface and the fibre end. If the film moves, the signal in the photodetector varies sinusoidally, with a period of half of the wavelength of the laser light. By applying an AC voltage across the film, periodic deflection will occur at the applied frequency or harmonics. With a lock-in amplifier, this weak AC signal can be detected very accurately. Feedback stabilization with a piezoelectric positioner allows the interferometer

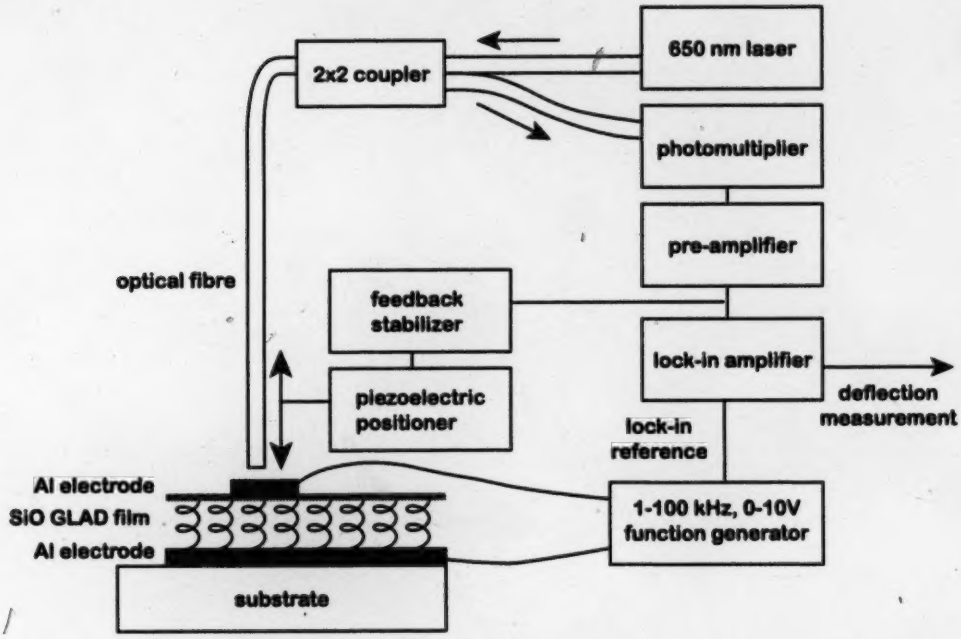

Figure 71: Fibre interferometer with AC detection. Based on a scanning tunnelling microscope electronics and control stage, detection limits are in the pm range.)

---

to be maintained at the maximum sensitivity portion of the detected sinusoid and allows high precision. With a test signal applied to the piezoelectric positioner (moving the fibre instead of the film), deflections of 100 pm were easily observable. When a voltage was applied across a variety of MgF_2 and SiO helical films between Al electrodes, no observable deflection was detected either at the applied frequency, or at double that frequency. Based on the theory of macroscopic springs, the best film geometry fabricated to date is shown in Figure 68. With the geometry of this film, the theoretical predicted film deflection is comparable to the interferometer detection limit. To observe squeezing of GLAD films, better geometries, or improved interferometry is required.

The lack of observable squeezing of a helical GLAD film with electrostatic actuation neither proves nor contradicts the hypothesis that they behave similarly to macroscopic springs. Because of inaccuracy in determining the film geometry, it is difficult to calculate accurate theoretical predictions of actuation.

8. Summary and Recommendations

8.1 Summary

This thesis describes a novel technique for creating structure in thin film materials, on a nanometre scale, and in three dimensions. Glancing angle deposition (GLAD) controls structure by exploiting a shadowing effect that occurs when deposition vapour arrives at an oblique angle onto the substrate. Computer-controlled substrate motion is used to shape the columnar film structure into desired shapes, including posts, helices, and others. The type of structural control enabled by GLAD leads to a new class of materials that appear particularly promising for use as new materials and devices for fields including optical, chemical, biological, mechanical, magnetic, and electrical. GLAD techniques are described in detail, from the most basic, to the current state-of-the-art, including an advanced technique which greatly expands the range of obtainable structures.

One type of GLAD material, a helical, or chiral, film was investigated with ellipsometry and circular polarized spectroscopy techniques, and the results are discussed, and compared to theoretical expectations. These helical films are the first engineered, inorganic, chiral medium for visible wavelength radiation. They exhibit an optical response very similarly to that of the technologically important chiral liquid crystalline materials, and may complement or replace liquid crystals in some applications for optical filtering or switching. The versatility of the GLAD technique should allow design of optical response characteristics not possible with liquid crystal materials. Also, while the studied materials exhibit purely dielectric responses, other chiral GLAD materials may exhibit more complicated effects.

The combination of GLAD films with liquid crystals also produces exciting results. When the voids in porous GLAD films are impregnated with liquid crystals, the molecular orientation of the liquid crystalline phase is controlled by the structure of the GLAD film. Chiral GLAD films induce chiral ordering of non-chiral liquid crystal materials. Optical display and switching applications may be possible with this technique, as it controls structures in liquid crystals while still allowing for switching of the liquid crystal.

Novel interference filters were fabricated with GLAD by creating a periodic density

variation in order to control refractive index. A refractive index profile can be designed to produce a desired spectral response of the filter. The outlook for applications of these filters in optical communications and sensing fields is encouraging.

Finally, electrostatic 'squeezing' of a helical GLAD film sandwiched between conductive electrodes is discussed. An interferometer with detection limits in the tens of picometers was developed to measure movement of the top electrode when an electric field was applied across the structure. No motion was observed with the films tested, but theoretical analysis predicts deflections on the order of the detection limit. Film structures with improved geometry, with larger pitches and higher porosities, are expected to display observable motion.

The GLAD technique is described in detail in the thesis, including equipment and control issues, and example of realized film structures. Descriptions of investigations of chiral optics, liquid crystal hybrids, interference optics, squeezing, and other areas should provide a firm foundation for future researchers interested in investigating GLAD techniques and materials.

8.2 Recommendations

Given the broad range of possible applications of GLAD, it has been difficult to decide on which areas to concentrate research efforts. The research described in this thesis included investigations of many ideas, either with literature evaluations alone, or combined with experimental studies. Application areas where investigative films were fabricated are discussed in "Applications" on page 58. In this section I would like to describe what I believe to be the most promising areas for GLAD application and study. Application and fundamental physics studies are both important, and I will describe aspects of each.

First, I think that the promise of GLAD films for optical applications is clear. Detailed initial investigations of chiral and interference optics were presented in this thesis, and the possibilities for future development are encouraging. Liquid crystal optical applications are also exciting, with demonstration of a switching cell the logical next step for hybrid GLAD/liquid crystal materials. If useful switching characteristics are observed, display and other switching applications will be possible.

As chemical sensors, I believe that GLAD films have great promise. Simple humidity sensors fabricated with GLAD display good response, and minor design changes should allow for selective chemical sensing. Catalytic applications may be possible with GLAD, but numerous issues must be resolved before this use is confirmed. A measurement of effective surface area would help to clarify GLAD usefulness in this area.

Magnetic material fabrication with GLAD appears, to me, to be slightly less promising than optical material fabrication. While it is known that magnetic properties are affected by oblique deposition, it is not completely clear what effect GLAD will have. Magnetic film control may be possible, but many basic effects must be investigated before GLAD use is possible.

Actuation of GLAD films, 'squeezing', appears to be more difficult, and perhaps less useful, than was originally thought. Small deflections, from difficult to manufacture films, could limit the usefulness of this effect. It may be interesting, however, to compare the elastic properties of nanoscale springs to macroscale springs. Finite size effects may be strong, providing insight into nanometre-scale mechanics.

Biological applications of GLAD may be important, but, like magnetics, many issues must be addressed. The controlled porosity obtainable with GLAD, however, is similar to many biological materials, and to biological implant coatings. GLAD may provide new ability to create porous biological coatings for implants and other uses. Further study is definitely warranted in this area.

Electrical properties of GLAD films were not investigated in this thesis, but may be useful. High surface area films may make good capacitors, for example. Helical conductor films should behave as magnetic coils (inductors), but the usefulness of this effect is unknown.

GLAD also provides some interesting, and novel, insights into the mechanics of thin film growth. The extreme shadowing allows more direct observation of the fractal nature of zone 1 film growth than was possible previously. I suggest that scanning force microscope studies of evolving structure may help to clarify scaling effects. Control of magnetic and crystallographic orientation is an interesting, but poorly understood phenomenon, and also worthy of further study.

9. References

[1.] L. Abelmann and C. Lodder, Thin Solid Films **305** (1997), 1-21.

[2.] L. Abelmann, University of Twente (1994) ISBN 90-9007098-2, from [1] Abelmann 1997.

[3.] D. F. J. Arago, Mem. de l'Inst. **12** (1811), part 1, 93, from [9] Barron 1982.

[4.] A. Atkinson and P. T. Moseley, Appl. Surf. Sci. **65/66** (1993), 212-219.

[5.] R. M. A. Azzam, Appl. Phys. Lett. **61** (26) (1992), 3118-3120.

[6.] P. Ball, Designing the Molecular World, (Princeton University Press 1994).

[7.] P. Ball, Made To Measure, (Princeton University Press 1997).

[8.] A. -L. Barabasi and H. E. Stanley, Fractal Concepts in Surface Growth, (Cambridge University Press 1995).

[9.] L. D. Barron, Molecular Light Scattering and Optical Activity, (Cambridge Univ. Press, cambridge, UK, 1982).

[10.] L. D. Barron, Proceedings of Bianisotropics 1997, 27-30, Glasgow, June (1997).

[11.] V. A. Belyakov and V. E. Dmitrienko, Soviet Scientific Reviews / Section A **13** (1) (1989).

[12.] Born, M., and Wolf, E., Principles of Optics, (Pergamon, New York, 1980), Sec. 1.6.2.

[13.] L. Bouteiller and P. Le Barny, Liquid Crystals **21** (2) (1996), 157-174.

[14.] M. J. Brett et al., J. Mat. Sci. **3** (1992), 64-70.

[15.] D. J. Broer et al., Nature **378** (1995), 467-469.

[16.] D. A. G. Buggeman, Ann. Phys. (Leipzig) **24** (1935), 636, from [111] Smith 1989.

[17.] S. Chandrasekhar, Liquid Crystals, (Cambridge University Press 1977).

[18.] J. Chen et al., Appl. Phys. Lett. **67** (14) (1995), 1990-1992.

[19.] J. Chen et al., Appl. Phys. Lett. **68** (7) (1996), 885-887.

[20.] J. Chen et al., J. Appl. Phys. **80** (4) (1996), 1985-1990.

[21.] J. Cheng et al., Appl Phys. Lett. **37** (8) (1980), 716-719.

[22.] S. Y. Chou, Proceedings of the IEEE **85** (4) (1997), 652-671.

[23.] D. Coates, J. Mater. Chem. **5** (12) (1995), 2063-2072.

[24.] M.S. Cohen, J. Appl. Phys. **32** (1961), 87S, from [60] van Kranenburg 1994.

[25.] P. J. Collings, Liquid Crystals, (Princeton University Press, Princeton, New Jersey, USA, 1990).

[26.] R. W. Collins, Rev. Sci. Instrum. **61** (1990), 2029, from [105] Rovira 1998.

[27.] H. de Vries, Acta. Crystallogr. **4** (1951), 219-226.

[28.] A. G. Dirks, and H. J. Leamy, Thin Solid Films **47** (1977), 219-233.

[29.] K. -H. Ernst et al., Proceedings of Bianisotropics 1997, 77-80, Glasgow, June (1997).

[30.] A. Fresnel, Bull. Soc. Philomath (1824), 147, from [9] Barron 1982.

[31.] A. Fresnel, Ann. Chim. **28** (1825), 147, from [9] Barron 1982.

[32.] L. J. Friedrich et al., Thin Solid Films **226** (83) (1995).

[33.] L. J. Friedrich, Ph. D. dissertation thesis, University of Alberta (1997).

[34.] J. M. Garcia-Ruiz et al. Speculations in Sci and. Technol. **15** (1) (1992), 60-71.

[35.] J. C. M. Garnett, Phils. Trans. R. Soc. Lond. **203** (1904), 385, from [111] Smith 1989.

[36.] P. G. de Gennes and J. Prost, The Physics of Liquid Crystals, (Clarendon, Oxford, UK, 1993).
[37.] A. P. Giri and R. Messier, Mat. Res. Soc. Symp. Proc. **24** (1984), 221-227.
[38.] W. J. Gunning et al., Appl. Opt. **28** (14) (1989), 2945-2948.
[39.] V. K. Gupta and N. L. Abbott, Science **276** (1997), 1533-1536.
[40.] K. Hara, J. Sci. Hiroshima Univ., A-II 34 (1970), 139-163, from [1] Abelmann 1997.
[41.] K. Hara et al., Jpn. J. Appl. Phys. **33** (1994), 3448-3452.
[42.] I. J. Hodgkinson et al., Appl. Opt. **35** (28) (1996), 5563-5568.
[43.] I. J. Hodgkinson, P. I. Bowmar, and Q. H. Wu, Appl. Opt. **34** (1) (1995), 163-168.
[44.] I. J. Hodgkinson et al., J. Opt. Soc. Am. A. **2** (10) (1985), 1693-1697.
[45.] I. J. Hodgkinson and P. W. Wilson, CRC Crit. Rev. Solid State Mat. Sci. **15** (1) (1988), 27-61.
[46.] L. Holland, J. Opt. Sci. Am. **43** (1953), 376, from [60] van Kranenburg 1994.
[47.] C. A. Huber et al., Science **263** (1994), 800-802.
[48.] T. E. Huber and L. Luo, Appl. Phys. Lett. **70** (19) (1997), 2502-2504.
[49.] T. E. Huber et al., Submitted to Physical Review B, March 1998.
[50.] T. E. Huber and L. Luo, Appl. Phys. lett. **70** (19) (1997), 2502-2504.
[51.] T. Ishiji and K. Takahashi, Sensors and Actuators B **13/14** (1993), 583-384.
[52.] S. D. Jacobs, J. Fus. Energy **5** (1) (1986), from [109] Shankar 1997.
[53.] D. L. Jaggard, Appl. Phys. **18** (1979), 211-216.
[54.] T. Jaworek et al., Science **279** (1998), 57-60.
[55.] M. Kamiya et al., J. Phys. Soc. Jpn. **52** (10) (1983), 3585-3591, from [1] Abelmann 1997.
[56.] B. Kasapbasioglu et al., Sensors and Actuators B **13/14** (1993), 749-751.
[57.] K. Kato et al., Jpn. J. Appl. Phys. **33** (1994), 4946-4949.
[58.] H. Kelker and R. Hatz, Handbook of Liquid Crystals, (Verlag Chemie, Weinheim 1980).
[59.] H. van Kranenburg et al., IEEE Trans. Mag. **26** (5) (1990), 1620-1622.
[60.] H. van Kranenburg and C. Lodder, Mat. Sci. Eng. **R11** (7) (1994), 295-354.
[61.] T. G. Knorr and R. W. Hoffmann, Physical Review **113** (1959), 1039-1046, from [1] Abelmann 1997.
[62.] J. Krug, Mat.-wiss u. Werkstofftech. **26** (1995), 22-26.
[63.] K. Kuwahara and J. Hirota, Jpn. J. Appl Phys. **13** (1974), 1093, from [60] van Kranenburg 1994.
[64.] K. Kuwahara and S. Shinzato, Thin Solid Films **164** (1988), 165-168.
[65.] A. Lakhtakia and W. S. Weiglhofer, Proc. R. Soc. Lond. A **448** (1995), 419-437.
[66.] A. Lakhtakia and W. S. Weiglhofer, Microwave Opt. Tech. Lett. **6** (1993), 804-806.
[67.] A. Lakhtakia and W. S. Weiglhofer, Microwave and Optical Technol. Lett. **11**(6) (1996), 320-323.
[68.] A. Lakhtakia and W. S. Weiglhofer, Proc. R. Soc. Lond. A **453** (1997), 93-105.
[69.] A. Lakhtakia (ed), Selected Papers on Linear Optical composite Materials, (SPIE Optical Engineering Press, Bellingham, Wa, USA, 1996).
[70.] A. Lakhtakia et al., Innov. Mat. Res. **1** (2) (1996), 165-176.
[71.] A. Lakhtakia, Optik **105** (3) (1997), 115-120.

[72.] A. Lakhtakia, Optik **106** (2) (1997), 45-52.
[73.] L. T. Lamont Jr., Solid State Technol. **22** (9) (1979), 107-112.
[74.] L. D.Landau and E. M. Lifshitz, Electrodynamics of Continuous Media, 2nd ed. (Pergamon, New York, 1966).
[75.] L. I. Maissel and R. Glang, Handbook of Thin Film Technology, (McGraw-Hill Book Company 1970,1983).
[76.] S. Manning-Meier and D. K. Gupta, Trans. of the American Society of Mechanical Engineers - Proceedings of the International Gas Turbine and Aeroengine Congress and Exposition, Cologne, Germany, June 1-4, 1992, 1-9.
[77.] G. W. Mbise et al., J. Phys. D: Appl. Phys. **30** (1997), 2103-2122.
[78.] A. J. McPhun et al., Electr. Lett. **34** (4) (1998), 360-361.
[79.] R. Messier et al., J. Vac. Sci. Technol. A **2** (2) (1984), 500-503.
[80.] R. Messier et al., J. Vac. Sci. Technol. A **15** (4) (1997), 2148-2152.
[81.] R. Messier, J. Vac. Sci. Technol. A **4** (3) (1986), 490-495.
[82.] R. Meyer, Phys. Rev. Lett. **22** (18) (1969), 918-921.
[83.] S. Mori et al., J. Opt. Soc. Am. A **7** (8) (1990), 1562-1566.
[84.] T. Motohiro and Y. Taga, Appl. Opt. **28** (13) (1989), 2466-2482.
[85.] T. Motohiro and Y. Taga, Appl. Opt. **28** (1989), 2466-2488.
[86.] B. A. Movchan and A. V. Demchishin, Phys. Met. Metallogr. **28** (83) (1969).
[87.] D. R. Nagy, Liburdi Engineering, personal communication, 1995.
[88.] J. M. Nieuwenhuizen and H. B. Haanstra, Philips Tech. Rev. **27** (1966), 87-91.
[89.] H. Ong and R. Meyer, J. Opt. Soc. Am. **73** (2) (1983), 167-176.
[90.] M. Ohring, The Materials Science of Thin Films, (Academic Press, New York, 1992.
[91.] L. Pasteur, Ann. Chim. **24** (1848), 457, from [9] Barron 1982.
[92.] E. W. Pugh et al., IBM J. **4** (1960), 163, from [60] van Kranenburg 1994.
[93.] R. Roark, Roark's Formulas for Stress and Strain, (McGraw-Hill, New York, 1989).
[94.] K. Robbie and M. J. Brett, J. Vac. Sci. Technol. A **15** (3) (1997), 1460-1465.
[95.] K. Robbie et al., J. Vac. Sci. Technol. A **13** (3) (1995), 1032-1035.
[96.] K. Robbie et al., J. Vac. Sci. Technol. B, **16** (3) (1998), 1115-1122.
[97.] K. Robbie et al., J. Vac. Sci. Technol. A **13** (6) (1995), 2991-2993.
[98.] K. Robbie et al., Submitted to J. of Mat. Res., March 1998.
[99.] K. Robbie and M. J. Brett, Proceedings of Bianisotropics 1997, Glasgow, June (1997).
[100.] K. Robbie et al., Nature **384** (1996), 616.
[101.] K. Robbie et al., Electron. Lett. **33** (14) (1997), 1213-1214.
[102.] K. Robbie, D. J. Broer, and M. J. Brett, In preparation.
[103.] K. Robbie, A. Huzinga, M. Seto, and M. J. Brett, In preparation.
[104.] P. I. Rovira et al., Appl. Phys. Lett. **71** (9) (1997), 1180-1182.
[105.] P. I. Rovira et al., Thin Solid Films **313-314** (1998), 373-378.
[106.] H. Sankur et al., Appl. Opt. **27** (8) (1988), 1564-1567.
[107.] G. M. Schwab et al., Kolloid-Zeitschrift **68** (1934), 157, from [29] Ernst 1997.
[108.] A. Seeboth, Thin Solid Films **223** (1993), 140-142.
[109.] N. K. Shankar, Ph.D. Dissertation, Cornell University, 1990.

[110.] J. C. Sit et al., Submitted to J. Vac. Sci. Technol. A, July 1998.
[111.] G. B. Smith, Opt. Comm. **71** (5) (1989), 279-284.
[112.] D. O. Smith, J. Appl. Phys. **30** (4) (1959), 264S-265S, from [1] Abelmann 1997.
[113.] D. O. Smith et al., J. Appl. Phys. **31** (10) (1960), 1755-1762, from [1] Abelmann 1997.
[114.] Southwell, W. H., J. Opt. Soc. Am. A **5** (1988), 1558-1564.
[115.] M. Suzuki and Y. Taga, J. Appl Phys. **71** (6) (1992), 2848-2854, from [1] Abelmann 1997.
[116.] Y. Taga and T. Motohiro, J. Crys. Growth **99** (1990), 638-642.
[117.] R. N. Tait et al., Thin Solid Films **226** (1993), 196-201.
[118.] R. N. Tait et al., J. Vac. Sci. Technol. A **10** (4) (1992), 1518-1521.
[119.] R. N. Tait et al., J. Appl. Phys. **70** (8) (1991), 4295- 4300.
[120.] C. Tang and S. Liang, Phys. Rev. Lett. **71** (7) (1993), 2769-2770.
[121.] J. A. Thornton, Ann. Rev. Mater. Sci **7** (1977), 239-260.
[122.] J. A. Thornton, J. Vac. Sci. Technol. A **4** (6) (1986), 3059-3065.
[123.] J. D. Traylor-Kruschwitz and W. T. Pawlewicz, Appl. Opt. **36** (10) (1997), 2157-2159.
[124.] V. C. Venugopal and A. Lakhtakia, Proceedings of Bianisotropics 1997, Glasgow, June (1997).
[125.] D. Vick et al., Accepted by Thin Solid Films, June 1998.
[126.] H. Vithana et al., Jpn. J. Appl. Phys. **35** (2-3A) (1996), L320-L323.
[127.] M. Volmer, Kristallbildung durch gerichtete Dampfmolekule, Z. Phys. **5** (1921) 31-34, from [1] Abelmann 1997.
[128.] L. Ward, The Optical constants of Bulk Materials and Films, (Adam Hilger, Bristol, UK, 1988).
[129.] K. L. Westra and D. J. Thomson, Thin Solid Films **257** (1995), 15-21.
[130.] E. White and E. Shors, Dental Clinics of North America **30** (1) (1986), 49-67.
[131.] H. S. Witham et al., J. Vac. Sci. Technol. A **11** (4) (1993), 1881-1887.
[132.] N. O. Young and J. Kowal, Nature **183** (1959), 104-105.
[133.] U.S. Patent #3,679,290, Notch Filters-Opposite Rotary Sense, 1972, from [109] Shankar 1997.
[134.] U.S. Patent #3,711,181, Notch Filters-Same Intrinsic Rotary Sense, 1973, from [109] Shankar 1997.
[135.] U.S. Patent #4,321,311, Columnar Grain Ceramic Thermal Barrier Coatings, 1982.